BRNO UNIVERSITY OF TECHNOLOGY
VYSOKÉ UČENÍ TECHNICKÉ V BRNĚ

FACULTY OF MECHANICAL ENGINEERING
FAKULTA STROJNÍHO INŽENÝRSTVÍ

ENERGY INSTITUTE
ENERGETICKÝ ÚSTAV

CAVITATING JET
KAVITUJÍCÍ PAPRSEK

MASTER'S THESIS
DIPLOMOVÁ PRÁCE

AUTHOR Bc. Helena Kotoulová
AUTOR PRÁCE

SUPERVISOR doc. Ing. Pavel Rudolf, Ph.D.
VEDOUCÍ PRÁCE

BRNO 2022

VYSOKÉ UČENÍ TECHNICKÉ V BRNĚ
FAKULTA STROJNÍHO INŽENÝRSTVÍ

Zadání diplomové práce

Ústav:	Energetický ústav
Studentka:	**Bc. Helena Kotoulová**
Studijní program:	Strojní inženýrství
Studijní obor:	Fluidní inženýrství
Vedoucí práce:	**doc. Ing. Pavel Rudolf, Ph.D.**
Akademický rok:	2020/21

Ředitel ústavu Vám v souladu se zákonem č.111/1998 o vysokých školách a se Studijním a zkušebním řádem VUT v Brně určuje následující téma diplomové práce:

Kavitující paprsek

Stručná charakteristika problematiky úkolu:

Kavitační paprsek vzniká, pokud voda o vysoké rychlosti opustí trysku a vnikne do okolí vyplněného opět vodou. Kolabující kavitační mrak dopadající na testovaný vzorek způsobuje kavitační erozi. Na základě tohoto principu funguje metoda pro zrychlené testy kavitačního opotřebení ASTMG134–17. Daný jev lze zkoumat jak experimentálně, tak s využitím výpočtového modelování proudění.

Cíle diplomové práce:

Cílem diplomové práce je výpočtové modelování kavitujícího paprsku, zjištění proudového pole, impaktních tlaků na testovaný vzorek a srovnání s experimentální vizualizací. Diplomová práce bude sloužit jako součást širšího výzkumného úkolu zabývajícího se popisem kavitačního opotřebení.

Seznam doporučené literatury:

SOYAMA, Hitoshi. Cavitating jet: a review. Applied Sciences. Basel: MDPI, 2020, 10(20), 1-27.

YANG, Yongfei, Wei LI, Weidong SHI, Wenquan ZHANG a Mahmoud A. EL-EMAM. Numerical Investigation of a High-Pressure Submerged Jet Using a Cavitation Model Considering Effects of Shear Stress. Processes. Basel: MDPI, 2019, (7), 1-18.

Termín odevzdání diplomové práce je stanoven časovým plánem akademického roku 2020/21

V Brně, dne

L. S.

doc. Ing. Jiří Pospíšil, Ph.D. ředitel ústavu	doc. Ing. Jaroslav Katolický, Ph.D. děkan fakulty

ABSTRACT

This diploma's thesis deals with the cavitating liquid jet and cavitation erosion models. It is divided into three main parts.

The theoretical part describes the fundamental principles of cavitation and its negative effects on the surface of circumflowed solid materials (e.g. at hydraulic machines). An extensive chapter is also devoted to a description of the cavitating liquid jet itself, including the mechanisms of its inception, growth and collapse. Another subchapter focuses on cavitation erosion models, which are of great importance for a prediction of the cavitation erosion in the phase of computational simulation.

In the experimental part, a copper sample was exposed to the cavitating jet in a test rig inspired by ASTM G134 standard and consequently, graphs of cumulative mass loss and mass loss rate were created. In addition, a visualization using high-speed camera was performed for better understanding of the cavitating liquid jet dynamic behavior.

The last part focuses on numerical simulations using Computational Fluid Dynamics (CFD) and the cavitation erosion prediction. Multiple computations were performed on different types of mesh with different turbulence models in order to optimize the numerical simulation. Subsequently, the results from the simulations were evaluated and used together with the results from the experiment to predict cavitation erosion.

Key words

Cavitation, cavitating liquid jet, cavitation erosion model, ASTM G134, numerical simulation, CFD

ABSTRAKT

Předložená diplomová práce se zabývá kavitujícím paprskem a je rozdělena do tří hlavních částí.

Teoretická část popisuje základní principy kavitace a její negativní účinky na povrch obtékaných těles (např. hydraulických strojů). Rozsáhlá kapitola je také věnována popisu samotného kavitujícího paprsku včetně mechanismů jeho vzniku, růstu a kolapsu. Další podkapitola je zaměřena na modely kavitační eroze, které mají velký význam pro predikci kavitační eroze ve fázi výpočtové simulace.

V experimentální části je popsáno testování vzorku mědi inspirované normou ASTM G134 a následné vytvoření grafů kumulativního hmotnostního úbytku a rychlosti úbytku hmotnosti. Dále byla také provedena vizualizace pomocí vysokorychlostní kamery, aby bylo možné podrobně prozkoumat dynamické chování kavitujícího paprsku.

Poslední část je zaměřena na numerické simulace pomocí výpočtového modelování proudění, tzv. Computational Fluid Dynamics (CFD), a na predikci kavitační eroze. Z důvodu optimalizace úlohy bylo provedeno více výpočtů na různých typech sítí s různými modely turbulence. Následně byly výsledky ze simulací vyhodnoceny a společně s výsledky z experimentu byly použity pro predikci kavitační eroze.

Klíčová slova

Kavitace, kavitující paprsek, kavitační erozní model, ASTM G134, numerická simulace, CFD

ROZŠÍŘENÝ ABSTRAKT

Diplomová práce se zabývá výzkumem kavitujícího paprsku, na jehož principu je založena jedna z hlavních metod používaných pro testování kavitace. V této metodě, podrobně popsané v normě ASTM G134, vzniká kavitace v turbulentní vrstvě generované rychle se pohybujícím proudem kapaliny. Nejčastější konfigurace zahrnuje trysku zanořenou pod hladinu rozsáhlé nádrže. Vzniklý kavitační oblak kolabuje na povrchu testovaného vzorku a následně dochází k erozi jeho povrchu. Předložená práce obsahuje teoretický popis kavitujícího paprsku, experimentální studii a také numerické simulace, sloužící k podrobnému prozkoumání tohoto velmi dynamického a nestabilního jevu.

Teoretická část začíná popisem základních principů kavitace, což je fyzikální jev, ke kterému dochází při náhlém poklesu tlaku pod tlak nasycených par. V ten moment se začnou vytvářet dutiny (tzv. kavity) naplněné plyny a parami okolní kapaliny. Tyto dutiny jsou následně unášeny proudem kapaliny do oblastí s vyšším tlakem, kde prudce kolabují a mohou značně poškodit povrch obtékaného tělesa. Mechanismy kavitační eroze zahrnují nejenom tlakové rázy, ale například i působení zvýšené teploty a elektrochemické procesy. Kavitace se může vyskytovat u různých hydraulických strojů, jako jsou turbíny a čerpadla, a může negativně ovlivnit jejich funkci, proto je velmi důležité vyvinout způsoby, jak se kavitaci vyhnout, nebo alespoň minimalizovat její účinky. Jedna sekce teoretické části je věnována také různým modelům kavitační eroze, které slouží k propojení experimentálních a numerických výsledků. Rozsáhlá kapitola je zaměřena přímo na kavitující paprsek a popisuje detailně jeho vznik a mechanismy zániku včetně vlivu vzdálenosti mezi ústím trysky a povrchem vzorku, dále také vlivu vstřikovacího tlaku, kavitačního čísla, geometrie trysky, rychlosti zvuku a vlastností vody.

V experimentální části byl testován vzorek mědi z hlediska kavitační eroze na novém experimentálním standu na OFIVK FSI VUT Brno. Nový stand je inspirovaný normou ASTM G134 a umožňuje pohodlnější manipulaci se vzorkem, a navíc zajišťuje přesnější měření. Mezi hlavní výstupy experimentální části patří grafy kumulativního hmotnostního úbytku a rychlosti úbytku hmotnosti, a navíc byla provedena vizualizace pomocí vysokorychlostní kamery, která umožnila stanovit frekvenci odtrhávání kavitujícího paprsku a poskytla nové informace o tvaru a nestabilním chování kavitujícího paprsku. Celkový hmotnostní úbytek po 15 hodinách testování byl pomocí vysoce přesné váhy stanoven jako 1.16461 g. Co je však důležitější, podařilo se dosáhnout všech stádií kavitační eroze v relativně krátkém čase, a proměřit tak celou tzv. S-křivku kumulativního úbytku hmotnosti. Bylo možné přesně rozeznat fázi inkubace, zrychlení eroze, její následné zpomalení a poté dosažení konstantní rychlosti úbytku hmotnosti. Mimo jiné experiment potvrdil optimální vzdálenost mezi vzorkem a ústím trysky (tzv. stand-off distance) stanovenou jako 50 mm, zaručující, že převažujícím mechanismem eroze je kavitace, a ne řezání vodním paprskem, neboť se na povrchu vzorku objevila charakteristická prstencovitá oblast s kavitačními důlky, tzv. pity. Naměřená data průtoku, tlaku a teploty také posloužila jako vstup při sestavování okrajových podmínek v numerických simulacích. Frekvence odtrhávání kavitačního oblaku určená pomocí snímků pořízených vysokorychlostní kamerou byla stanovena jako 1028 Hz, tedy perioda odtrhávání je $9.73 \cdot 10^{-4}$ s. Ve spolupráci s výzkumným centrem CEITEC se mimo jiné podařilo získat

soubor velmi zajímavých a poměrně unikátních snímků okavitovaného vzorku. Povrchová topografie, profilometrie a pozorování erodovaného povrchu a jednotlivých vyerodovaných částic pomocí SEM nám umožnily podrobněji studovat důsledky kavitační eroze. Navíc se podařilo stanovit tvrdost vzorku dle Brinella, která je spojená s kavitační odolností, na 86.74 HBW.

Další soubor experimentů byl proveden za účelem pozorování distribuce pitů na vzorku a pro určení vyerodovaného objemu během inkubační doby. Výsledný celkový výkon dopadající na povrch vzorku byl stanoven jako 0.403 W/m^2 a později byl tento výsledek propojen s výsledky z výpočtového modelování prostřednictvím modelu energetické kaskády.

Poslední kapitola se věnuje popisu provedených numerických simulací kavitujícího paprsku. Rozsáhlá část této kapitoly byla věnována také důkladnému popisu vybraných kavitačních a turbulentních modelů a celkovému nastavení jednotlivých výpočtů včetně problémů spojených s modelováním tak dynamického jevu, jakým je kavitující paprsek. Finální výpočet byl proveden s RNG k-ε turbulentním modelem rozšířeným o UDF pro snížení turbulentní viskozity. Následný post-processing dat zahrnoval vyhodnocení frekvence odtrhávání kavitačního paprsku pomocí rychlé Fourierovy transformace provedené z dat objemových zlomků s výsledkem 5256 Hz. Bohužel je tato hodnota přibližně 5x vyšší než hodnota frekvence odtrhávání určená pomocí experimentu. Jedním z možných vysvětlení je vyšší tlumící efekt během experimentu, který může souviset se zvýšeným obsahem vzduchu ve vodě.

Důležitá podkapitola výpočtové části je zaměřena na stanovení celkového výkonu dodávaného vzorku pomocí modifikovaného modelu energetické kaskády. Nejprve byla efektivní vzdálenost h_{agr}, při které se předpokládá, že kavitace ještě způsobí vážné poškození vzorku, určena jako 10% tloušťky kavitační struktury; a počáteční tlak plynu p_{g0} byl stanoven jako 1000 Pa. Výsledný celkový výkon byl však přibližně 15krát větší než ten, který byl určen z experimentu.

Z tohoto důvodu byla snaha upravit modifikovaný model energetické kaskády – zaprvé, hodnota h_{agr} byla snížena na 5% tloušťky kavitační struktury kvůli velmi vysoké kavitační intenzitě kavitujícího paprsku, a zadruhé, p_{g0} bylo zvýšeno na hodnotu 5000 Pa. Navýšení hodnoty počátečního tlaku plynu bylo provedeno za účelem implementování pravděpodobného vlivu vyššího obsahu vzduchu v experimentu, který měl patrně za následek nižší frekvenci odtrhávání než v případě CFD. Tyto úpravy vedly k tomu, že celkový výkon dodávaný vzorku se snížil na hodnotu 0.96 W/m^2, což už podstatně lépe odpovídá výše uvedenému experimentálnímu výsledku 0.403 W/m^2.

Je však velmi důležité poznamenat, že celé vyhodnocení modifikovaného modelu energetické kaskády je zatíženo chybami jednak z experimentu, tak i z výpočtu. V případě experimentu by bylo potřeba přesněji vyhodnotit objem pitů a také stanovit obsah vzduchu ve vodě. Co se týče výpočtu, tak model turbulence SST k-ω by mohl přinést podstatně přesnější data, nicméně simulace s tímto modelem turbulence vyžaduje velice jemnou síť a modelování kavitujícího paprsku je třeba provádět za použití nízkého časového kroku. Tyto vlivy dohromady vedou na velice náročnou výpočetní úlohu.

Závěrem lze říci, že model energetické kaskády je nepochybně velmi silným nástrojem pro predikci kavitační eroze ve fázi CFD modelování. Některé typy problémů jsou však pro tento přístup vhodnější, obzvláště případy s kavitačním číslem v rozmezí desetin až jednotek, což bohužel není případ kavitujícího paprsku. Přesto lze konstatovat, že tato práce přinesla mnoho cenných výsledků a poznatků týkajících se výpočtové a experimentální studie kavitujícího paprsku a napomohla tak vědeckému výzkumu v této oblasti.

BIBLIOGRAPHIC CITATION

KOTOULOVÁ, Helena. *Kavitující paprsek* [online]. Brno, 2022 [cit. 2022-05-08]. Dostupné z: https://www.vutbr.cz/studenti/zav-prace/detail/137042. Diplomová práce. Vysoké učení technické v Brně, Fakulta strojního inženýrství, Energetický ústav. Vedoucí práce Pavel Rudolf.

DECLARATION

I declare that I have personally compiled the thesis "**Cavitating jet**" according to the instruction of my supervisor, doc. Ing. Pavel Rudolf, Ph.D. and with the use of the sources listed in bibliography.

Datum

Helena Kotoulová

ACKNOWLEDGMENT

First of all, I would like to sincerely thank my diploma's thesis supervisor doc. Ing. Pavel Rudolf, Ph.D. for his patience and guidance. I would also like to thank Bronislav Kusý and Karel Večeřa for helping me to conduct the experiments; to Ing. David Štefan, Ph.D. for a valuable advice concerning the numerical simulations; to Ing. Hana Lisá, Ph.D. and Ing. Ladislav Šnajdárek, Ph.D. for help with the mass measurements of the tested sample; to Ing. Ondřej Cejpek for performing the cavitation visualization using high-speed camera; to Ing. Pavel Gejdoš, Ph.D., Ing. Martin Juliš, Ph.D. and Ing. Lenka Klakurková, Ph.D. from CEITEC for surface topography and profilometry of samples and of course, big thanks belong to my family and my boyfriend, Marek Polčák, for the support during my whole study.

Contents

Introduction

The thesis is focused on an investigation of a cavitating liquid jet, one of the main methods used for cavitation testing. The presented research of the cavitating jet contains a theoretical description, an experimental study, and multiple numerical simulations to explore this complex problem in detail.

The theoretical part starts with the description of fundamental principles of cavitation - a physical phenomenon, which occurs in case of a sudden pressure drop below saturated vapor pressure. In that moment, cavities filled with gases and vapors of surrounding liquid emerge, and as they are carried away to the locations of higher pressure, they collapse abruptly, causing a large damage to the nearby solid body. The described processes are entitled cavitation inception, growth and collapse, so-called cavitation erosion mechanisms. Cavitation can occur at various hydraulic machinery, such as turbines and pumps, and can negatively affect their function. Therefore, it is very important to investigate cavitation in order to discover ways of avoiding it, or at least, minimizing its effects. One part of the theoretical section is also devoted to the cavitation erosion models, which are used for linking experimental and numerical results. An extensive chapter focuses directly on the cavitating liquid jet in terms of its development and collapse mechanisms and its influencing parameters, such as standoff distance, injection pressure, cavitation number, nozzle geometry, speed of sound and water qualities.

In the experimental part, a copper sample was tested in terms of cavitation erosion via cavitating liquid jet. A new experimental stand, inspired by ASTM G134 standard, was designed and built at OFIVK FME BUT Brno. The new stand enables a more comfortable way of manipulating with the sample and moreover, it ensures more accurate measurement. The main outcomes of the experiment include graphs of cumulative mass loss and mass loss rate, and in addition, information about the shape of the cavitating jet and its shedding frequency was gathered by a visualization using high-speed camera. Moreover, in a cooperation with scientists from CEITEC, a detailed display of the eroded sample and individual eroded particles was obtained. Surface topography, profilometry and observation by Scanning Electron Microscope (SEM) were performed, hence, enabling us to better understand the cavitation erosion mechanisms.

The last chapter is devoted to numerical simulation of cavitating jet using Computational Fluid Dynamics (CFD) and to cavitation erosion prediction. Multiple computations with thoroughly described settings were performed on account of optimization of the simulation, thus the numerical results together with the experimental results could be used for cavitation erosion prediction based on the modified energy cascade model.

1 Cavitation

Cavitation is a process of generation cavities in liquid; this can be achieved by various processes and technologies – laser cavitation (created by laser), acoustic cavitation (caused by ultrasonic waves), particle cavitation (induced by a beam of elementary particles, e.g. protons) and hydrodynamic cavitation. The following subchapter will be devoted to the description of hydrodynamic cavitation [1].

1.1 Principle and types of hydrodynamic cavitation

In principle, hydrodynamic cavitation is a phase change from liquid to vapor (evaporation), which occurs when liquid is subjected to a significant pressure drop – below saturated vapor pressure. In that moment, cavities (also called cavitation bubbles) filled with vapor of surrounding liquid start to emerge and they grow subsequently, while they are being carried away by the flow. Once they get to a region with higher pressure, they implode aggressively, causing severe material erosion of a near solid body. Therefore, cavitation, as a physical phenomenon, needs a lot of investigation as it can strongly affect the function of propellers, turbines, pumps and other hydraulic machines. However, it is important to mention, that the processes accompanying the cavitation collapse (increased pressure and temperature, shock waves), can be advantageously used for destroying unwanted microbiological organisms in water [1], [2], [3], [4].

There are also various types of hydrodynamic cavitation, distinguishable according to its shape, location and motion. Cavitation can be either transposing (cavitation moves in a fluid flow), non-transposing (connected to a solid body) or it can reach a state called supercavitation, occurring when cavitation is entirely hemmed about the solid body. Another important type of cavitation is vortex cavitation, which emerges in a vortex core as it is a location of significantly lower pressure than of surrounding liquid. Hydrofoils are usually susceptible to a formation of so-called sheet cavitation, see Figure 1 [5]. Last type of hydrodynamic cavitation worth mentioning is a cavitation cloud, which is a cluster of individual cavitation bubbles. Dynamics of cavitation clouds is different from single cavitation bubble dynamics, and it is usually more complicated [1].

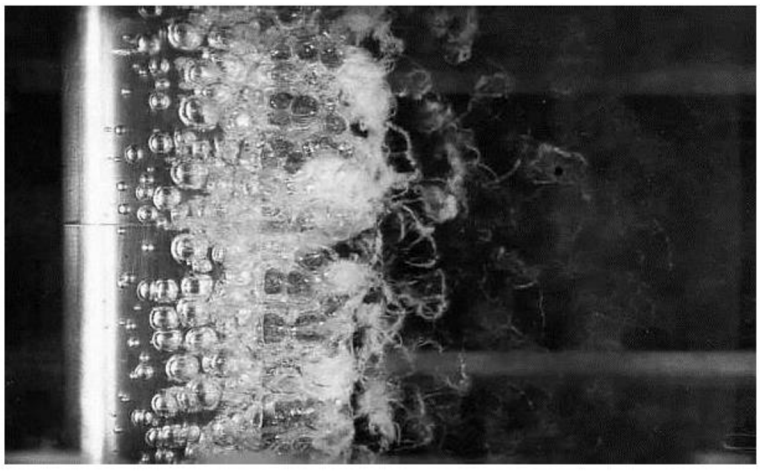

Figure 1: Formation of cavitation [5]

1.2 Stages of cavitation

Cavitation process can be divided into three main stages – inception, growth and collapse, see Figure 2. These stages will be described in following subchapters in detail.

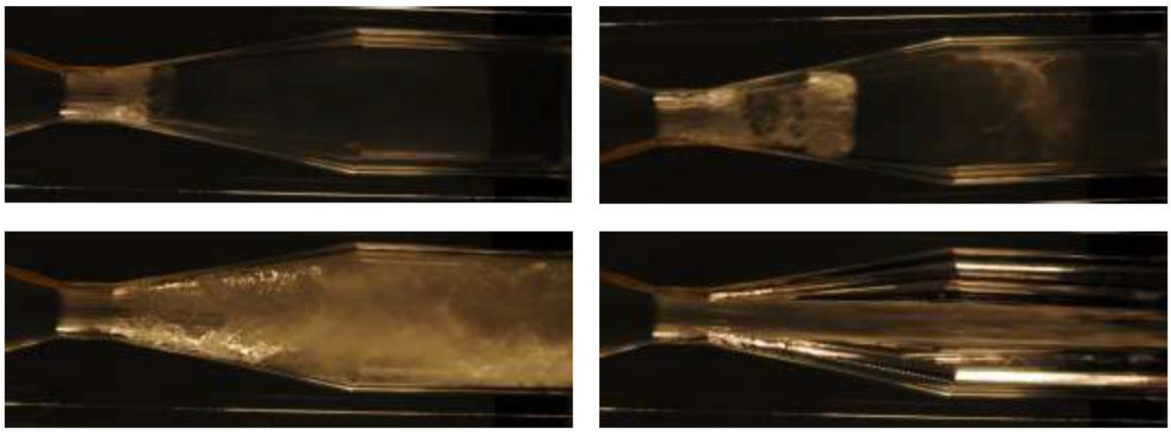

Figure 2: Stages of cavitation in Venturi tube - inception (upper left), growth (upper right and bottom left), supercavitation (bottom right) [6]

1.2.1 Inception of cavitation

As mentioned above, cavitation occurs during a pressure drop below saturated vapor pressure. Liquids are usually not perfectly clean and contain various mechanical particles and molecules of undissolved gas, which act as cavitation nuclei. Cavitation also usually occurs in so–called weak locations, which are points of lower liquid strength and are caused e.g. by vortices in a turbulent boundary layer. During the mentioned pressure drop, cohesion of liquid is affected leading to a generation of cavities filled with vapors of surrounding liquid and also gases. In case of even further drop in pressure, cavitation bubbles grow accordingly and they are simultaneously transported by surrounding liquid. Typical locations with low pressure are e.g. narrow part of Venturi tube or pump suction [1], [2].

Although cavitation is not directly caused by temperature change, but by pressure drop; the saturated vapor pressure is temperature dependent - as temperature increases, so does the saturated vapor pressure. There are many equations describing this dependency, e.g. modified Clausius-Clapeyron equation [7]:

$$p_v = 100 \cdot e^{53.6796 - \frac{6743.69}{T} - 4.8451 \cdot \ln(T)} \tag{1}$$

Another influential parameter of cavitation growth is an initial radius of a cavitation bubble. Critical value of radius can be distinguished and accordingly, two cases can follow. Either the initial radius is lower than critical radius, meaning that pressure of surrounding liquid is higher than inner pressure of the bubble resulting in a reduction of the bubble size, or the initial bubble radius is bigger than the critical one, leading to a growth of the bubble because of higher inner bubble pressure in comparison to the surrounding pressure. Therefore, in case of larger cores, it is easier to achieve cavitation as such low pressure drops are not needed [1], [8]. These conclusions are also depicted in Figure 3.

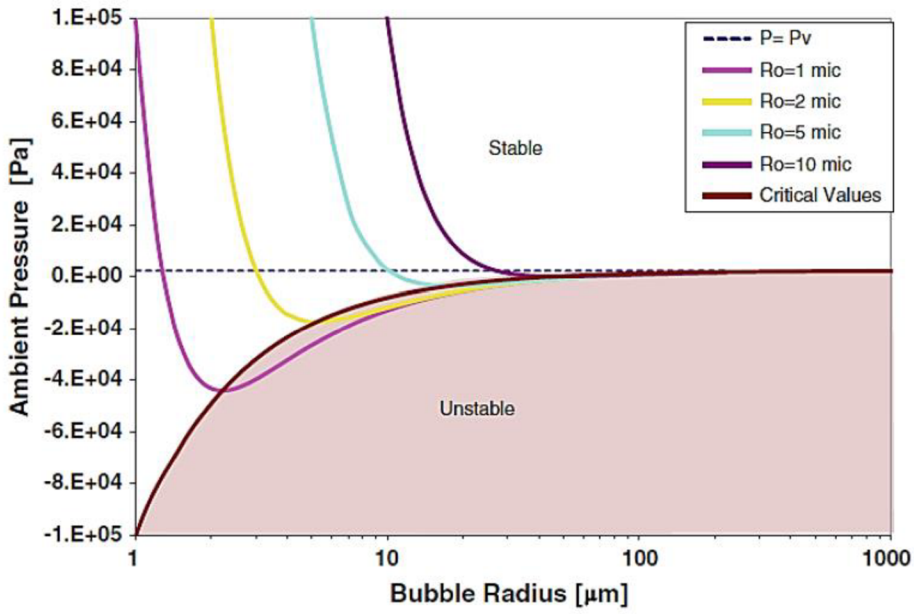

Figure 3: Influence of initial radius of cavitation bubble on its growth [2]

As mentioned above, cavitation occurs when fluid continuum is disrupted and cohesive forces are overcome by low pressure field. Cohesion forces are strongly linked to surface tension, therefore, it is obvious that this physical property has a big influence on cavitation inception. Higher surface tension supports cohesion forces, hence, it is more difficult to reach cavitation [1].

Viscosity has similar effects – with higher viscosity (therefore higher internal friction forces), the cavitation growth and collapse are slower [1], [8].

Liquid compressibility reduces the speed of sound in comparison to incompressible fluid, therefore, shock waves emerging during cavitation collapse does not move so fast [8].

A strong tool for description of cavitation bubble dynamics is Rayleigh-Plesset equation, which is derived directly from Navier-Stokes equation. In general, this equation is as follows [5]:

$$\frac{p_B(t)-p_\infty(t)}{\rho}=R\ddot{R}+\frac{3}{2}(\dot{R})^2+\frac{4\nu_L}{R}\dot{R}+\frac{2\sigma_L^*}{\rho R}, \tag{2}$$

where:

$R(t)$ is a bubble radius variable in time,

ρ, ν_L, is surrounding liquid density and kinematic viscosity respectively,

σ^*_L is the surface tension at interface of bubble and surrounding liquid,

$p_B(t)$ is homogenous pressure in the bubble,

$p_\infty(t)$ is external pressure at an infinite distance from the bubble.

Neglecting the non-linear term with second derivative and the terms with viscosity and surface tension, lead to a simplified version of Rayleigh-Plesset equation, which is used as a basic numerical model for cavitation modelling in CFD (computational fluid dynamics) [6].

An important coefficient (a non-dimensional number), which describes the intensity of cavitation, is a cavitation number. The lower the cavitation number, the more intensive and aggressive the cavitation is. There are several definitions of cavitation number, the mostly used one is the following :[2]

$$\sigma = \frac{p_\infty - p_v}{\frac{1}{2}\rho v_\infty^2}, \tag{3}$$

where:

p_∞, v_∞ are the reference pressure and the reference velocity respectively,

p_v is the saturated vapor pressure,

ρ is the liquid density.

1.2.2 Cavitation collapse

Cavitation collapse is a condensation process followed by compression of vapor and subsequent emission of shock waves. It is a phenomenon reversed to explosion (hence, implosion) and it begins at the moment of reaching a location with higher pressure. Cavities collapse abruptly and result in an intense local increase of pressure and temperature. There are various mechanisms of cavitation collapse, which can occur simultaneously – micro jet, hot spots, electrochemical processes, divergent spherical waves, cavitation cloud collapse.

Collapse of a single cavitation bubble is by no means a continuous process - on the contrary, a few rebounds of the bubble size can be observed. This is caused by the volume of vapors trapped inside the bubble, which eventually cannot be compressed more. These rebounds make the cavitation collapse very complicated to computationally model. After shrinking and rebounding, the residual bubble remains in the liquid [8], [9], see also Figure 6a. The collapse of a cavitation bubble with its rebound is depicted in Figure 4.

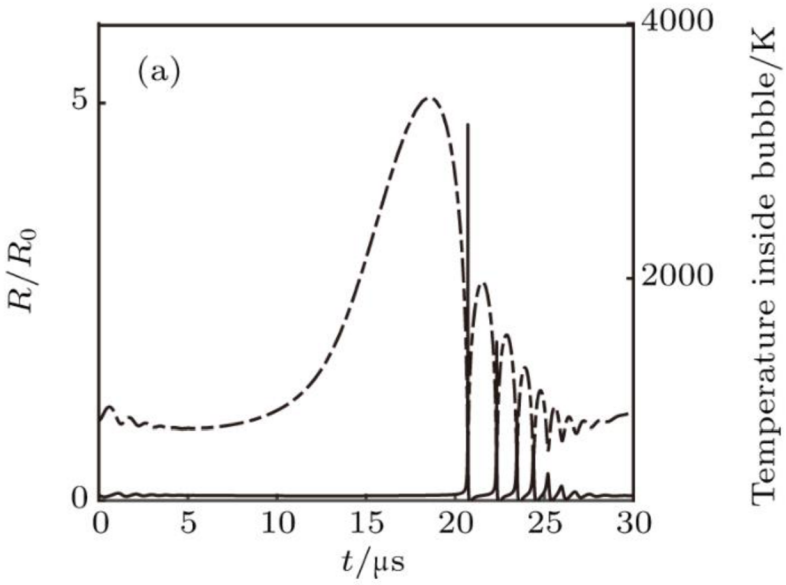

Figure 4: Cavitation bubble collapse and its rebounds [9]

Micro jet is a typical form of collapsing cavity. As the bubble gets in a location with higher pressure, it starts to cave inwards producing an unmistakable ring shape, see Figure 5. Consequently, a high speed liquid jet flows throughout the ring. The liquid jet always moves towards the surrounding solid body as the bubble collapses faster at the side more remote from the solid body. The micro jet can reach velocities up to speed of sound of liquid, thus meaning a very high potential of material damage [8].

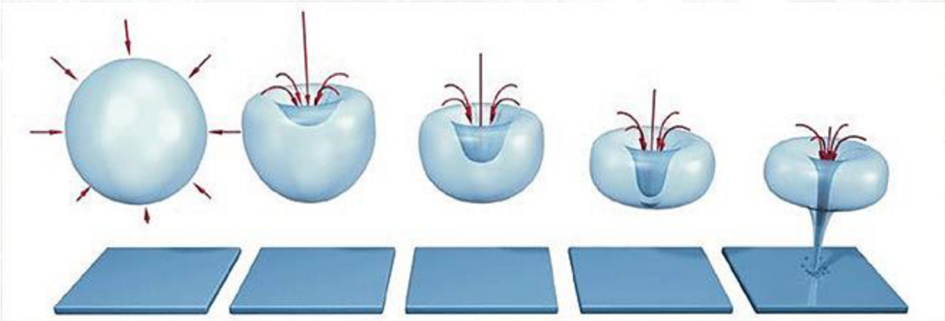

Figure 5: Micro jet [9]

Hot spots are an interesting phenomenon occurring during cavitation collapse. The process of cavity collapse is very fast and can be therefore considered as adiabatic one. The adiabatic compression of gases trapped in the cavity leads to significant increase of pressure and temperature, creating so-called hot spots. The temperature increase also results in decomposition of water into hydrogen and hydroxide and if a consequent oxidation-reduction reaction takes place, hydrogen peroxide is created, which can be advantageous in a destruction of microorganisms present in the liquid [11].

Vortex cavitation, schematically shown in Figure 6b, is even more severe than spherical bubble cavitation. The vortex cavitation can occur e.g. below Francis turbine operating in non-optimal regimes leading to the generation of vortex rope, which can include cavitation in its center; or behind ship's screw-propellers. Micro jet can also occur in the center of vortex cavitation [1], [12].

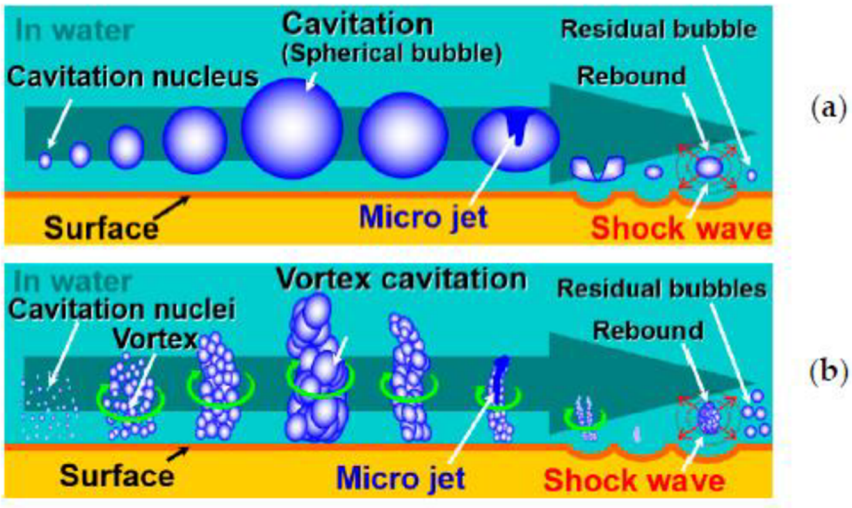

Figure 6: Cavitation inception, growth and collapse in case of spherical bubble (a) and vortex cavitation (b) [13]

As a result of cavitation collapse, various electrochemical processes take place leading to electrochemical corrosion of the material [8].

Shock waves generated as a result of either single cavitation bubble collapse, or even the whole cavitation cloud collapse, are probably main reason for consequent material erosion. Though, the cavitation collapse is a very short process, it is repeated with high frequency and the pressure waves can reach values up to 150 MPa, which is not a negligible number. Hence, the impact pressure amplitude caused by shock waves can quite easily exceed material threshold characteristics (either the yield stress or even the ultimate strength) [8], [12].

Table 1 shows a comparison of four cavitation erosion mechanisms in terms of the pressure amplitude and time duration. It can be seen that collective micro bubble collapse generates the highest pressure amplitude and simultaneously, the duration of this phenomenon is quite long. As mentioned above, cavitating vortices are also very aggressive form of cavitation collapse.

Table 1: Comparison of various cavitation erosion mechanisms [12]

Mechanism	Type of loading	Pressure amplitude [MPa]	Duration [μs]
Micro bubble collapse	Pressure wave	100	1
Micro jet (from a single 1 mm bubble)	Impacting jet	150	0.03
Collective micro bubble collapse	Pressure wave	>>100	>>1
Cavitating vortices	Impacting jet	>100	>10

1.3 Cavitating liquid jet [13]

Cavitating liquid jet is a phenomenon which is advantageously used in the ASTM G134 testing method. The cavitation occurs in the turbulent layer generated by the fast-moving liquid jet, which can be either structured (in case of a precise shape of a nozzle), or unstructured with a rather random distribution of cavitation bubbles. In contrast to other cavitation testing methods (e.g. generation of cavitation bubbles by vibratory apparatus – ASTM G32), in this method, the cavitation intensity can be altered significantly by means of the jet velocity or its diameter and angle. As a consequence, a more realistic distribution of bubble diameters and collapse frequencies could be obtained, even with the cavitation number much smaller than 1 (and jet pressure can reach values up to 300 MPa).

Soyama [13] presented a thorough study on cavitating liquid jet and some of the conclusions are going to be described in this thesis in the following sections and subsections.

Cavitating liquid jet is strongly connected to an emergence of many various instabilities, such as vortices in turbulent jets, ring vortices, single helical vortices and even double-helical vortices. Cavitation clouds shed periodically with rather high frequencies of order of hundreds Hz, causing severe damage to the material. Clouds shedding would not be visible at normal light, therefore flash lights with low exposure times are usually used in experiments to take an instantaneous picture of the cloud. A comparison of time-averaged and instantaneous display is provided in Figure 7.

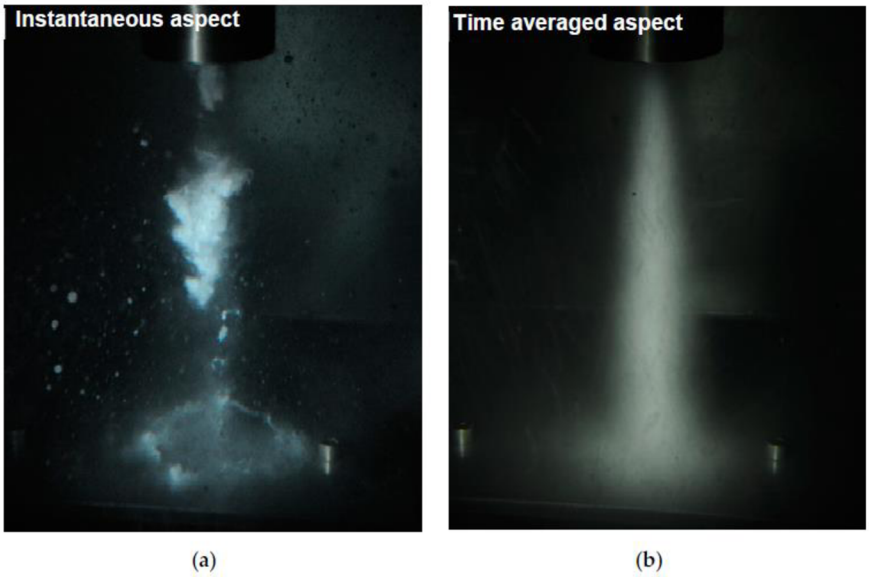

Figure 7: Instantaneous display (a) versus time-averaged display of cavitating jet [13]

Cavitating jet can be induced in water, but also in air, which is mainly performed by means of injecting high-speed water jet into low-speed water jet, see Figure 8 (taken from [13]).

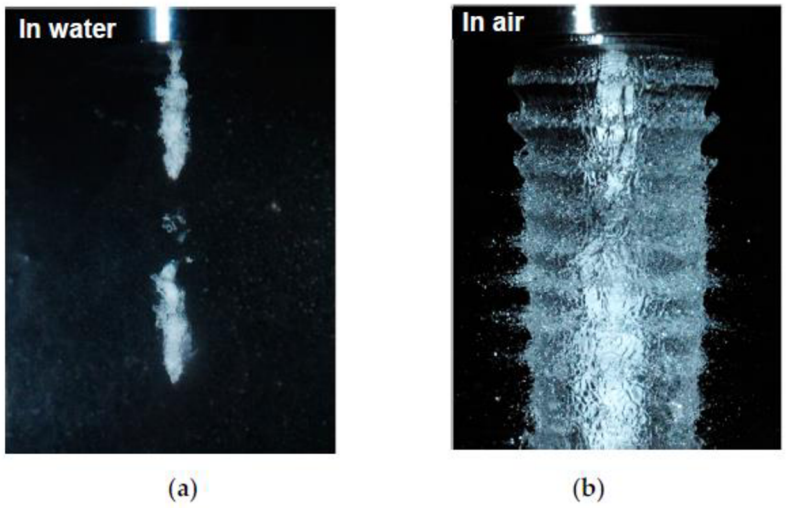

Figure 8: Cavitating jet in water (a) and in air (b) [13]

Cavitating jet development was thoroughly experimentally and numerically investigated in the study by Soyama, bringing an interesting description of this phenomenon, see Figure 9 [13].

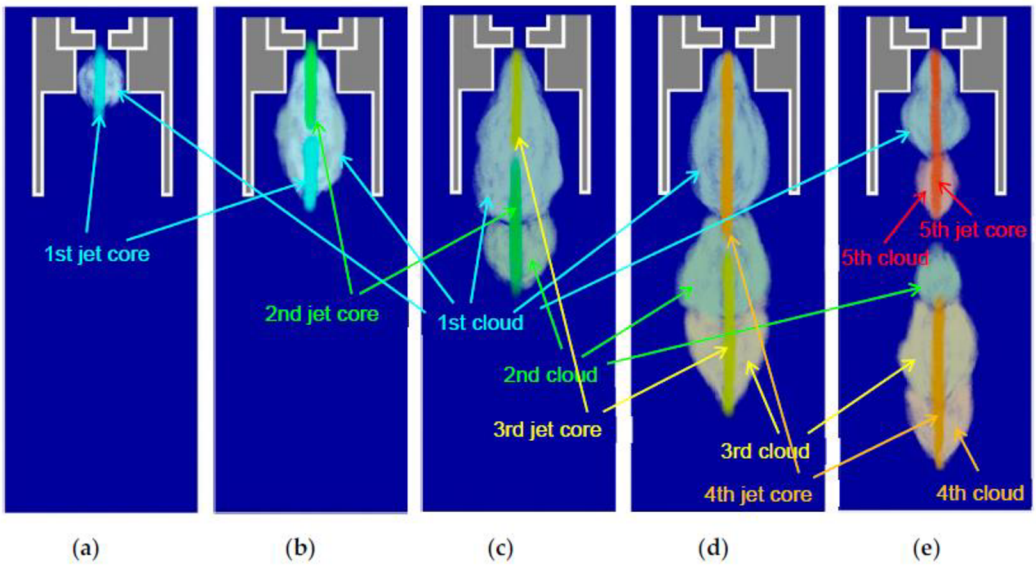

Figure 9: Development of cavitating jet [13]

Cavitating jet development starts with an emergence of the first jet core, which leads to a creation of the first cloud. Afterwards, second jet core is induced and it flows through the first cloud. Consequently, second cloud and third core jet are created. Subsequently, the process is repeated and fourth and fifth jet cores and clouds occur, creating rather complicated unstable structure. The impacts to the surface cause typical ring distribution of pits as presented in Figure 24. It is important to note, that whereas the ring itself is of cavitation origin, the damage in the center is caused by the jet and therefore, it is not directly evoked by cavitation impacts.

Another interesting remark made by Soyama is that cavitation clouds with longer lifetime cause more severe damage to the material, as the cavitation intensity is larger in that case.

As for the typical ring distribution of the pits, it is necessary to look into the cavitation collapse more thoroughly. As mentioned above, there is a big difference between instantaneous and time-averaged display of the cavitating jet. According to the research conducted by Soyama, the ring shape of the impacted area on the sample surface is not caused by swirls in the shear region of the jet as it was formerly thought, when high-speed cameras were not so wide-spread and only time-averaged displays were available. As a matter of fact, the ring shaped damage is rather induced by ring vortex cavitation which is formed from cloud cavitation. Those cavitation clouds meld together below a region with vortex cavitation, which is located just behind the nozzle outlet. The comparison of the described effects is presented in Figure 10.

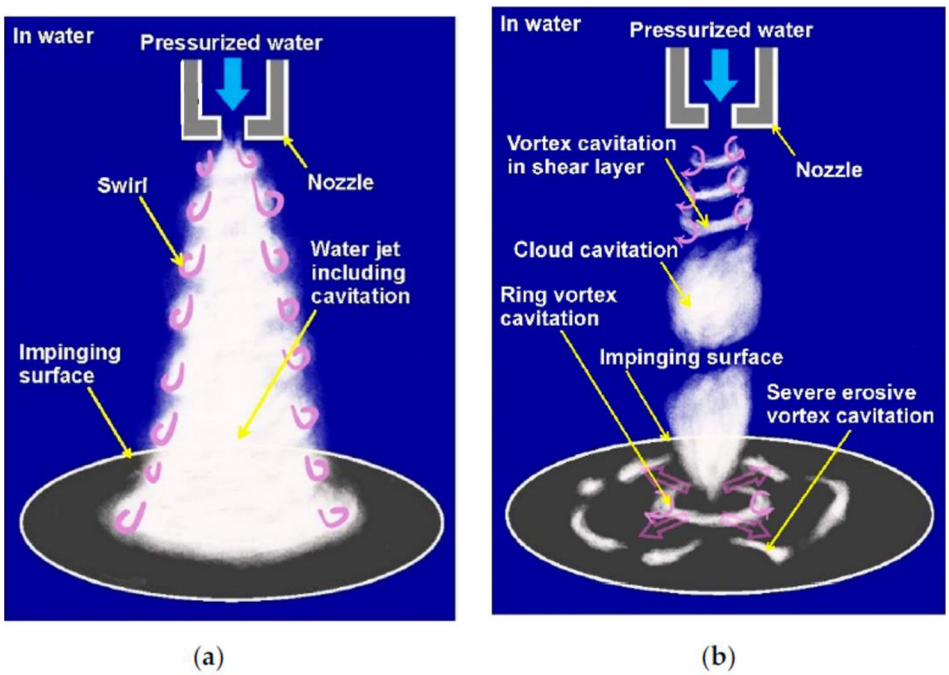

Figure 10: Cavitation damage induced by swirl (a) – incorrect, damage created by ring vortex cavitation (b) – correct [13]

To better understand the complicated processes during cavitating jet development, a cavitation number and local cavitation should be defined. The cavitation number can be expressed as:

$$\sigma = \frac{p_2 - p_v}{p_1 - p_2} \tag{4}$$

where p_1 is the injection pressure (upstream the nozzle), p_2 is the pressure in the tank (usually equaled to atmospheric pressure) and p_v is saturated vapor pressure. As it holds that $p_1 >> p_2 >> p_v$, the equation above can be simplified to:

$$\sigma \approx \frac{p_2}{p_1} \tag{5}$$

Local cavitation number σ_L is connected to a certain point on the impacted surface and is defined by the maximal pressure p_{max} (which is located in the jet center), pressure p at the given position and maximal velocity v_{max}. Velocity has zero value in the jet center and its maximum lies at a certain distance from the jet center, therefore, it is obvious that it is a function of radius and also of a pressure difference between p_{max} and p_2. Those considerations are brought together in the following equation:

$$\sigma_L \propto \frac{p - p_v}{\frac{1}{2} \cdot \rho \cdot v_{\max}^2} \propto \frac{p - p_v}{p_{\max} - p_2} f(r) \tag{6}$$

In Figure 11, a dependency of pressure, velocity and local cavitation number on radius is displayed.

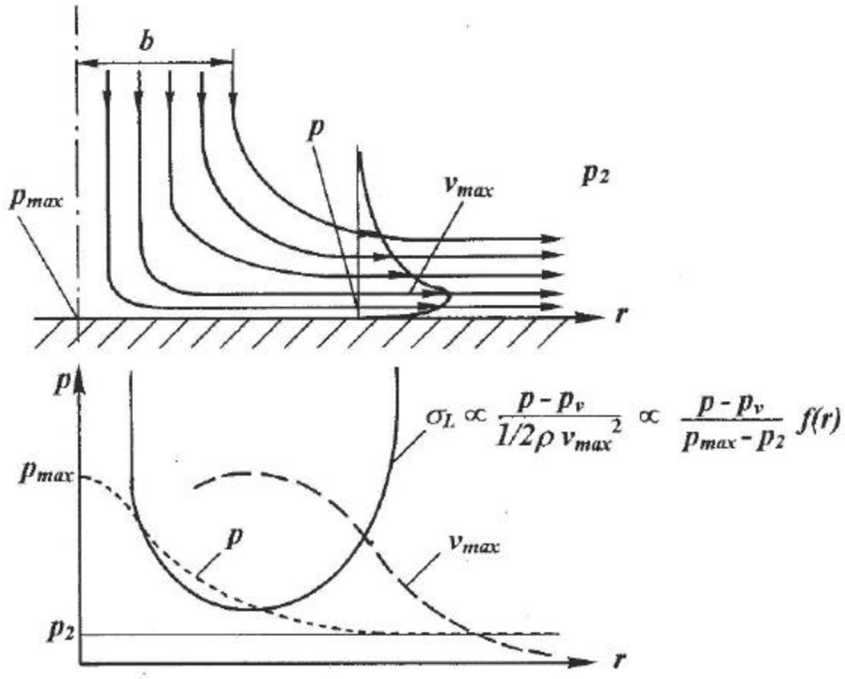

Figure 11: Local cavitation number [23]

It can be seen from Figure 11, that the local cavitation number has a minimum value at a location with maximal velocity and at this point ($\partial\sigma_L/\partial r \approx 0$), the ring vortex cavitation collapses. At locations with ($\partial\sigma_L/\partial r < 0$), the cavitation develops.

Nishimura, Takakuwa and Soyama have conducted experiments [24] to investigate a dependency of shedding frequency of cavitation clouds on pressure p_1, diameter of the nozzle d, and on cavitation number σ. It was found out, that the shedding frequency increases with increasing pressure p_1 and also with increasing cavitation number σ, however, it decreases with the increasing nozzle diameter d. Another important conclusion, which was drawn from this study, is that Strouhal number, which is defined by the shedding frequency of the cavitation cloud, its characteristic length and velocity at the nozzle outlet, is constant. However, it changes with various nozzle outlet geometry.

Cavitating jet is influenced by the type of the cavitation jet, standoff distance, injection pressure, cavitation number, speed of sound and water qualities. These effects will be thoroughly described in the following subsections.

1.3.1 Influence of cavitation type

As mentioned above, cavitating jet can develop not only in water, but also in air. In case of cavitating jet in water, compressive residual stresses are in deeper locations, whereas in the other case (cavitating jet in air), these stresses are more shallow (but large), see Figure 12.

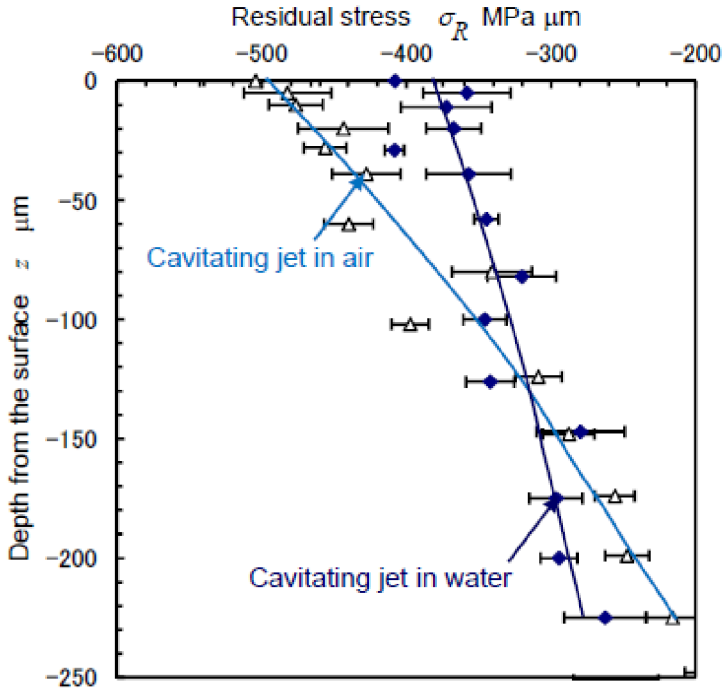

Figure 12: Compressive residual stresses [25]

1.3.2 Influence of standoff distance

This subchapter is of a great importance, as it shows the significance of standoff distance (that is the distance between the nozzle outlet and the sample). According to Soyama [13], in case of short standoff distances, the damage of the surface is not caused by cavitation erosion, but by a mechanism known as water jet cutting, which is sometimes used in manufacturing processes. Since the standoff distance is short, the cavitation does not have enough space to develop entirely. However, in case of larger standoff distances, the prevailing mechanism of erosion is cavitation. Naturally, there is also an influence of the cavitation number, which is affected by upstream and downstream pressure. Soyama [13] conducted many experiments to investigate this issue. Figure 13 summarizes his results in a form of a diagram presenting a dependency of weight loss on the standoff distance. The experiments were conducted at constant pressure upstream the nozzle (p_1=120 bar) and downstream pressure p_2 was being changed to obtain different cavitation numbers. For each case, two distinguishable peaks of weight loss can be observed – the first one at short standoff distances is related to the water jet cutting, and the second one is connected to cavitation erosion. The first peak remained almost the same for all of the cases, however, the second peak was changing with cavitation number. Also, the standoff distance, at which the second peak related to cavitation erosion appeared, was influenced by cavitation number. It can be seen, that in case of p_2=2.4 bar and σ=0.02 (the most aggressive cavitation of the presented cases), the second peak was much larger than the first one. On the other hand, in case of p_2=3.6 bar and σ=0.03 (the least aggressive cavitation), the first peak was

higher than the second one and therefore, the water jet cutting was more significant than cavitation erosion at this downstream pressure.

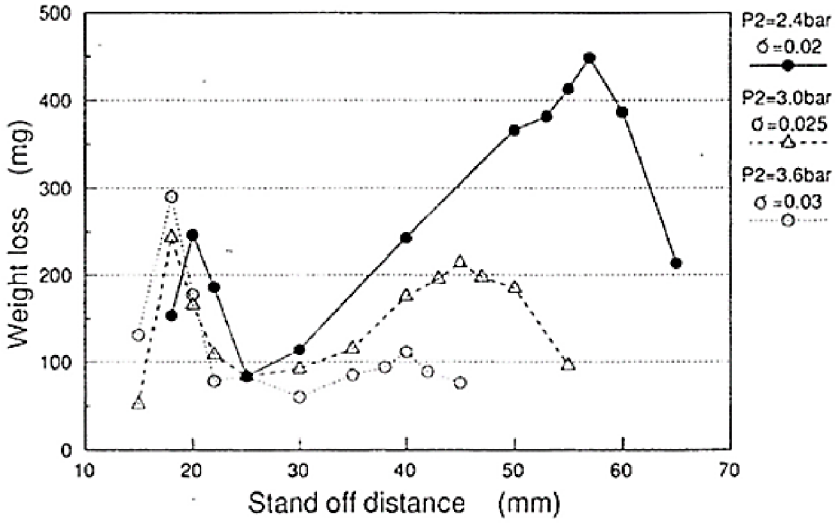

Figure 13: Weight loss dependent on the standoff distance [13]

Figure 14 shows a comparison of cavitating jet aggressiveness (as an inverse of the curvature radius of the Almen strip[1]) for two cases – one with large nozzle and low injection pressure (blue curve) and the second one with small nozzle and high injection pressure (black curve). In both cases, the downstream pressure remained at a constant value of p_2=1 bar. In the former case one can observe, that the second peak related to the cavitation erosion was much higher than in the latter case. Therefore, the application of large nozzles and relatively low injection pressure leads to more severe surface damage caused by cavitation erosion [25].

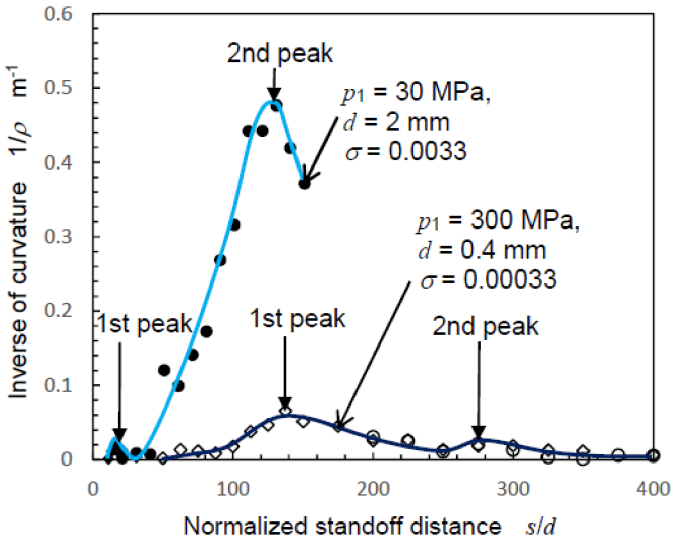

Figure 14: Dependency of cavitating jet aggressiveness (inverse of curvature radius) on the standoff distance [25]

[1] Almen strips are used for determining shot-peening intensity. The narrow steel strip is placed on ball supports and it bends into the shape of arc accordingly to the impacts from shots. Micrometer measures the arc height in order to evaluate the shot-peening intensity [26].

Based on the results from this study and also from many other sources, Soyama [25] has defined a parameter called optimal standoff distance, which approximately separates conditions at which either water jet cutting or cavitation erosion are prevailing mechanisms of the surface erosion:

$$\frac{s_{opt}}{d} = 1.8 \cdot \sigma^{-0.6} \tag{7}$$

At this optimal standoff distance, maxima of weight loss are reached. The prediction of Eq. (18) is included in the following diagram presenting a classification map for cavitation peening (cavitation erosion) and water jet peening (cutting):

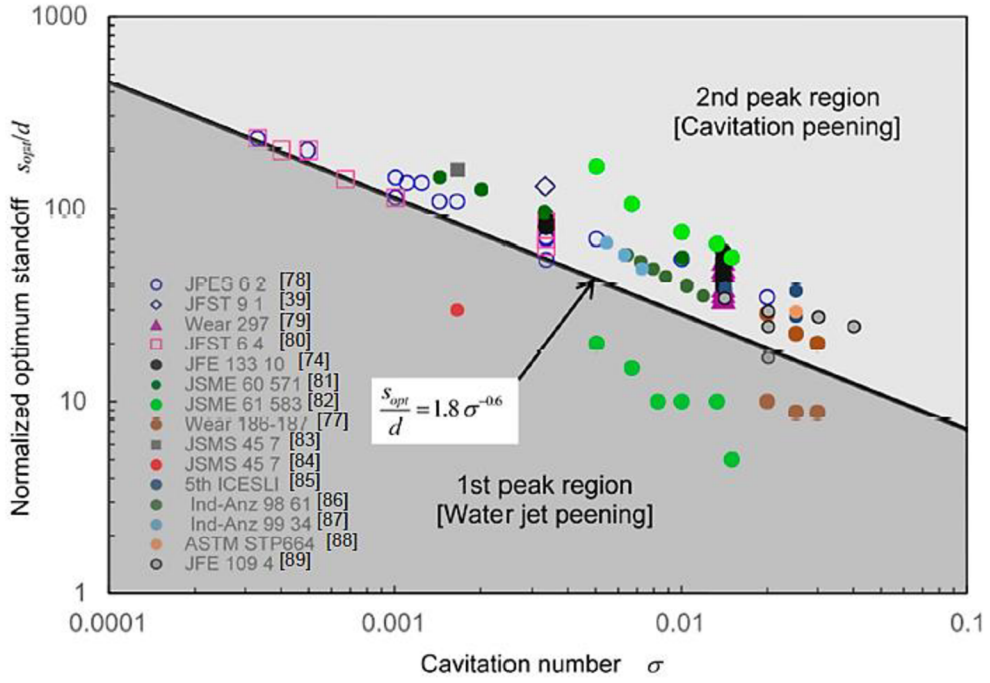

Figure 15: Classification map for cavitation erosion and water jet cutting [25]

It can be seen from Figure 15, that in case of low cavitation numbers (the most aggressive cavitation), sufficient standoff distance has to be ensured in order to enable the cavitation to develop. To confirm that the cavitation erosion occurred, the cavitating jet experiment can be conducted at the chosen conditions, and if the ring shape of the damaged area develops on the sample surface, then the conditions fall into the region for creation of cavitation peening.

1.3.3 Influence of injection pressure

The influence of injection pressure was partly introduced in Figure 14, where it was concluded that large nozzles and low injection pressure easier induce more intensive cavitation erosion than small nozzles and high injection pressure. Soyama [13] continued to investigate this effect and compared the effect of injection pressure on the effectivity of water jet peening and cavitation erosion, see Figure 16. The experiments were again conducted at constant downstream pressure and Almen strips were used to determine the peening intensity. The quantity called processing capability β [27] is similar to the inverse of curvature radius in Figure

14, but it also includes the influence of steel width and peening width. Nonetheless, once again, it expresses the aggressiveness of cavitating jet.

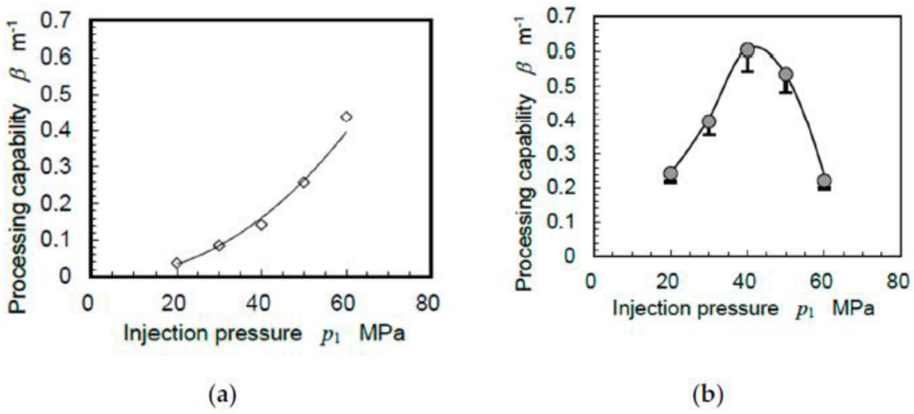

Figure 16: Aggressiveness of the cavitating jet (as an processing capability) as a function of injection pressure for water jet peening (a) and cavitation peening (b) [27]

It can be seen from Figure 16, that in case of water jet peening (a), the aggressiveness of the cavitating jet increases with the injection pressure. In case of cavitation peening (b), the processing capability increases with the increasing pressure until it reaches its maximum. In this case, the maximum lies at pressure p_1=40 MPa, where the processing capability reached 1.7 times higher value than for water jet peening at the same pressure. However, with the further increase of pressure, the aggressiveness of the cavitating jet decreases, which is probably caused by the simultaneous decrease in speed of sound.

1.3.4 Influence of cavitation number

The influence of the cavitation number is already clear from Figure 15 and Eq. (18) for optimal standoff distance. Figure 17 summarizes the relationship between the cavitation number and the standoff distance.

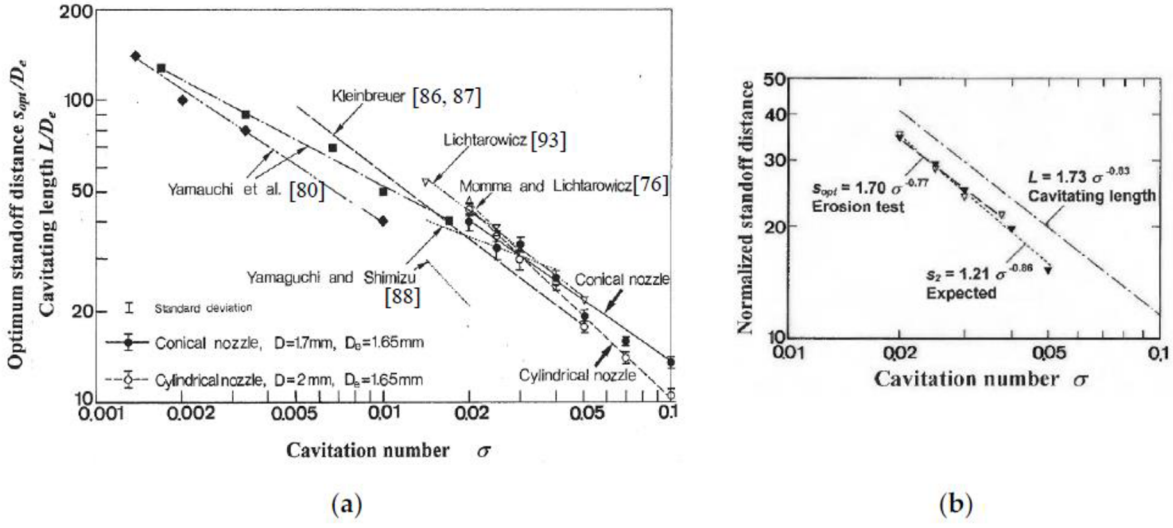

Figure 17: Standoff distance (and cavitating length) as a function of cavitation number (a), local cavitation number (b) [28]

The relation between cavitation number and standoff distance can be generally expressed as:

$$\frac{s_{opt}}{d} = c_1 \cdot \sigma^{-c_2} \tag{8}$$

Therefore, it is obvious, that with increasing cavitation number, the optimal standoff distance, which is required for full cavitation development, decreases.

1.3.5 Influence of speed of sound

Soyama [13] studied the influence of speed of sound on the aggressiveness of the cavitating jet in an experiment with Venturi tube. Figure 18 presents a dependency of speed of sound on the cavitation number. Clearly, the speed of sound increases with the cavitation number.

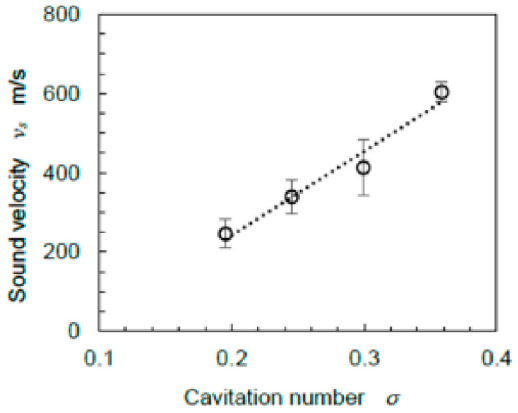

Figure 18: Velocity of sound as a function of cavitation number [13]

Two conflicting tendencies were found out: 1) with an increase of the cavitation number, the speed of sound increases too, meaning that the cavitation erosion rate is higher, 2) an increase of cavitation number leads to a lower intensity of cavitation erosion rate. As the two theories contradict each other, there is a certain peak of cavitation aggressiveness for a given cavitation number, which is presented in Figure 19. The maximum cavitation intensity is reached for cavitation number of a value between 0.01 and 0.02.

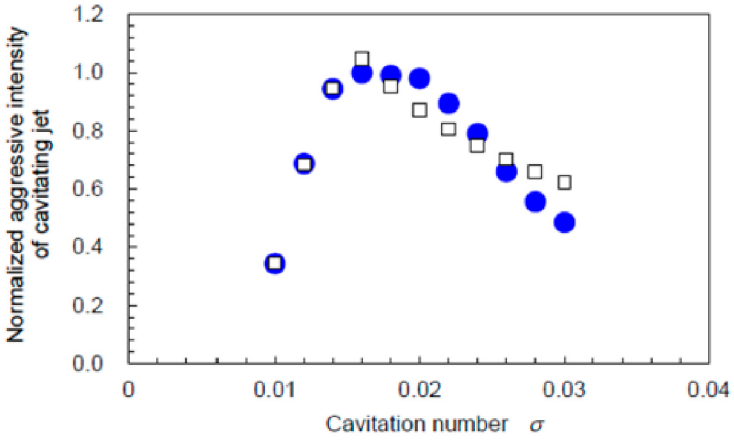

Figure 19: Normalized cavitation intensity as a function of cavitation number; blue dots correspond to the experiment, the white squares were obtained from following equations [13]

In Figure 19, a property called normalized cavitation intensity is presented. The normalization lies in dividing the cavitation intensity by its maximal value. Cavitation intensity can be defined as:

$$I_{cav} \propto \left(L_{cav}\right)^3 \cdot \left(p_2 - p_v\right) \cdot \left(v_s - v_{s,th}\right) \cdot \left(\sqrt{p_1 - p_2}\right)^n , \tag{9}$$

where $(L_{cav})^3$ is the cavitation volume, v_s is the speed of sound, $v_{s,th}$ is the threshold value of speed of sound corresponding to threshold value of cavitation intensity and the pressures were already described above. It was found out, that n=3 and the volume of cavitation can be expressed with the help of Equation (8). Then the Equation (9) can be rewritten as:

$$I_{cav} = c_3 \sigma^{-1.8} \cdot \left(p_2 - p_v\right) \cdot \left(v_s - v_{s,th}\right) \cdot \left(\sqrt{p_1 - p_2}\right)^3 , \tag{10}$$

where c_3 is a constant. It can be seen from Figure 19, that the experimental and numerical data are in good agreement.

Low cavitation intensity at low cavitation numbers is probably caused by a decrease of speed of sound at too high injection pressure.

1.3.6 Influence of nozzle geometry and diameter

The influence of the nozzle diameter was already discussed above with the conclusion that large nozzle (and relatively low injection pressure) cause more severe cavitation damage than small nozzle (and high injection pressure). The influence of nozzle geometry on the cavitation intensity is illustrated in Figure 20.

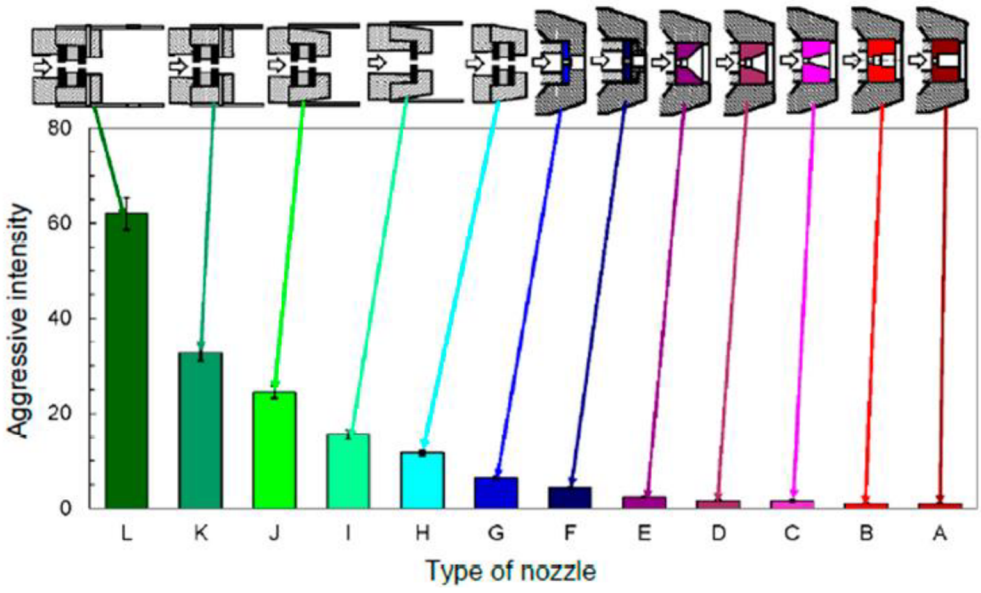

Figure 20: Aggressiveness of cavitation as a function of nozzle geometry [13]

Nozzles A-E are standard nozzles for water jets. Nozzle I and J were equipped with a guide pipe and a cavitator, which is in principle a rotor equipped with cavities. As the cavitator rotates, cavitation is induced in the cavities. This principle is usually used in mixing and heating technologies, where cavitation intensity is controlled in order to avoid destructive potential of

cavitation [29]. In case of nozzle K, water flow holes near nozzle outlet were installed. Nozzle L is also equipped with water flow holes, but in addition, also with a guide pipe. Flow in water flow holes is wrapped around the cavitating jet, leading to an increase of cavitation impact force [30]. In Figure 21, a cavitator and water flow holes are depicted.

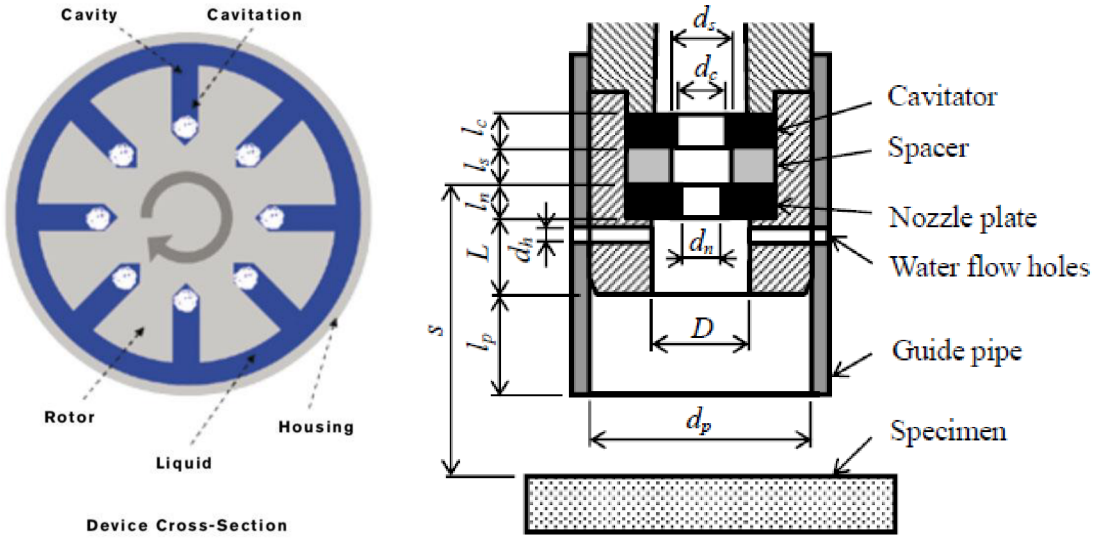

Figure 21: Cavitator (left) [29], nozzle with water flow holes (right) [30]

1.3.7 Influence of water qualities

As mentioned in Chapter 1.2.1, water temperature affects the conditions for cavitation inception. However, small temperature differences (288-308 K, according to [15]) should not cause a significant change in the erosion intensity of cavitating jet.

Concerning the gas content, a small content is usually required as it serves as cavitation nuclei. However, if there are too many air bubbles, the cavitation intensity is reduced as the speed of sound decreases.

1.4 Material erosion

On account of the cavitation collapse mechanisms described above, plastic deformation occurs in material and consequently, grains of material are being gradually chipped off from a solid body. Microscopic craters, so-called pits, are one of the first signs of cavitation erosion. Those pits magnify in time and they can be even observed by naked eye. Rougher surfaces are more susceptible to cavitation erosion as the material protrusions are more easily detached from the solid body [1], [8].

Cavitation erosion can occur at all of the materials, including metal, rubber, glass, etc. However, some of the materials are more predisposed to cavitation erosion (e.g. aluminum or nickel alloys) than other (e.g. tungsten). Figure 22 compares several steels and cast iron with respect to the mass loss caused by cavitation and relates it to the hardness of material. It is worth mentioning, that the cavitation can occur not only in water, but also in other liquids as e.g. liquid lithium or mercury [1], [8].

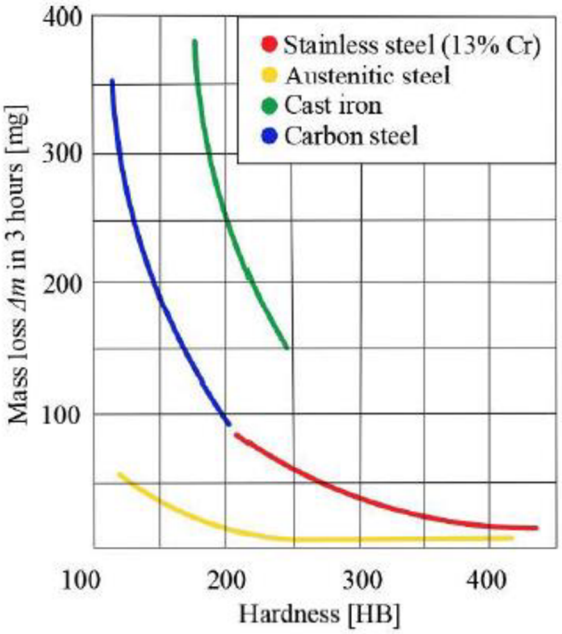

Figure 22: Comparison of mass loss caused by cavitation for various materials, adapted from [14]

Cavitation erosion proceeds in four main stages – incubation, acceleration, deceleration and steady-steady state period. The material loss in the particular phases can be displayed either cumulatively or with help of rate of volume loss over time [12], see Figure 23.

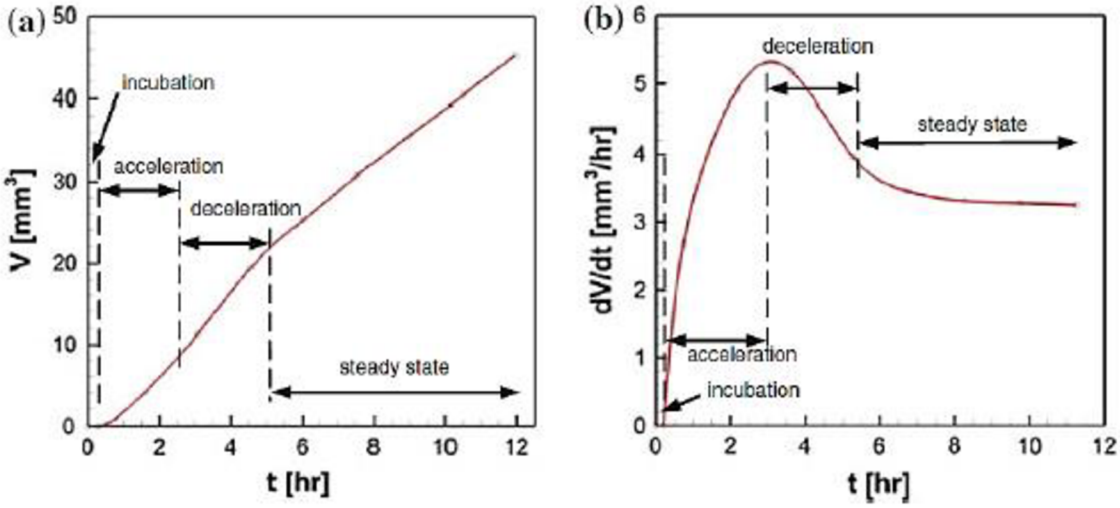

Figure 23: Cumulative volume loss (a), rate of volume loss (b) [2]

In the incubation period, plastic deformation of the material occurs and only very small pits are created. Cavitation impacts during the incubation period can be advantageously used for material treatment, so-called cavitation peening (based on similar principle as shot peening, however, no shots have to be used). Cavitation peening is usually done by cavitating liquids jets and it improves fatigue strength of the given material [12].

During the acceleration period, the highest rate of volume loss of the material occurs. Grains are being removed from the material as large cracks at the grain boundaries emerge [2].

Afterwards, deceleration of volume loss supervenes as a result of weakened cavitation erosion due to gas molecules being trapped in the large pits and craters at the material surface [2].

Consequently, steady-state of volume loss is reached and the cumulative curve is almost linear [2].

Figure 24: Typical ring distribution of pits over the material surface [15]

It is also important to mention, that cavitation erosion is more significant with increasing velocity. This relation can be described using the following equation [12]:

$$\dot{m}_l = K \cdot (v - v_0)^n, \tag{11}$$

where:

$\dot{m}_l$ is the mass loss of the material,

v is the flow velocity,

v_0 is the lowest velocity at which cavitation still occurs,

n is exponent of the velocities difference and it ranges from 4 to 9 (usually around 7)

1.5 Cavitation erosion models

There are various physical models used for an assessment and a description of cavitation erosion mechanisms. Those models help to understand cavitation collapse and are useful for linking CFD and experimental results to enable prediction of the cavitation erosion only via tools of computational modelling.

1.5.1 Fluid-Structure Interaction Models

These models are based on a connection of cavitation processes in fluid directly with damage on a solid boundary. At first, it is important to recognize the extent and type of cavitation and also its generation rate. Afterwards, number and size of bubbles has to be determined, which is quite a difficult task. Usually, it is estimated from a measurement of air bubble distribution. Pit distribution on the surface of a sample is evaluated to estimate the erosion rate. Impact pressure itself is determined using a model of single bubble implosion in an infinite space. Eventually, the distribution of impact forces and pressure is estimated according to the pit distribution, the cavity generation rate and the number and size of bubbles [17], [18].

Fluid-structure interaction models are of a quantitative kind, which can be useful in an industrial praxis. However, they neglect some parameters as e.g. ambient pressure change around the bubble or a value of initial pressure of gas inside the bubble and not many experimental configurations were taken into consideration so far, therefore, more experiments need to be carried out [17].

1.5.2 Eulerian-Lagrangian method

This method of cavitation erosion modelling is based on using Eulerian mechanics for description of the fluid flow on macroscopic scale and Lagrangian approach for modelling the individual bubbles on microscopic scale. Three main equations (continuity, momentum and energy equation) are solved at macroscopic level and the results are used as an input for equation of a bubble oscillation to estimate the change of a bubble radius. Eventually, cavitation erosion rate is determined from the impact pressure caused by the bubble collapse [17].

This method is quite promising as it has a strong theoretical background and it even considers bubble rebounds. Nonetheless, also this method deals with some issues, mainly with the positioning of the bubble injection, which can significantly affect cavitation erosion intensity. Another considerable disadvantage of this method is closely related to its basic principle – the method does not model the whole cavitation cloud but only a single bubble, whose collapse mechanisms are significantly different. Moreover, the cavitation cloud obviously holds more impact energy than the single bubble leading to the different cavitation bubble dynamics and a different rate of erosion. Therefore, the modelling of a single bubble behavior is a rather large simplification as in real applications one cannot observe a single bubble cavitation, but the cavitation cloud [17].

1.5.3 Energy cascade models

Energy cascade models stem from an idea of energy transfer between the collapsing bubble and the surrounding solid body. Cavities dispose of potential energy, which is converted into acoustic energy in form of pressure waves during the cavitation cloud collapse. Those pressure waves are then considered as the main reason for cavitation erosion [16], [17].

According to Bark [19], a global cavity moving through the fluid collapses into small cavities, which are considered to cause pits in the material. This theory considers either pressure waves alone or pressure waves together with micro-jet effect as the main contributors to the material deformation and fatigue.

Probably the best known cavitation erosion model, which is also based on the energy cascade theory, is model proposed by Fortes-Patella [20], [21]. The model claims that the pressure wave itself can be created either by micro-jet, spherical bubble collapse or even vortex collapse. Results from CFD or experiments including the characteristics of the macro cavity development are used as an input for this model. The principle of this method lies in a definition of potential energy of a vapor structure defined as [17], [20], [21]:

$$E_{pot} = \Delta p \cdot V_{vap} = (p_d - p_v) \cdot V_{vap}, \tag{12}$$

where p_d is the driving pressure of the cavity collapse, p_v is the saturated vapor pressure and V_{vap} is the volume of the vapor structure. Afterwards, instantaneous potential power P_{pot}, can be expressed as a Lagrangian time-derivative of the potential energy:

$$P_{pot} = \frac{DE_{pot}}{Dt} = (p_d - p_v) \cdot \frac{DV_{vap}}{Dt} + \frac{Dp}{Dt} \cdot V_{vap} \tag{13}$$

Instead of using V_{vap}, a volume fraction, related to the volume of one cell V_{cell}, can be defined as:

$$\alpha_v = \frac{V_{vap}}{V_{cell}} \tag{14}$$

Consequently, the potential power of each cell or potential power density, respectively, can be expressed as:

$$P_{den} = \frac{P_{pot}}{V_{cell}} = (p_d - p_v) \cdot \frac{D\alpha_v}{Dt} + \frac{Dp}{Dt} \cdot \alpha_v \tag{15}$$

The second term of the equation above is negligible compared to the first term, therefore the equation can be rewritten as:

$$P_{den} = \frac{P_{pot}}{V_{cell}} = (p_d - p_v) \cdot \frac{D\alpha_v}{Dt} \tag{16}$$

The Lagrangian time-derivatives of the volume fraction can be expressed by the following relation:

$$\frac{D\alpha_v}{Dt} = \frac{\partial \alpha_v}{\partial t} + \nabla \cdot (\alpha_v \cdot u) - \alpha_v \nabla \cdot u, \tag{17}$$

where u stands for the velocity of the flow. The time-dependence of volume fraction can be omitted and the term with divergence is actually the continuity equation, characterized as:

$$\nabla \cdot u = \dot{m} \cdot \left(\frac{1}{\rho_v} - \frac{1}{\rho_l} \right), \tag{18}$$

where ρ_v and ρ_l stand for the density of vapor and liquid, respectively, and mass flow rate is indicated as $\dot{m}$. The equation (17) can be rewritten using the volume fraction and mixture density as:

$$\frac{D\alpha_v}{Dt} = \frac{\dot{m}}{\rho_v} - \alpha_v \cdot \dot{m} \cdot \left(\frac{1}{\rho_v} - \frac{1}{\rho_l} \right) = \dot{m} \cdot \frac{\rho}{\rho_v \cdot \rho_l} \tag{19}$$

Potential power density is then:

$$P_{den} = (p_d - p_v) \cdot \max\left(\dot{m} \frac{\rho}{\rho_v \cdot \rho_l}, 0 \right) \tag{20}$$

The model assumes a point source of power at location *i*, which propagates radially without any energy losses until it reaches a solid surface at position *j*. With the knowledge of position vector $\vec{R}$, the instantaneous power at the time *t* and location *j* can be expressed as:

$$P_{imp}(j,t)\big|_i = P_{den}(i,t) \cdot \frac{1}{2\pi \cdot \left|\vec{R}\right|} \cdot \frac{\vec{R} \cdot \vec{n}}{\left|\vec{R}\right|} \tag{21}$$

The described situation is also depicted in Figure 25.

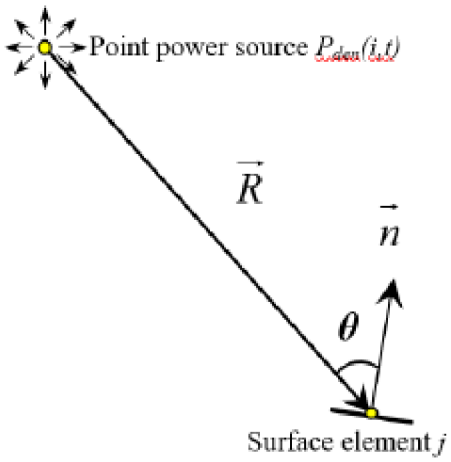

Figure 25: Scheme of point power source and surface element j [17]

By integrating the above equation over the whole surface of the solid body, the total power at location *j* and time *t* from all of the point power sources can be obtained. By comparing this value to the material threshold power, the rate of cavitation erosion can be assessed [17], [20], [21].

Obviously, the significance of the equations above is strongly connected to the driving pressure p_d, which can be taken as an instantaneous value or an averaged value. Another important term is the mass flow rate $\dot{m}$, whose value is related to the cavitation model used in the computation. The study [17] showed that the averaged values of pressure (over ten cycles) led to better agreement with experimental data and concerning the cavitation model, Schnerr-Sauer model outperformed Kunz and Zwart models.

1.5.4 Other cavitation erosion models

According to Dular [16], [22], there are four phases of cavitation erosion starting with cavitation cloud collapse causing pressure waves emissions propagating towards the solid body. As a result, a single cavitation bubble starts to oscillate and micro-jet develops, pointing directly to the solid body and, subsequently, causing a pit in the material.

This model is partly theoretical and partly empirical and it is important to note, that some other authors assume the reversed progress of cavitation collapse – a single implosion leads to an implosion of cavitation cloud (so-called cascade collapse) [16].

2 Experimental part

The following experimental part is focused on cavitation testing using cavitating liquid jet. However, more laboratory methods for cavitation testing exist, as e.g. the vibratory cavitation apparatus (ASTM G32), which uses an ultrasonic horn to induce acoustic cavitation. Another interesting method is high-speed cavitation tunnel, which is suitable in case of highly resistant materials since high velocities can be achieved in this method, and consequently, also a greater intensity of cavitation. These methods are described in detail in [2].

Results from the experiment are presented in the form of mass loss dependency on time. In addition, thanks to the cooperation with scientists from CEITEC, the surface sample was assessed by surface topography and profilometry. Moreover, the eroded surface and the eroded particles themselves were studied using Scanning Electron Microscope (SEM). These data enable us to better comprehend the processes ongoing during the cavitation erosion. Furthermore, a cavitation visualization using high-speed camera was performed, hence, the shedding frequency of the cavitating jet could be determined.

2.1 Description of the experimental stand

Recently, a new experimental stand for the cavitating liquid jet test was designed at OFIVK FME BUT Brno in order to more accurately realize requirements presented in norms for ASTM G134 test. The following section is devoted to the description of the new experimental stand.

The new experimental stand includes a removable frame, which enables a rather comfortable manipulation with the sample without the necessity of emptying the tank. The testing chamber itself is of the following dimensions: 500x500x500 mm, and is entirely made of glass in order to make it possible to observe the experiment easily. The testing chamber includes a weir, hence, there is a constant water level. A pump, which is used for water supply to the testing section, is not a part of the stand itself, as it could cause unwanted vibrations. The new testing stand is depicted in Figure 26, [31].

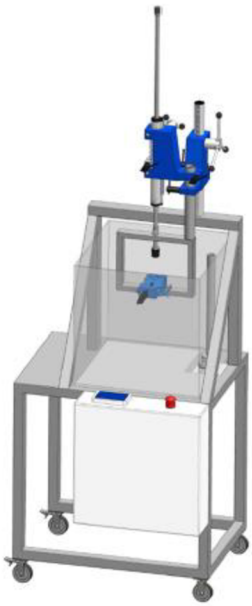

Figure 26: The new experimental stand – mobile and compact solution [31]

In Figure 27, the construction of the removable frame is presented.

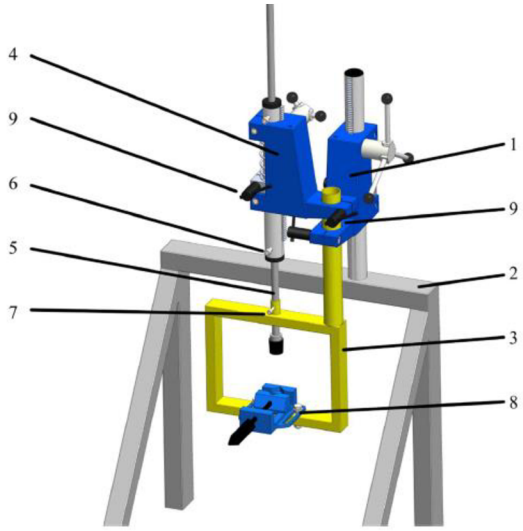

Figure 27: The removable frame [31]

The testing set-up is equipped with two drilling stands. The first one (1) is mounted on the supporting construction (2) by screws and it enables the motion of the removable frame (3) with a gripper (8), which serves to vise a sample. The second drilling stand (4) provides the motion of the nozzle (5), which is supported by an interposer bar (6). Locking screws (7,9) ensure arresting of the particular components [31].

At the beginning of the experiment, the removable frame is put out from the testing chamber by using the first drilling stand. Afterwards, the sample is vised into the gripper and the required standoff distance between nozzle and sample is set. The standoff distance remains the same during the whole test, therefore, it is not necessary to set it again after manipulating with the sample. Arresting screws are locked to make sure that the components stay in place during the experiment. Consequently, the frame is submerged into water, the locking screws arrest the position of the drilling stand and the test can proceed. After a certain period of time, the removable frame is emerged from water, the sample is removed and weighted in order to observe the mass loss [31].

The whole testing circuit is depicted in Figure 28.

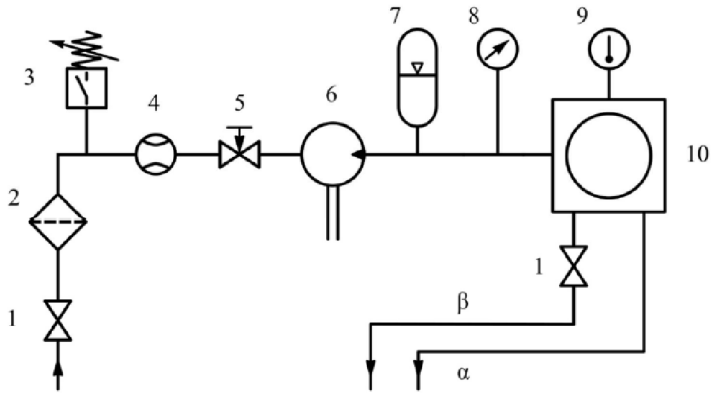

Figure 28: The whole testing circuit - (1) shut-off valve, (2) filter, (3) pressure switch, (4) flowmeter, (5) control valve, (6) pump, (7) hydraulic accumulator, (8) pressure gauge, (9) thermometer and (10) test chamber [31]

The testing circuit is equipped with a shut-off valve, a control valve and a hydraulic accumulator to ensure a safe operation. Measuring devices include a flowmeter, a pressure gauge and a thermometer (to determine the saturated vapor pressure). Water is pumped from the basement tank into the testing section, which is equipped with two outflow sections – the section α is connected to a weir ensuring the constant water level and the section β enables emptying of the testing section [31].

The following section is devoted to the specification of the measuring devices used in the experiment.

Table 2: Technical parameters of the piston pump INTERPUMP E2B2014 [32]

Piston pump INTERPUMP E2B2014	
Maximum output pressure	200 bar
Maximum flow rate	14 $l \cdot min^{-1}$
Revolutions per minute	1450

Table 3: Technical parameters of the pressure sensor DMK 331 P by BD SENSORS [33]

Pressure sensor DMK 331 P	
Nominal pressure rel./abs.	100 bar
Overloading	200 bar
Destruction pressure	250 bar
Accuracy	±0.5 %

Table 4: Magnetic-inductive flowmeter MQI 99 – SN by ELA [34]

Magnetic-inductive flowmeter MQI 99 – SN	
Maximal flow.	0.5 l/s
Standard pressure	40 bar (4 MPa)
Operating temperature	-20 ÷ +60 °C
Principle	Pulse, direct

2.2 Test conditions and sample

The nozzle with a diameter of 1.2 mm was submerged approximately 6 cm below a water level and the pressure $p_{1,\,abs}$ behind the pump (respectively ahead of the nozzle) was set to 180 bar. Consequently, the cavitation number for the cavitating liquid jet test was evaluated using the following equation:

$$\sigma = \frac{p_{2,\,abs}}{p_{1,\,abs}} = \frac{1}{180} = 0.00\bar{5}, \tag{22}$$

where $p_{2,\,abs}$ is pressure in the water tank (≈ atmospheric pressure). As the cavitation number is significantly low, it can be concluded, that the cavitation in the test was rather aggressive and intense.

The optimal standoff distance was calculated using Eq. 18 as s_{opt}=48.71 mm and it was round up to 50 mm to ensure that cavitation peening really takes place and the material erosion is caused mainly by cavitation and not by water jet cutting.

Flow through the nozzle measured by the electromagnetic flowmeter reached an average value of 12.16 l/min, which is a little bit lower value than it is stated by the nozzle manufacturer (according to the nozzle catalogue, the flowrate should reach a value of 12.58 l/min for the pressure of 180 bar [36]).

The water temperature was on the average approximately 14 °C, therefore, according to Eq. 1, the water vapor pressure was calculated as 1580 Pa. However, the real value might be higher due to dissolved air.

The material under the test was copper employed in electrical circuits. Therefore, it should be almost pure copper with just a trace amount of other chemical elements, which should not have a marked influence on the copper properties. Copper sample was not chosen because of its great erosion resistivity, on the other hand, the quite low material characteristics of copper were considered as an advantage to complete the full cavitation test in a reasonable time. The dimensions of the sample were approximately 30x30 mm.

Two sets of experiments were carried out – the purpose of the first set was to measure the whole cumulative mass loss curve (the S-curve), and in the second set of measurement, it was intended to subject the sample only to the incubation period, therefore pits' distribution and dimension characteristics could be obtained with the view of applying the results to the cavitation erosion model.

The first set of experiment took 15 hours. The sample was weighted every 30 minutes at a highly precise scale with an accuracy of hundredths of milligrams and the photos of the progressing cavitation erosion were taken too.

In the second set, two samples were put under the test – the first one was exposed to cavitation for 1 minute, the other one for 5 minutes.

2.3 Results

This chapter is divided into three main sections – the first one is devoted to the results from the first set of measurements, the second section focuses on evaluation of the results obtained from the second set of measurement and the last section contains concluding remarks of the experimental part.

2.3.1 Results from the first set of measurements

This particular subchapter is also divided in multiple sections – the first one focuses directly on the mass loss of the sample caused by the cavitation peening, the second one presents detailed pictures of the sample provided by scientists from CEITEC and the third one describes the cavitation visualization using high-speed camera.

2.3.1.1 Mass loss

It is obvious from the following set of pictures of the sample that the stand-off distance was chosen correctly as there is a visible circular pit region, which is characteristic for cavitation peening as mentioned in Chapter 1.4. In the center of this ring pit region, a material removal by water jet cutting could be observed as it is almost unavoidable part of the material erosion process in the cavitating jet experiment.

First signs of cavitation erosion could be observed even after the first half an hour. During the first two hours of the experiment, the material removal was rather slow and it is possible to assign it to an incubation period. After the first two hours, the material removal accelerated (so-called acceleration period) and the surface of the sample became quite rough, see Figure 29, Figure 30 and Figure 31.

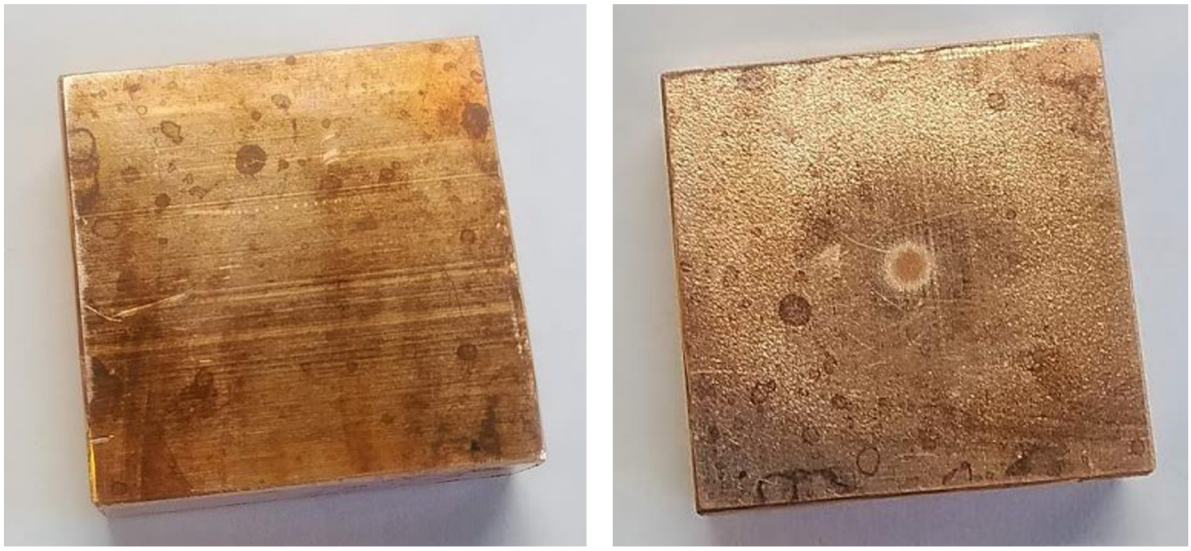

(a) *(b)*

Figure 29: The sample at the beginning of the test (a) and after 0.5 h (b)

(a) *(b)*

Figure 30: The sample after 1 h (a) and after 2 h of the test (b)

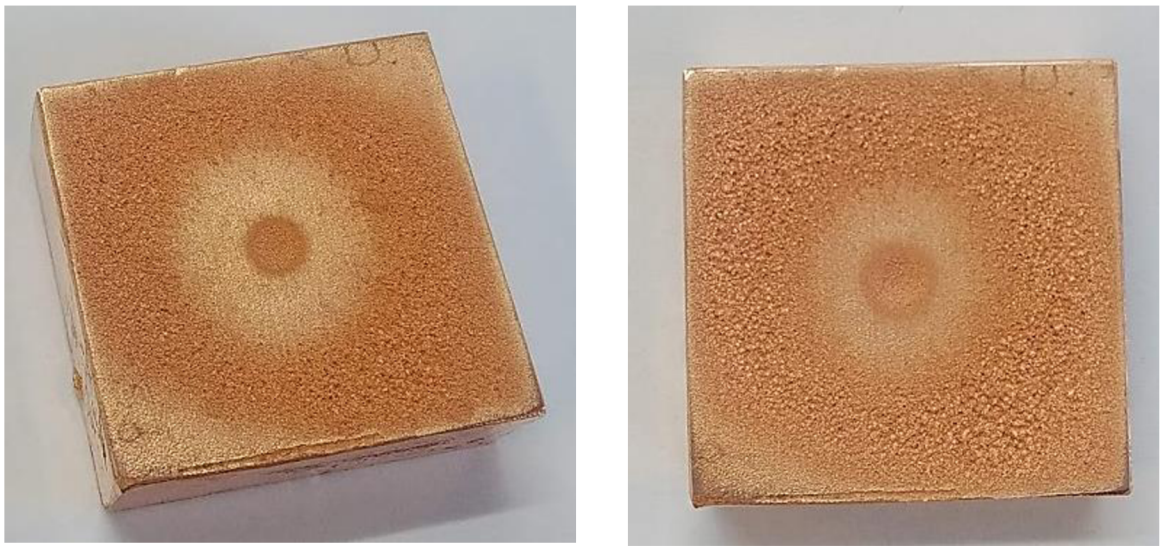

(a) *(b)*

Figure 31: The sample after 4 h (a) and after 6 h of the test (b)

After approximately 8 hours of the experiment, the material removal slowed down a little bit and the cavitation erosion came to the deceleration period. However, the mass loss was still rather significant and the surface of the sample got even rougher as it can be seen in Figure 32.

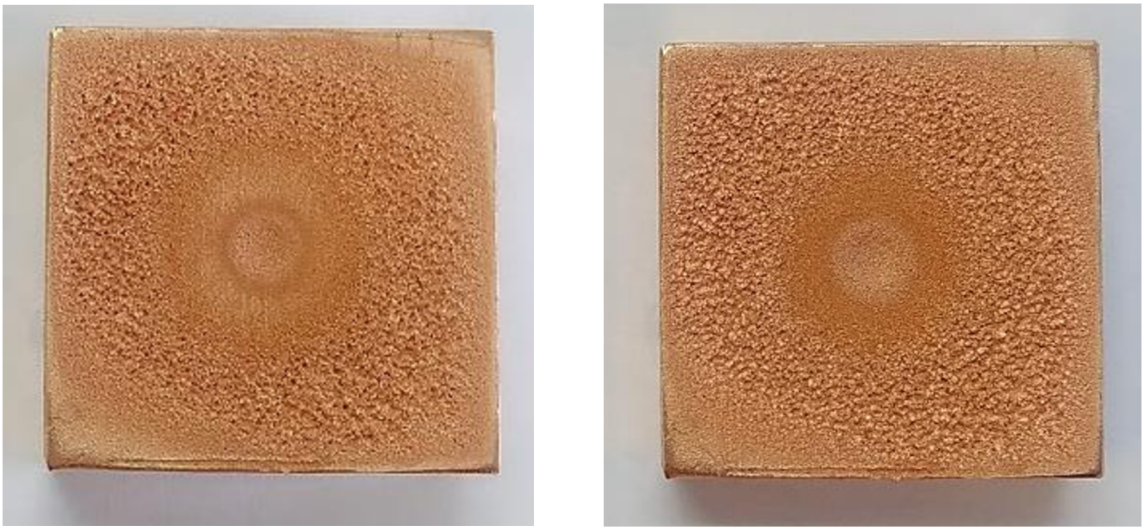

(a) (b)

Figure 32: The sample after 8 h (a) and after 10 h of the test (b)

After another 2 hours, the mass loss reached approximately constant value over the measured time periods, therefore the cavitation erosion process could be characterized as a steady-state process. The experiment was terminated after 15 hours, when a very large pit region was obtained, see Figure 33 (b).

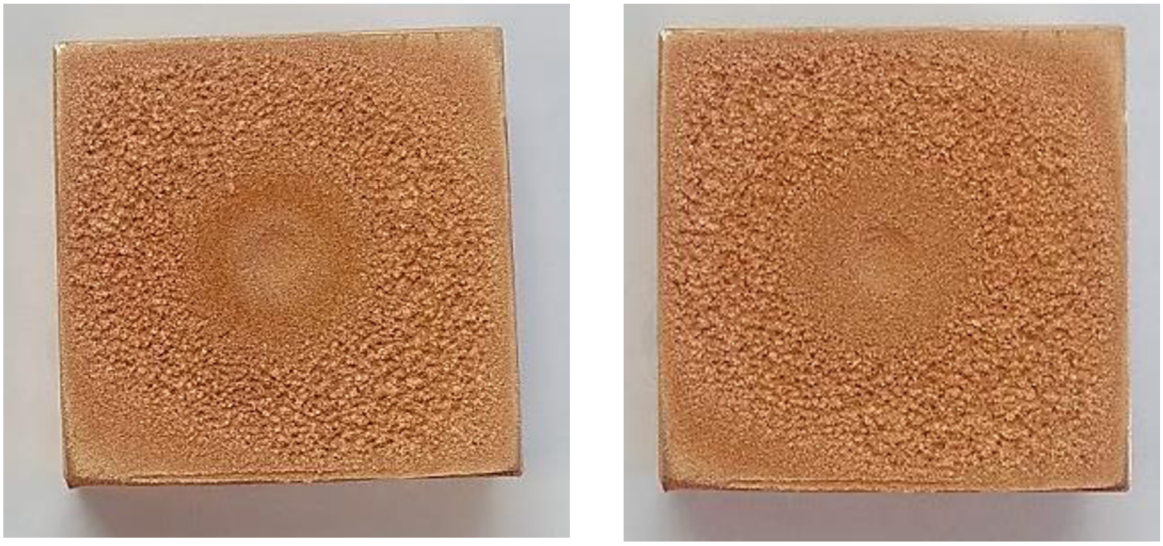

(a) (b)

Figure 33: The sample after 12 h (a) and at the end of test - after 15 h (b)

As mentioned above, the sample was continuously weighted every 30 minutes and Table 5 presents the measured data. The quantity $\Delta m_{cummulative}$ stands for a cumulative mass loss and it can be seen, that after 15 hours of the experiment, over 1 g of the material was lost as a consequence of the cavitation erosion. The quantity $\Delta m_{partial}$ describes a mass loss between two following measurements. The mass loss rate *dm/dt* was evaluated, too.

Table 5: Results of the experiment

t [min]	Δt [min]	t [h]	m [mg]	m [g]	$\Delta m_{cummulative}$ [g]	$\Delta m_{partial}$ [g]	dm/dt [g/h]
0	0	0	78900.42	78.90042			
30	30	0.5	78899.61	78.89961	0.00081	0.00081	0.001620
60	60	1	78898.52	78.89852	0.0019	0.00109	0.002180
90	90	1.5	78896.86	78.89686	0.00356	0.00166	0.003320
120	120	2	78894.09	78.89409	0.00633	0.00277	0.005540
150	150	2.5	78888.67	78.88867	0.01175	0.00542	0.010840
180	180	3	78876.67	78.87667	0.02375	0.012	0.024000
210	210	3.5	78857.59	78.85759	0.04283	0.01908	0.038160
240	240	4	78833.55	78.83355	0.06687	0.02404	0.048080
270	270	4.5	78805.61	78.80561	0.09481	0.02794	0.055880
300	300	5	78775.06	78.77506	0.12536	0.03055	0.061100
330	330	5.5	78739.45	78.73945	0.16097	0.03561	0.071220
360	360	6	78693.66	78.69366	0.20676	0.04579	0.091580
390	390	6.5	78641.76	78.64176	0.25866	0.0519	0.103800
420	420	7	78588.36	78.58836	0.31206	0.0534	0.106800
450	450	7.5	78537.37	78.53737	0.36305	0.05099	0.101980
480	480	8	78482.04	78.48204	0.41838	0.05533	0.110660
510	510	8.5	78425.45	78.42545	0.47497	0.05659	0.113180
540	540	9	78384.95	78.38495	0.51547	0.0405	0.081000
570	570	9.5	78342.36	78.34236	0.55806	0.04259	0.085180
600	600	10	78283.59	78.28359	0.61683	0.05877	0.117540
630	630	10.5	78225.09	78.22509	0.67533	0.0585	0.117000
660	660	11	78165.61	78.16561	0.73481	0.05948	0.118960
690	690	11.5	78108.17	78.10817	0.79225	0.05744	0.114880
720	720	12	78050.77	78.05077	0.84965	0.0574	0.114800
750	750	12.5	77996.79	77.99679	0.90363	0.05398	0.107960
780	780	13	77941.12	77.94112	0.9593	0.05567	0.111340
810	810	13.5	77886.24	77.88624	1.01418	0.05488	0.109760
840	840	14	77833.92	77.83392	1.0665	0.05232	0.104640
870	870	14.5	77784.09	77.78409	1.11633	0.04983	0.099660
900	900	15	77735.81	77.73581	**1.16461**	0.04828	0.096560

Data from Table 5 are graphically presented below in a form of the cumulative mass loss graph and also as a dependence of the mass loss rate on time.

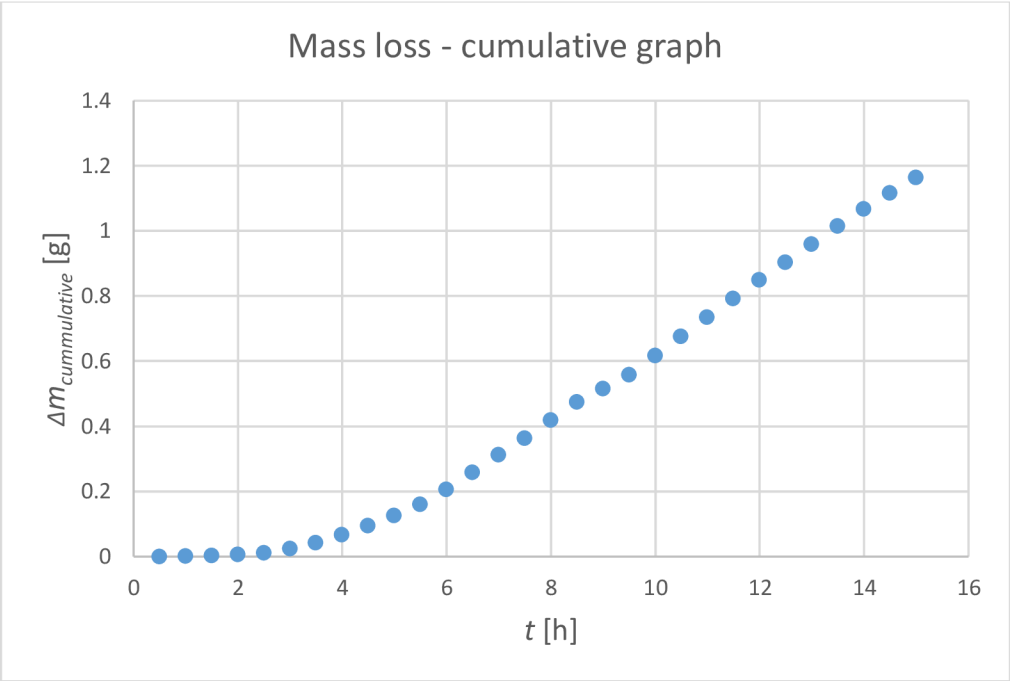

Figure 34: Cumulative mass loss

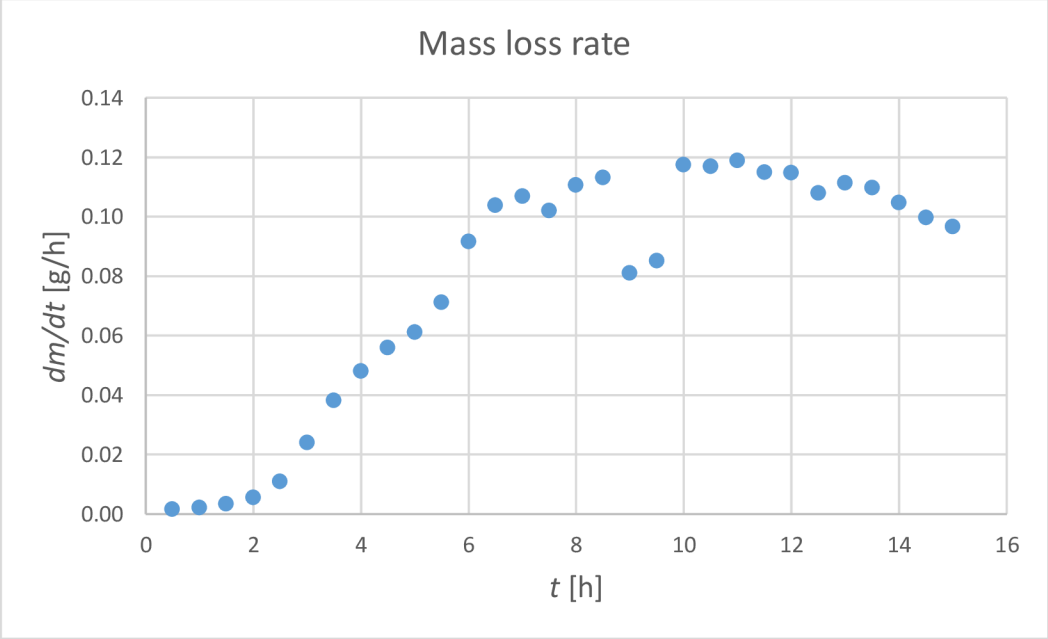

Figure 35: Mass loss rate over time

In Figure 34, a typical cumulative mass loss curve can be observed, the so-called S-curve (resembling very closely the cumulative graph presented in Figure 23 (a) [2]). As mentioned above, the material removal was at first rather small (the incubation period), then it accelerated and the curve obtained a convex course. After approximately 8 hours, it decelerated and the curve was of a concave shape. Then, after altogether 10 hours, the cavitation erosion reached steady-state progress and the curve was almost linear.

Figure 35 presents a dependency of mass loss rate on time. Once again, it can be seen that during the first 2 hours, the mass loss rate was quite low. Consequently, it accelerated rapidly until the 8th hour of the experiment, where a significant drop in the mass loss rate occurred. Since the 10th hour of the experiment, the mass loss rate was approximately constant, corresponding to the steady-state cavitation erosion.

To conclude, the experiment seems to be successful in reaching all the cavitation erosion phases in a reasonable time, which was the aim. Therefore, the copper sample showed as a good choice for this cavitating jet experiment. Another important concluding remark is the confirmation of the equation for the optimal stand-off distance, which ensured that the cavitation peening was the prevailing mechanism of the material erosion as a significant ring shaped pit region occurred on the surface sample. And naturally, the measured data of volume flow rate, pressure and temperate will serve as a basis for defining boundary conditions in the following CFD calculations.

2.3.1.2 Details of the sample surface

To better understand the cavitation erosion mechanisms, various procedures including 3D scanning, profilometry, observation of the sample by Scanning Electron Microscope and the hardness measurements were performed by scientists from CEITEC.

Figure 36 displays the surface topography of the sample after 15 hours of cavitation peening. The ring-shaped eroded area is clearly visible.

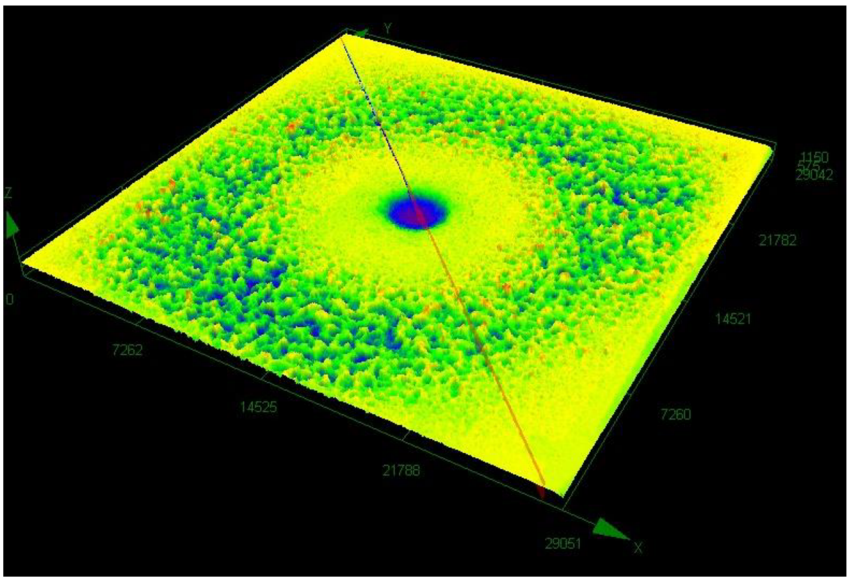

Figure 36: Surface topography of the sample, source: CEITEC

Profilometry of the sample presented in Figure 37 was performed in the region marked as the red line in Figure 36. All the dimensions are in micrometers. Maximum depth of the ring-shaped eroded area (location 2) was determined as 587.36 μm and the depth of the location 1 (directly below the nozzle) was found out to be 692.52 μm.

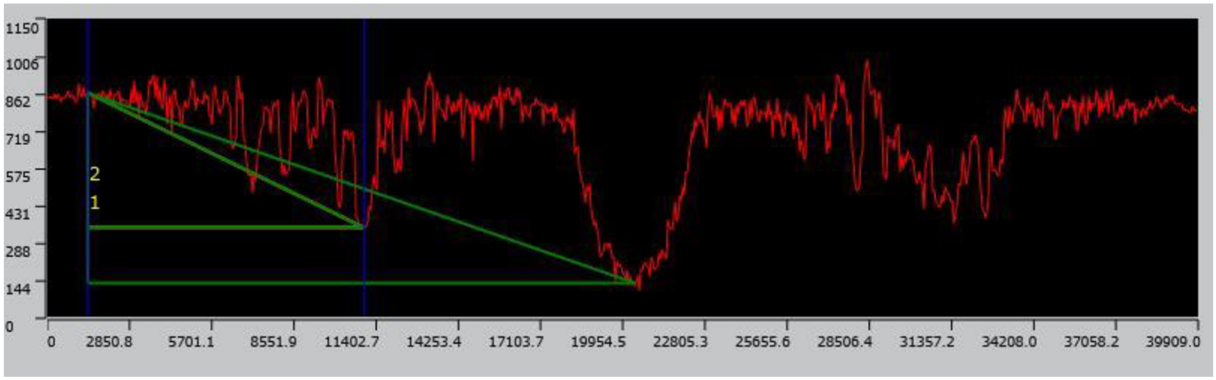

Figure 37: Profilometry of the sample, source: CEITEC

As mentioned above, the surface sample was also observed using Scanning Electron Microscope (SEM) TESCAN LYRA3 XMH. Figure 38 displays details of the surface at the ring-shaped eroded area. Clearly, the material damage is rather severe, and a big amount of small holes created by recurring impacting loads can be observed.

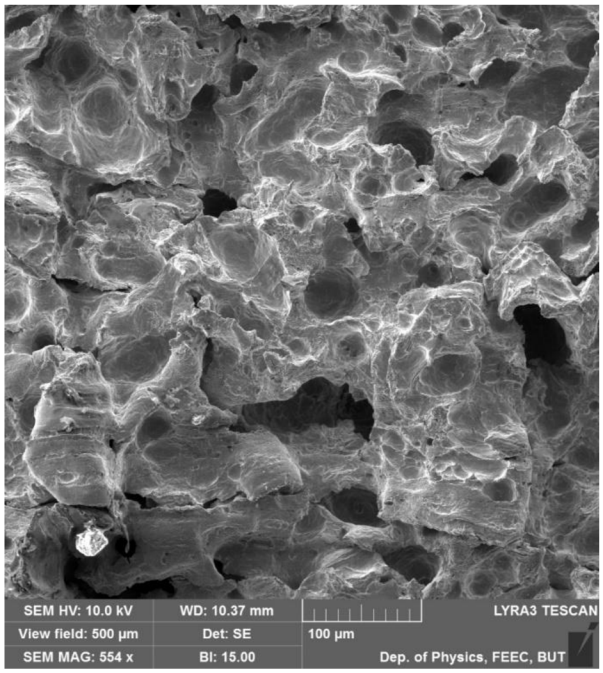

Figure 38: Ring-shaped eroded area of the sample displayed by SEM, source: CEITEC

Figure 39 presents a very unique view of the eroded particles of the sample, which were gathered after the experiment. The width of the individual particles can be determined as approximately 300 μm.

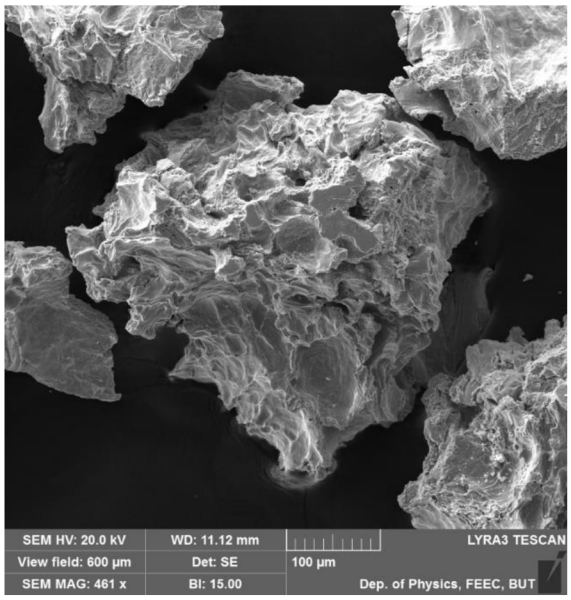

Figure 39: Eroded particles, source: CEITEC

Moreover, the hardness measurements of the sample were performed using the Brinell method according to the particular standard with a result of 86.74 HBW. The hardness value relates to cavitation resistance.

2.3.1.3 Cavitation visualization using high-speed camera

As mentioned above, hydraulic data gathered from the experiment are to be used to set the boundary conditions in Fluent. However, as the simulation of the cavitating liquid jet is of a transient character, it is necessary to set the time-step correctly too. Should the time-step be too long, the dynamics of the cavitation collapse would not be captured. On the other hand, too small time-step would unnecessarily prolong the computation time. Therefore, a visualization of the cavitating jet experiment will be performed to determine the shedding frequency of the cavitation cloud and to set the time-step accordingly. Naturally, this is not the only purpose of the performed visualization, nonetheless, in this thesis, only this kind of information provided by the visualization is going to be elaborated.

High-speed cameras enabled a huge development in the field of cavitation as their high frame rate makes it possible to capture very dynamic phenomena of short time scales. The experimental set-up requires a strong source of light and part of the experimental circuit must be transparent. Light is reflected from the interface between cavitation phases (liquid and vapor). The images are usually captured in grayscale and the changing intensities of the particular pixels can be used to determine the phenomena's frequency by means of Fast Fourier Transformation.

In Table 6, the main characteristics of the high-speed camera FASTCAM SA-Z type 2100K-M-16GB, that was used in the experiment, are presented.

Table 6: Parameters of the FASTCAM SA-Z type 2100K-M-16GB high-speed camera

Record rate [fps] – sampling frequency	60000
Shutter speed [s]	1/200000
Color bit	12
Color type	Mono
Image width x Image height	512 x 512
Total number of frames	4001

Figure 40 displays the experimental set-up with the light source. The stand-off distance and pressure correspond to the values used for the investigation of the mass loss rate (s_{opt}=50 mm and $p_{1,\,abs}$ =180 bar).

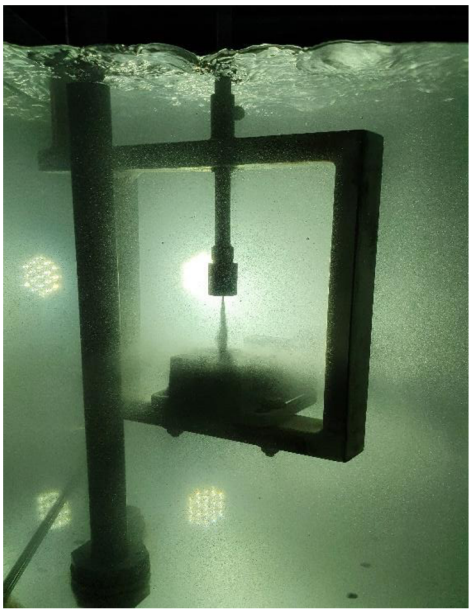

Figure 40: Experimental set-up with the light source

Altogether 9 points (pixels) with certain suitable coordinates (edges of the cavitating liquid jet) were chosen for the analysis of the phenomenon's frequency. A short script in Python was developed to obtain a value of the grayscale at the particular pixel and afterwards, Fast Fourier Transformation (FFT) was performed on these data to obtain a frequency-dependent signal from the original time-dependent domain. The principles of FFT are not going to be described here as it is not the aim of this thesis and FFT was merely used as a helpful tool to determine the cavitating jet shedding frequency. Figure 41 displays the matrix of 9 chosen points at 2 different images of the cavitating liquid jet.

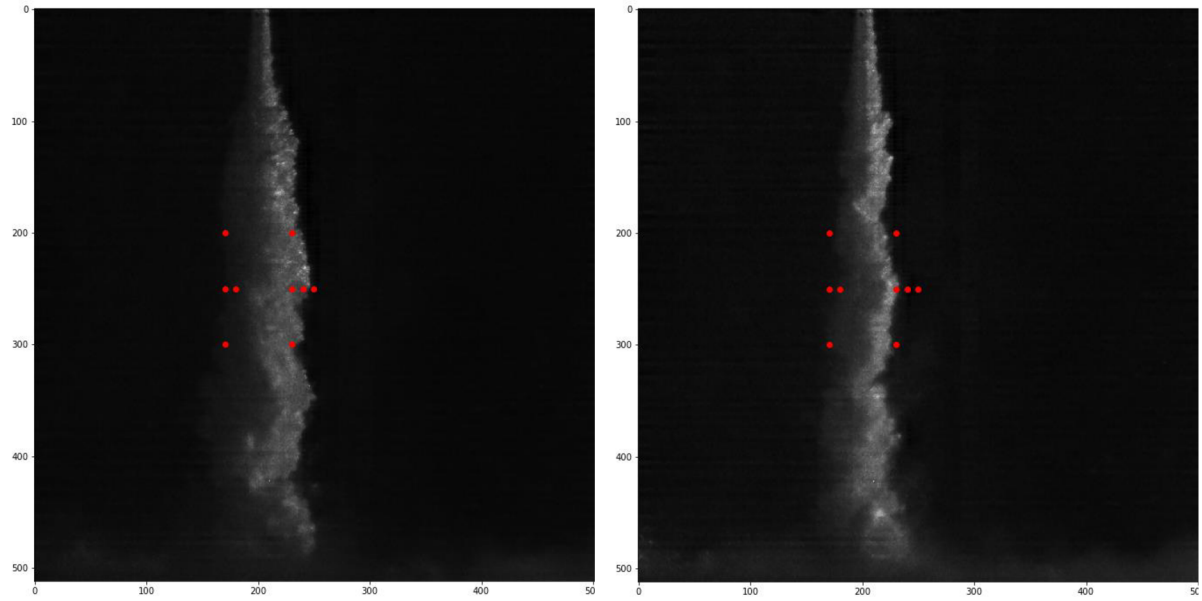

Figure 41: Matrix of 9 chosen points for the analysis

The results from the FFT (frequency of the shedding process) are presented in Table 7.

Table 7: Results from FFT – frequency at the particular pixel coordinate

Pixel coordinate (x_y)	Frequency f_{shedd} [Hz]
170_200	945
170_250	960
170_300	1020
180_250	990
230_200	1290
230_250	1200
230_300	1020
240_250	960
250_250	870

As it can be seen from Table 7, frequencies obtained from different coordinates differ slightly, which is probably caused by additional phenomena of different intensities (e.g. secondary swirling) occurring at those locations. However, generally, the obtained frequencies were not too high, reaching an average value of 1028 Hz. The shedding period, determined as $1/f_{shedd,}$ is therefore 9.73 e-4 s. This result was rather surprising; as much shorter shedding periods were anticipated - the original assumption on the cavitation shedding period was in order of 1e-8 s to 1e-6 s.

A doubt arose, that the shedding frequency might get in a resonance with the frequency of the 3-piston pump, potentially leading to a distortion of the results. The pump frequency was determined as 24.37 Hz and the pistons' frequency is therefore 73.11 Hz (three times higher as there are 3 pistons). Other multiples of frequencies were calculated, see Table 8. Nonetheless, it can be concluded, that resonance should not occur as the shedding frequencies are different from the pistons' and the pump's frequency.

Table 8: Multiple of frequencies of the pump pistons and the pump itself

Number of multiple	Pistons' frequency [Hz]	Pump frequency [Hz]
1	73.11	24.37
2	146.22	48.74
3	219.33	73.11
4	292.44	97.48
5	365.55	121.85
6	438.66	146.22
7	511.77	170.59
8	584.88	194.96
9	657.99	219.33

Number of multiple	Pistons' frequency [Hz]	Pump frequency [Hz]
10	731.1	243.7
11	804.21	268.07
12	877.32	292.44
13	950.43	316.81
14	1023.54	341.18
15	1096.65	365.55
16	1169.76	389.92
17	1242.87	414.29
18	1315.98	438.66

2.3.2 Results from the second of measurements

As mentioned above, the purpose of the second set of measurement was to observe the pit distribution over the sample and to determine the average dimensions of the individual pits, including an approximate number of them. The results will serve as a basis for comparison of CFD results with the experiment by means of the cavitation erosion model.

Two samples were tested, one was subjected to cavitation for 1 minute, the second one for 5 minutes. In Figure 42, surface topographies of the two samples are presented.

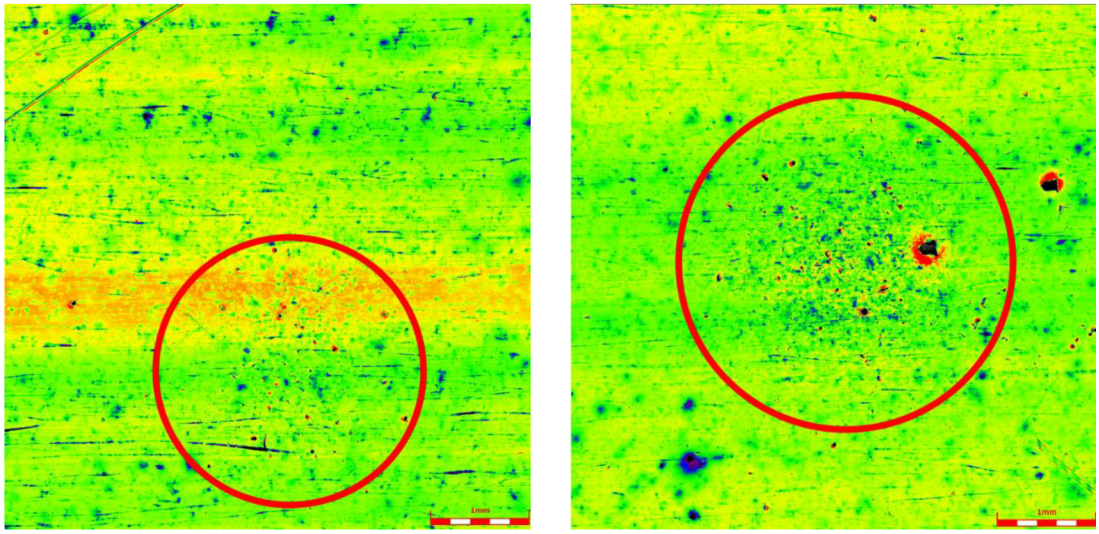

Figure 42: Surface topographies of the samples from the second set of measurements after 1 minute (left) and after 5 minutes (right), source: CEITEC

It can be seen that the pitted region of the sample, which was exposed to cavitation for only 1 minute, is not very distinct. Therefore, the second sample is going to be used for evaluation of the pit characteristic.

The approximate number of pits on the sample was computed to be 160, including even the smallest pits. The pit dimensions were determined from profilometry, which was performed in

the direction of x and y axis and also in the diagonal direction. Figure 43 presents a profilometry in the diagonal direction with highlighted pits.

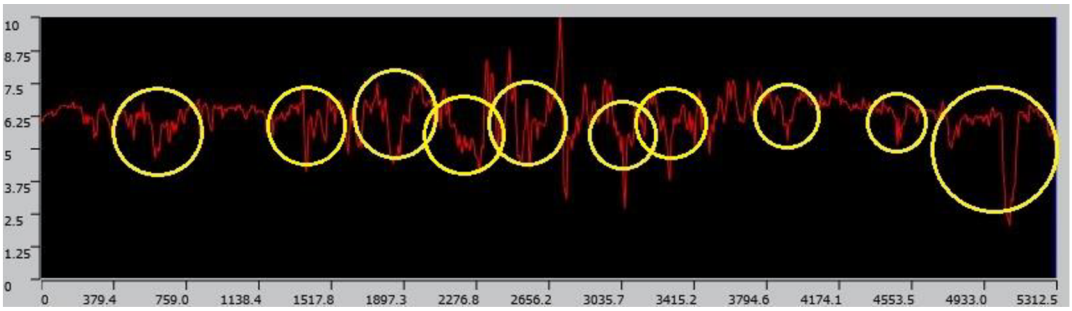

Figure 43: Profilometry of the pit region, source: CEITEC

For each pit, the corresponding radius and depth were assessed according to Figure 44, inspired by [41].

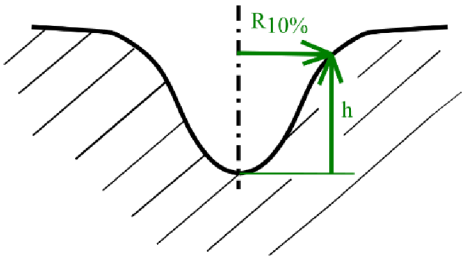

Figure 44: Pit dimensions, inspired by [41]

The average radius and the average depth were determined as 68 µm and 2.1 µm respectively, resulting in an average volume of the pit to be approximately $3.05 \cdot 10^{-14}$ m^3. Together with the approximate number of pits (160), the surface of the sample (0.0008078 m^2) and the duration of the test (300 s), it can be concluded that the volume damage rate V_d, defined as a ratio of deformed volume (relative to the sample surface) and the test duration, is $2.014 \cdot 10^{-11}$ m^3/(m^2·s). This value is going to be applied in the cavitation erosion prediction model.

2.3.3 Concluding remarks to the experimental part

The goal of this subchapter is to summarize the experimental part and to highlight the most important findings.

The first experimental set seemed to be successful in reaching all the cavitation erosion phases in a reasonable time, which was the main aim. Therefore, the copper sample showed as a good choice for this cavitating jet experiment. Another important concluding remark is the confirmation of the equation for the optimal stand-off distance, which ensured that the cavitation peening was the prevailing mechanism of the material erosion as a significant ring-shaped pit region occurred on the surface sample. And naturally, the measured data of the volume flow rate, pressure and temperate will serve as a basis for defining boundary conditions in the following CFD calculations.

Cavitation visualization performed by high-speed camera brought results concerning the shedding frequency of the cavitating liquid jet, which was determined to be 1028 Hz. This value is going to be compared to the numerical results provided by CFD.

Moreover, a set of very unique pictures of the eroded sample and even of the individual material particles was obtained in a cooperation with scientists from CEITEC, enabling us to better understand the cavitation erosion mechanisms. In addition, Brinell hardness of the sample was determined as 86.74 HBW. The gathered data should be a subject to a thorough material research focused on a studying of the eroded particles' shape and the sample surface itself.

The second set of measurement brought results concerning the volume damage rate, computed as $2.014 \cdot 10^{-11}$ m/s, which will serve as a basis in cavitation erosion prediction model for linking the experimental and computational results obtained from CFD simulation described in the following chapter.

3 Computational part

3.1 Introduction

The aim of this CFD modelling is to simulate a cavitating liquid jet experiment (inspired by ASTM G134 test) and compare experimental results with numerical ones. The comparison will be carried out by means of the appearance and behavior of the cavitation cloud and the results from the simulation will also serve as a basis for cavitation erosion prediction. Moreover, a comparison of different turbulence models and other settings will be provided too as a part of the chapter devoted to the optimization of numerical simulation of the cavitating jet.

3.2 Geometry and mesh

The fluid domain with its main dimensions is presented in Figure 45. The domain consists of a shaped nozzle, submerged below water level in a large tank, thus the problem can be solved as axisymmetric. Firstly, the dimension *s* (the stand-off distance) was determined as 20 mm to correspond to the experimental set-up described in the author's bachelor thesis [37]. However, in this diploma thesis, the new knowledge of cavitating liquid jet behavior was utilized and the minimal stand-off distance was calculated as 50 mm to ensure cavitation erosion. Therefore, two initial computations with and without temperature effects were carried out using the geometry with a 20 mm stand-off distance, and afterwards, in case of all other computations, the changed geometry with the longer stand-off distance was applied. Moreover, dimensions *h* and *b* were later extended (from 80 mm to 190 mm in case of the dimension *h* and from 95 mm to 190 mm in case of the dimension *b*) to reduce a potential risk of the cavitation being extinguished by a backward pressure wave reflecting from the pressure outlet boundary condition.

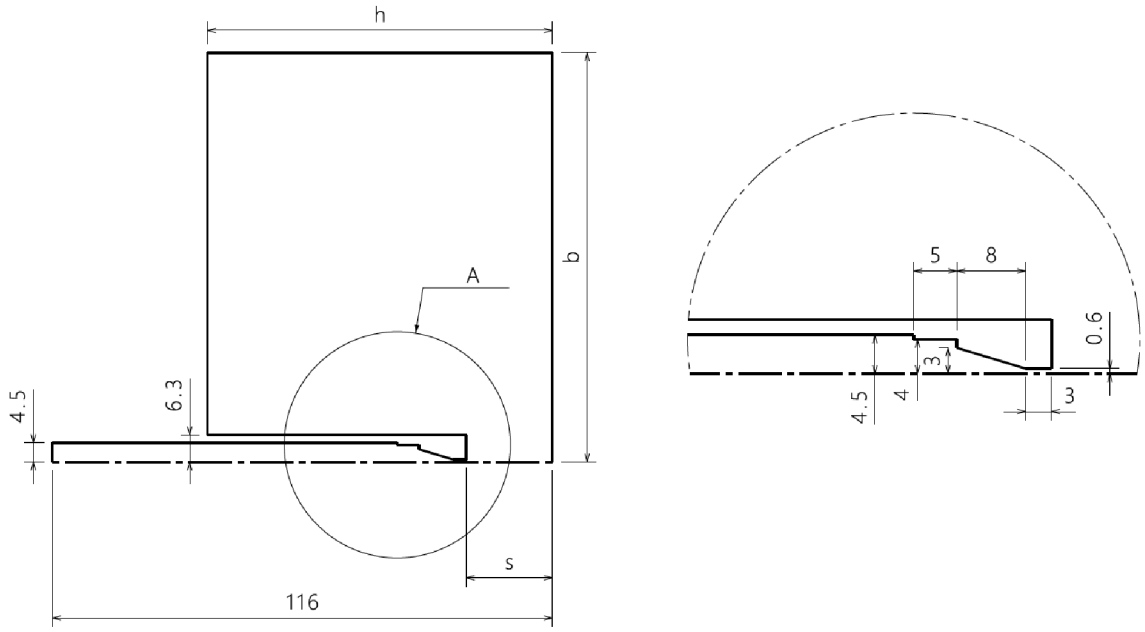

Figure 45: Computational domain

Three types of mesh were created – a coarse one (495 696 nodes, 493 800 cells), a middle-sized one (1 583 981 nodes, 1 580 300 cells) and a fine one (3 470 009 nodes, 3 464 220 cells), therefore various turbulence models could be employed. The coarse mesh was advantageously used for testing of new computational set-ups as the computational time was rather reasonable in comparison with the larger meshes. The coarse mesh with its details is displayed in Figure 46.

The presented configuration corresponds to the stand-off distance of 20 mm. As mentioned above, number of nodes is 495 696 and number of elements is 493 800, therefore it almost reaches the upper limit of 512 000 elements for student license of Ansys Fluent. The element order is linear (hence, without mid-side nodes), and all the elements are quadrilateral. In the nozzle throat, where cavitation is incepted, the mesh is refined to 30 elements across the cross-section with bias factor of 5. The whole mesh is conformal.

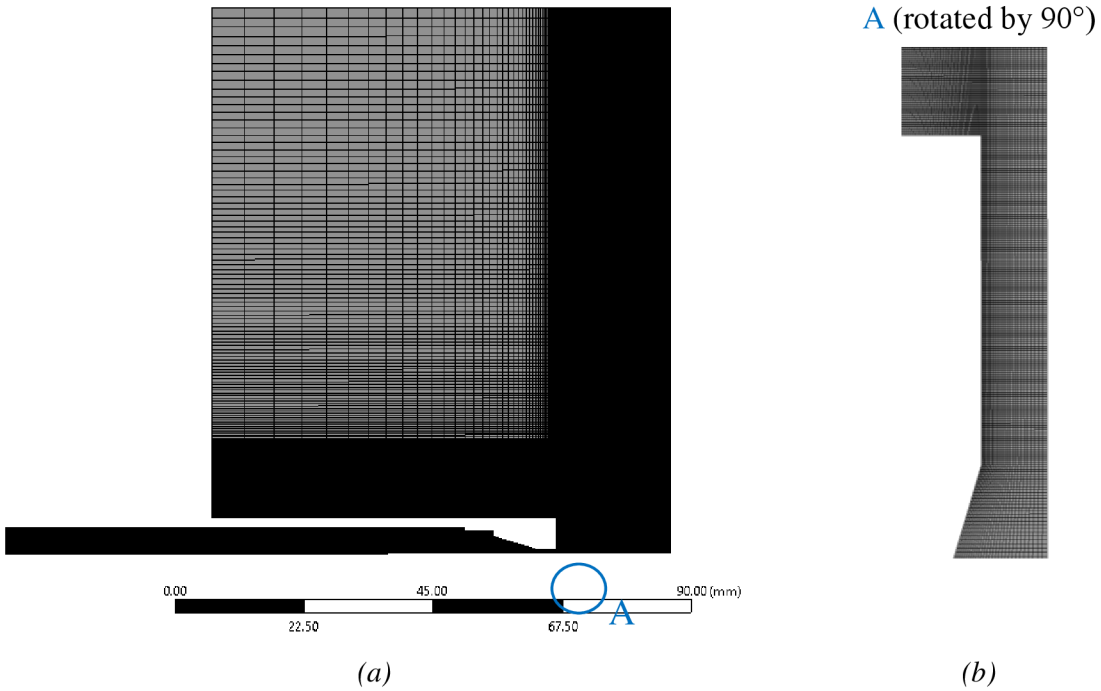

Figure 46: The coarse mesh (a) and its detail in the nozzle throat (b)

As mentioned earlier, the stand-off distance was later changed to 50 mm, and simultaneously, the outlet zone was prolonged, therefore the chance of the cavitation cloud being prematurely swallowed (before reaching the bottom wall) by the artificial pressure wave reflecting from the pressure outlet boundary condition was decreased. In the middle-sized mesh, number of nodes across the nozzle throat was still held at 30 with the bias factor of 5, however, the area between the nozzle throat and the bottom wall was meshed finer. And obviously, the larger domain at the outlet led to another increase of nodes in the mesh, which eventually consisted of 1 583 981 nodes. The middle-sized mesh is presented in Figure 47.

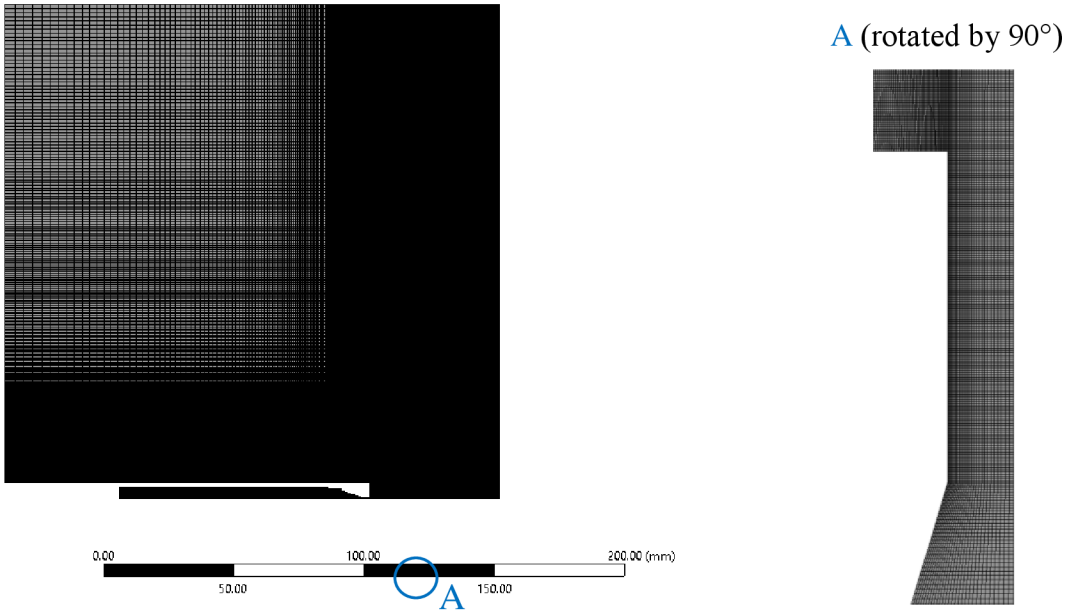

Figure 47: The prolonged domain and the middle mesh (a) and its detail (b)

The fine mesh contains altogether 3 470 009 nodes and is very significantly refined across the nozzle cross-section, see Figure 48. In contrast to the coarse and middle-sized mesh, which both have 30 elements across the cross-section, the fine mesh includes 90 nodes in this direction. The refinement was performed to enable the application of SST *k-ω* model.

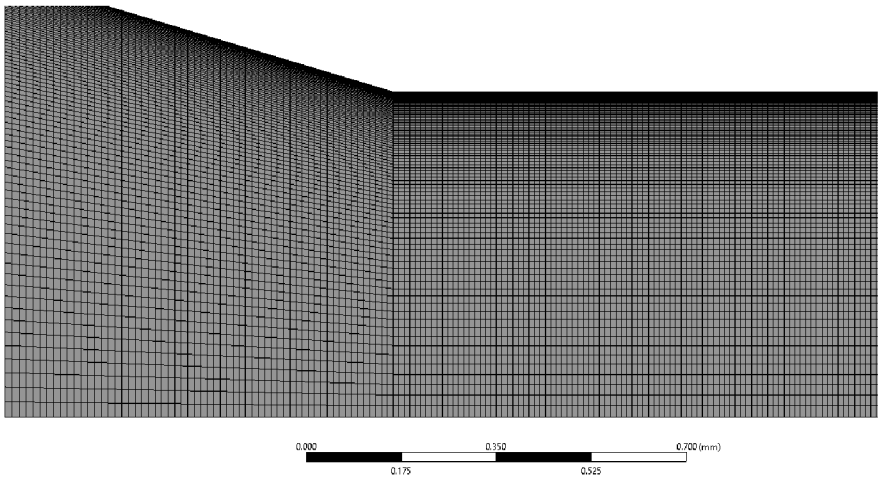

Figure 48: Detail of the fine mesh

3.3 Set-up

3.3.1 General settings

The problem was solved in a double-precision mode, which uses the double number of decimal numbers in the computation compared to a single-precision mode, leading to more accurate calculation. In case of multiphase problems, the double-precision mode is almost necessary for solving the difficult pressure fields correctly [35].

The cavitation problems are of a transient character, the presented geometry is 2D and axisymmetric, and pressure-based solver was chosen. Traditionally, pressure-based solver was used for incompressible (or mildly compressible) flows of low speeds, however, nowadays even compressible flows can be simulated with this solver. On the other hand, density-based solvers are usually slightly better at solving highly compressible flows, including shock waves [35].

3.3.2 Turbulence modelling

As mentioned above, various turbulence models were compared in terms of their ability to capture vortices emerging during cavitation inception and collapse.

The coarse and middle-sized meshes have higher values of the wall y^+ criterion[2], therefore k-ε realizable model with non-equilibrium wall functions was applied. This model does not require too high resolutions in near-wall regions and the criterion y^+ could lie in an interval of 20-120. Realizable model is less dissipative and has a reasonable convergence in comparison to standard k-ε and RNG k-ε. The wall functions solve the near-wall regions. Quantity k is the kinetic turbulence energy and ε is the turbulent dissipation rate.

The fine mesh was created in the way to satisfy the criterion wall y^+ approximately equal to 1 (however, the interval of 1 to 5 is viewed as sufficient), that means very high spatial resolutions of the mesh in the near-wall regions. Therefore, the shear-stress transport (SST) k-ω model could be applied in this problem. This model conveniently combines the robust and accurate standard k-ω model in the near-wall region and in the free-stream, it uses k-ε model. This connection of the models makes the SST k-ω model applicable to a wider variety of flow states (e.g. adverse pressure gradient flows and transonic shock waves) than the standard k-ω model and k-ε model separately.

All the described models belong to models based on RANS (Reynolds-averaged Navier-Stokes) equations and they are two equations eddy viscosity models, which means that they assume isotropic turbulent viscosity [35].

One type of the computations was performed using the RNG turbulence model with a modification of turbulent viscosity via User Defined Function (UDF). The UDF was

[2] Criterion wall y^+ describes the velocity gradients in near-wall regions. An accurate representation of the near wall region determines a successful prediction of wall bounded turbulent flows. Each turbulence model uses appropriate wall functions, therefore different values of y^+ and spatial resolutions of the near wall area are required. Quantity y^+ is a dimensionless wall distance, denoted by:

$$y^+ = \frac{y \cdot u_\tau}{\nu},$$

where u_τ is friction velocity, y is absolute normal distance from the wall and ν is kinematic viscosity. Criterion y^+ can be interpreted as a local turbulence Reynolds number, which means that its magnitude determines the relative importance of turbulent processes [40].

constructed according to the paper [38]. The authors found out that standard *k-ε* RNG model and *k-ω* model without compressibility effects were not able to fully capture the pulsating and unstable behavior of the cavitating flow. Therefore, the *k-ε* RNG model was modified and in case of *k-ω* model the compressibility effects (considering barotropic fluid) were implemented in the calculation. Comparison of the numerical and experimental results led to a conclusion that compressibility effects are significantly important when modelling cavitating flow. In the standard *k-ε* RNG model, the effective viscosity is composed of laminar turbulent viscosity μ_l and turbulent viscosity μ_t, which can be expressed by the following equation (so called Prandtl-Kolmogorov equation) [38]:

$$\mu_t = \rho \cdot C_\mu \cdot \frac{k^2}{\varepsilon}, \tag{23}$$

where C_μ is a constant equaled to 0.09. It can be seen, that the density in the equation is considered to be constant and no corrections are provided for two phase mixtures. The modification of the standard *k-ε* RNG model therefore implements a function for the calculation of the mixture density leading to a reduction of the turbulent viscosity, especially in the areas with low void ratio[3]. Density in the Prandtl-Kolmogorov equation is therefore substituted by a function for density [38]:

$$f(\rho) = \rho_v + \left(\frac{\rho_v - \rho}{\rho_v - \rho_l} \right)^n \cdot (\rho_l - \rho_v) \qquad n \gg 1 \tag{24}$$

In Figure 49, a comparison of modified and standard function *f(ρ)* for *n* = 10 is displayed. It is clearly visible that in regions with lower densities the function *f(ρ)* is shifted downwards, thus reducing a turbulent viscosity significantly.

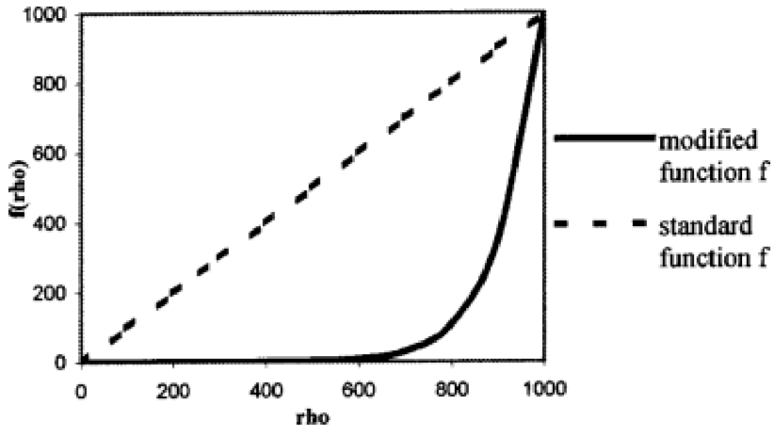

Figure 49: A comparison of standard and modified function f(ρ)

[3] Void ratio (respectively void fraction) α determines the ratio of vapor and liquid phases in a particular part of the domain. It is calculated as follows: $\alpha = (\rho - \rho_l)/(\rho_v - \rho_l)$. Therefore, α = 0 means that the area is completely filled with liquid, and α = 1 stands for a fully vapor area [38].

As mentioned above, the described modification led to a reduction of the turbulent viscosity and consequently, the oscillation of the cavitating flow and its shedding frequency were captured more precisely and corresponded well to the experimental results [38].

Similar modification can be carried out also for the Prandtl-Kolmogorov equation in the SST *k-ω* turbulence model [39].

The described modification of the RNG turbulence model was used in the cavitation simulation in this diploma thesis and UDF for reduction of the turbulent viscosity was created, see Figure 50.

```
/** UDF to modify the Turbulence Viscosity in two-phase flow with cavitation model
(Coutier-Delgosha, Regiane Fortes-Patella (JFE, 2003) **/
#include "udf.h"
#include "mem.h"
DEFINE_TURBULENT_VISCOSITY(cavitation_mu_t, c, t)
{
 int n = 10;
 real M_keCmu = 0.09;
 Thread** pt = THREAD_SUB_THREADS(t);
 real rhoM = C_R(c, t);
 real rhoL = C_R(c, pt[P_PHASE]);
 real rhoV = C_R(c, pt[S_PHASE]);
 real f_of_rho = rhoV + pow((rhoM - rhoV)/(rhoL - rhoV), n)*(rhoL - rhoV);
 return M_keCmu*f_of_rho*SQR(C_K(c,t))/C_D(c,t);
}
```

Figure 50: UDF for reduction of the turbulent viscosity

3.3.3 Cavitation modelling

The multiphase problem in this diploma thesis was simulated using the mixture model. However, one computation with VOF (Volume of Fluid) set-up was performed on the middle-sized mesh, as it is known, that VOF models might lead to a better distinction of the phases interface. The chosen formulation of volume fraction parameters was set to explicit, which can be only used in transient simulations and provides better accuracy than the implicit formulation. The implicit formulation is, unlike the explicit formulation, iterative and is suitable for both steady and transient solvers. Due to its iterative character, the computational time is significantly shorter, however, it is redeemed by worsened accuracy of the solution.

In case of the mixture model, two Eulerian phases (water-liquid and water-vapor) were set, slip velocity as a mixture parameter was not taken into consideration and dispersed interface modeling was selected. In case of the VOF model, the third Eulerian phase was added (air at the outlet boundary).

Concerning the particular cavitation model, the Schnerr-Sauer cavitation model with the following settings was applied in the numerical simulation: bubble number density left at its default value of 10^{11} and vaporization pressure was changed to a value of 1580 Pa, which was determined from the experiment. Another cavitation model is Zwart-Gerbert-Belamri, which needs a specification of the bubble diameter, the nucleation site, volume fraction, the evaporation coefficient, and the condensation coefficient. Both described models work well,

and they are compatible with all of the turbulence models, which are available in Fluent [35]. There is also another cavitation model created by Singhal et al. (also called Full Cavitation Model), whose advantage is an applicability to non-condensable gases. However, this model is not compatible with the Eulerian multiphase model [35].

3.3.4 Boundary conditions and named selections

As mentioned above, the boundary conditions were determined from the experiment to enable a full comparison of numerical and experimental results. The average value of the flow through the nozzle was calculated as 12.16 l/min, which corresponds to a value of velocity at the inlet of 3.185 m/s as the inlet section has a diameter of 9 mm. The water temperature was averaging around 14 °C, therefore, the water vapor pressure was determined as 1580 Pa. At the outlet, there is atmospheric pressure, thus zero-gauge pressure was set. In Figure 51, named selections are presented.

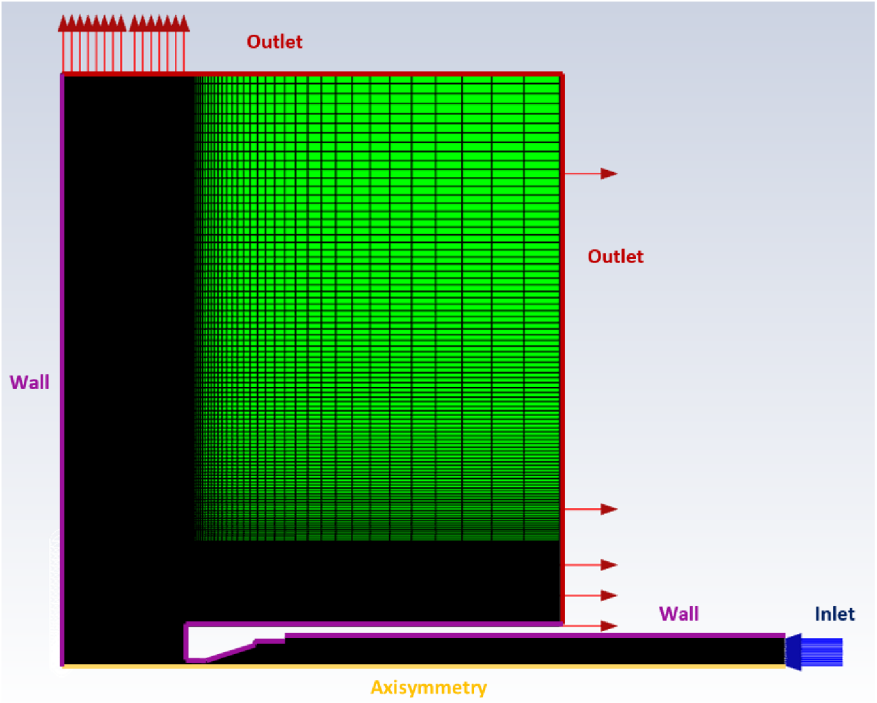

Figure 51: Named selections

3.3.5 Energy equation and non-reflecting boundary condition

To be more in line with the reality, energy equation was employed in one of the computations. The simulation was performed on the coarse mesh, with k-ε realizable model of turbulence and multiphase mixture model. Energy equation takes into consideration temperature and enthalpy changes, which can affect all the temperature dependent quantities, as e.g., water vapor pressure and density. In this computation, even the non-reflecting boundary condition was utilized to minimize effects, such as premature termination of the cavitation process, caused by the backward pressure wave reflecting from the pressure outlet boundary condition. Density of water-vapor was calculated according to the equation of ideal gas, unlike all the other computations, which assumed the density to be constant. Firstly, density of water-liquid was

left as constant in order not to further increase the complexity of the calculation. However, the problem diverged, therefore the water-liquid was switched to compressible. Unfortunately, the non-reflecting boundary condition decreases robustness of the computation, therefore relaxation factors had to be decreased significantly to ensure convergence of the problem, leading to a significant prolongation of computational time. Chapter 3.4.2 will be devoted to this type of computation.

3.3.6 Solution methods and activities

Concerning the solution methods, the following schemes and spatial discretization were selected: SIMPLE pressure-velocity coupling, PRESTO! discretization for pressure and First Order Upwind discretization for momentum, volume fraction, turbulent kinetic energy and turbulent dissipation rate. Under-relaxation factors were altered subsequently: 0.5 for density and 0.05 for vaporization mass. In case of the computation with the SST k-ω turbulence model and in case of the computation with the energy equation and non-reflecting boundary condition, the relaxation factors were at the beginning of the simulation decreased even further (all quantities to 0.1 with exception of the vaporization mass, which remains to be set at 0.05). Nonetheless, after a few thousands of iterations, they were all (except for the density and the vaporization mass) set to default again.

Volume fraction of the phases and static pressure were monitored, and their contours were recorded, therefore, animations could be created. Phase interaction was analyzed, too.

The set-up of the transient solver included 20 iterations per time-step. One part of the computations used a fixed time-step size of $1 \cdot 10^{-8}$ s and the other part was set to adaptive time-stepping with minimum time-step size $1 \cdot 10^{-8}$ s, maximum time-step size $1 \cdot 10^{-5}$ s and global Courant number set to 2, therefore a faster convergence of the problem could be obtained.

3.3.7 Complete overview of individual computations

Table 9 puts together all the different set-ups for individual simulations. The goal is to optimize the computation, hence, the most realistic results could be used as a basis for cavitation erosion prediction.

Table 9: Overview of the computation variants

Computation number	Type of the mesh	Energy equation	Non-reflecting boundary condition	Multiphase model	Turbulence model
1	Coarse	No	No	Mixture	k-ε Realizable
2	Coarse	Yes	Yes	Mixture	k-ε Realizable
3	Middle-sized	No	No	Mixture	k-ε Realizable
4	Middle-sized	No	No	VOF	k-ε Realizable
5	Fine	No	No	Mixture	SST k-ω
6	Coarse	No	No	Mixture	k-ε RNG with UDF (Eq. 24)
7	Middle-sized	No	No	Mixture	k-ε RNG with UDF (Eq. 24)

Notes on the computations:

- Computations no. 1 and no. 2 were performed on the geometry with the stand-off distance of 20 mm.
- Cavitation model was in all cases set to Schnerr-Sauer, see Chapter 3.3.3.
- Both k-ε models included non-equilibrium wall functions for near-wall treatment.

3.4 Optimization of numerical simulation

This chapter is devoted to the optimization of the numerical simulation of the cavitating liquid jet as it is quite difficult problem due to its dynamic and unstable behavior. Various computations with different settings according to Table 9 were performed and assessed rigorously, hence, the most realistic simulation could be used for prediction of cavitation erosion.

3.4.1 Computation no. 1

At first, it is very important to stress out that even the computation performed on the coarse mesh was tremendously time-consuming. The computation ran on a remote desktop with 2x4 processors and 40 GB RAM for more than 3 months almost without a break-in (apart from a few days, corresponding to restarts needed for software upgrades, which led to quite an abrupt termination of the calculation). The computation probably took so much time because of the very low time-step ($1 \cdot 10^{-8}$ s), which was however inevitable due to very fast and unstable behavior of the cavitating flow. The calculation can be considered to run properly as the residuals were relatively low (of order $1 \cdot 10^{-5}$ and lower). The final number of iterations was around 4 588 000 and as none-convergence criterion was chosen and 20 number of iteration per-time step were selected, it can be concluded that the computation included altogether 229 400 time-steps, resulting in $2.294 \cdot 10^{-3}$ s of duration of the whole phenomenon taking into consideration the fixed time-step of $1 \cdot 10^{-8}$ s. This means that the investigated cavitation process including cavitation inception, its growth and finally, a collapse, was very abrupt and fast. However, the results from the experiment suggested that the shedding period was around $9.73 \cdot 10^{-4}$ s, therefore 2.4 times shorter than according to the numerical simulation.

As mentioned above, during the computation, one could observe the inception of cavitation, its growth and its following collapse. Following set of pictures displays contours of volume fraction of phases; the legend is presented on the right - red color stands for volume fraction of value 1 (all water) and blue color shows volume fraction of value 0 (all vapor). Black color in the pictures is caused by slight issues with displaying and the affected regions should be considered as all-water.

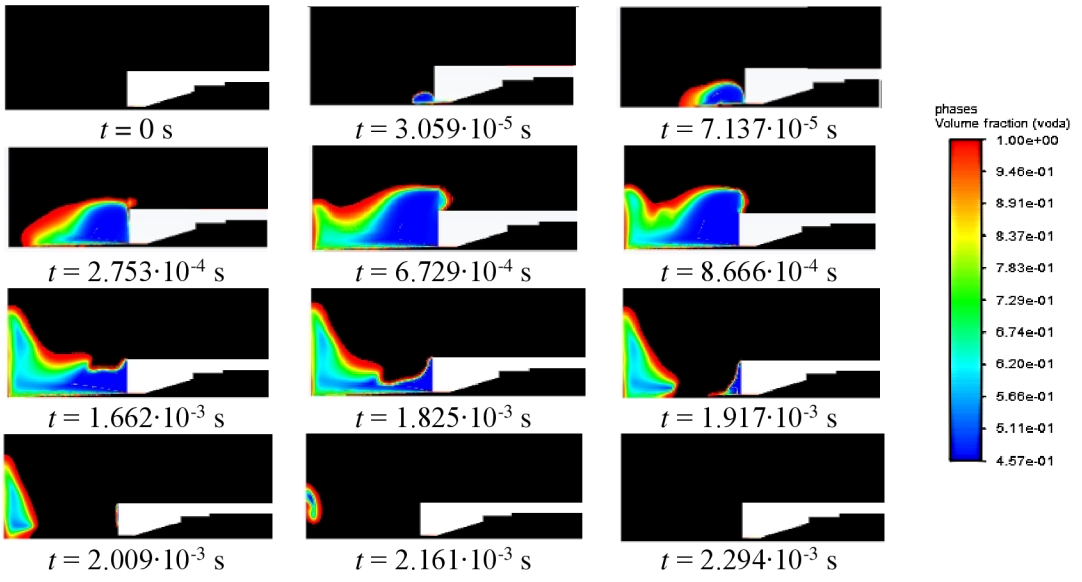

Figure 52: Inception, growth and decay of the cavitation – computation no. 1

Static pressure was monitored on the impact surface and the obtained data was exported as an ASCII file. Consequently, the data were processed in a script in Python and maximal value of impact pressure $1.4 \cdot 10^7$ Pa was found, corresponding to the moment when the cavitation cloud stopped growing and started to reduce its size.

3.4.2 Computation no. 2

The computation no. 2 included the temperature effect to simulate the cavitating flow more realistically. Moreover, a non-reflecting boundary condition was applied at the pressure outlet to minimize the chance of the pressure wave reflection from the pressure outlet leading to an extinguishment of the cavitating jet. As mentioned above, density of water-vapor was determined using the ideal gas equation and density of water-liquid was at first left as constant, but then changed to compressible because of the simulation divergence. According to the Fluent's User Guide [35], the non-reflecting boundary condition decreases robustness of the simulation, therefore relaxation factors had to be decreased to make it possible to start the simulation at all. The whole simulation was very unstable and diverged a few times, even when the relaxation factors and time-step were decreased significantly. After 2 242 000 iterations with the fixed time-step size of $1 \cdot 10^{-9}$ s, the problem diverged again, and it was not possible to renew the simulation again in any way – further decrease of the time-step and relaxation factors did not help. Figure 53 displays the contour of volume fraction at the 2 233 820th iteration.

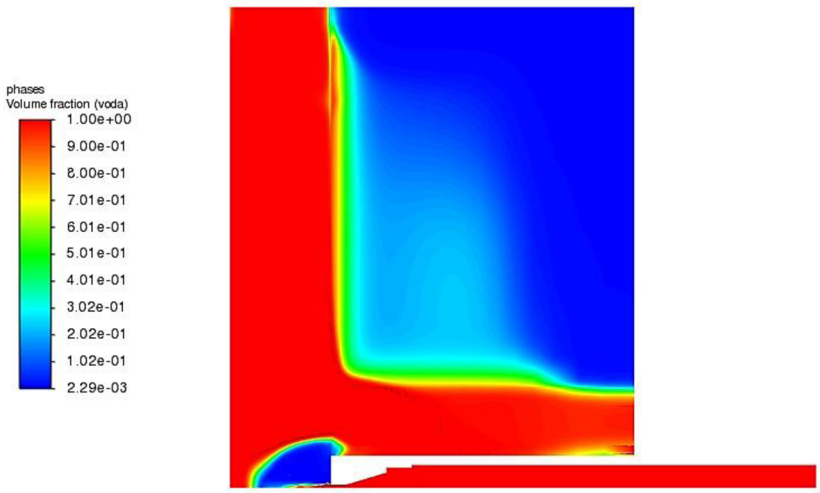

Figure 53: Volume fraction contour – computation no. 2

In Figure 53, a very significant influence of the mesh can be observed. In the regions, where the cells grow in their size, the contour of volume fraction suggest a locality with water-vapor, however, that is not physically acceptable. There is a very distinct border corresponding to the area with growing size of cells. Obviously, the mesh should be either refined in these areas, or the simulations should have proceeded on at least the middle-sized mesh. However, even the computation performed on the coarse mesh lasted over 1 month (to reach the described diverged state), and obviously, in case of larger meshes, the computational time would increase even more. Such long simulations could be accepted in a long-term scientific research, however, they are not feasible within the scope of diploma theses.

3.4.3 Computation no. 3

Computation no. 3 was performed on the middle-sized mesh and with *k-ε* realizable turbulence model. Adaptive time stepping with minimum time-step size of $1 \cdot 10^{-8}$ s and maximum of $1 \cdot 10^{-5}$ s was set to ensure a faster proceeding of the simulation. Nonetheless, even in spite of this setting and running the computation on the university's cluster with 26 processors, the computation lasted for over one month. Therefore, it is evident, that this simulation is not very suitable for testing new types of settings as the expected change in results would require a lot of computational time.

In the following set of images, results from the numerical simulation are presented. Obviously, the cavitation did not reach the bottom wall, which unfortunately does not correspond to the experiment. This was probably caused by too high turbulent viscosity and computation no. 6 will investigate this issue more profoundly. However, the shape of the cavitation cloud seems to be quite realistic and the whole phenomenon of cavitation inceptions, its growth and following collapse lasted for approximately $3.427 \cdot 10^{-3}$ s, therefore, it can be concluded that in case of a larger stand-off distance, the phenomenon duration increases. For comparison, in the computation no. 1 with the stand-off distance of 20 mm, the cavitation process lasted for approximately $2.294 \cdot 10^{-3}$ s.

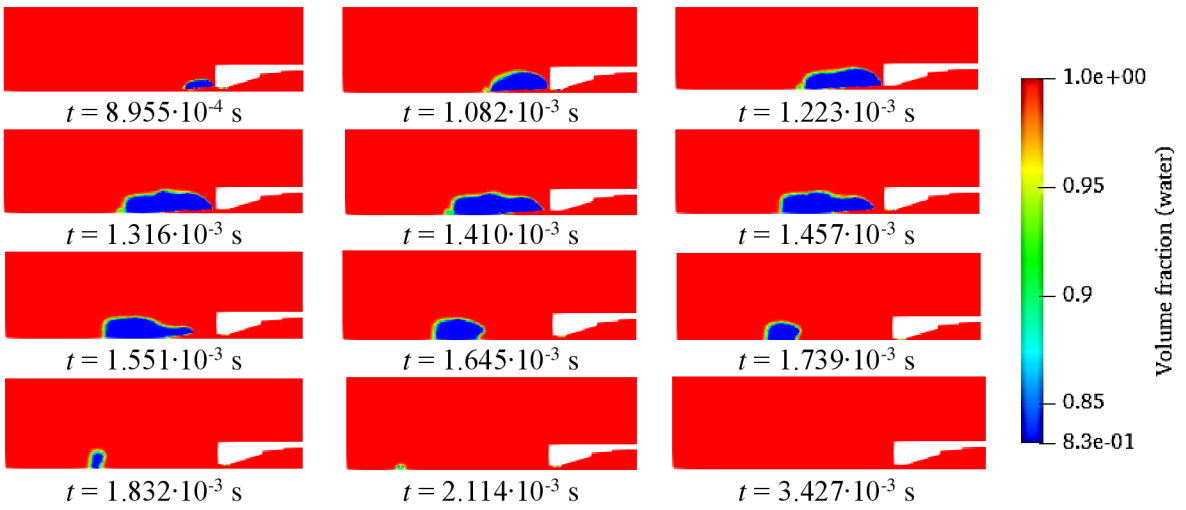

Figure 54: Set of pictures of volume fraction (water) – computation no. 3

3.4.4 Computation no. 4

In case of the calculation with the multiphase model Volume of Fluid (VOF), better distinction between phases was anticipated. Again, *k-ε* realizable model was used and temperature changes were not taken into consideration as the computation no. 2 diverged after implementing the energy equation in the simulation. The simulation ran on the middle-sized mesh and the time-step was once again set to a fixed value of $1 \cdot 10^{-8}$ s. The simulation proceeded quite steadily, however, the distinction between the phases was approximately at the same level as in case of mixture model, therefore, the VOF model was abandoned in the other computations as the simulations with mixture model proceeded more quickly.

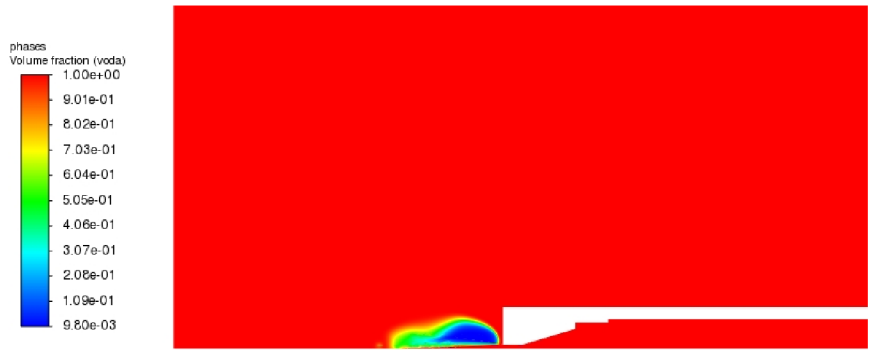

Figure 55: Cavitation inception – VOF model, $t = 1.173 \cdot 10^{-3}$ s

3.4.5 Computation no. 5

Computation no. 5 was performed on the fine mesh with 3 470 009 nodes and SST k-ω model, which advantageously combines standard k-ω model in the near-wall region and k-ε model in the free-stream, therefore it enables to capture emerging vortices in a better detail than k-ε models. Time-step size was at first set-up to a value of $1 \cdot 10^{-8}$ s, however, the calculation diverged altogether two times due to Courant number exceeding a limiting value of 250. Subsequently, the time-step was reduced to $1 \cdot 10^{-9}$ s after the first divergence and to $1 \cdot 10^{-10}$ s after the second one. The computational time was indeed very long due to a combination of a quite large mesh and very low time step, even in spite of running the simulation on the university's cluster using altogether 26 processors.

However, the details of cavitation cloud obtained from the simulation are very fine and enable us to better understand the unstable behavior of the cavitating liquid jet.

The blue color in the following set of figures stands for the vapor phase and the red one illustrates the liquid – the scale presented in the first row of pictures is the same for all the other pictures.

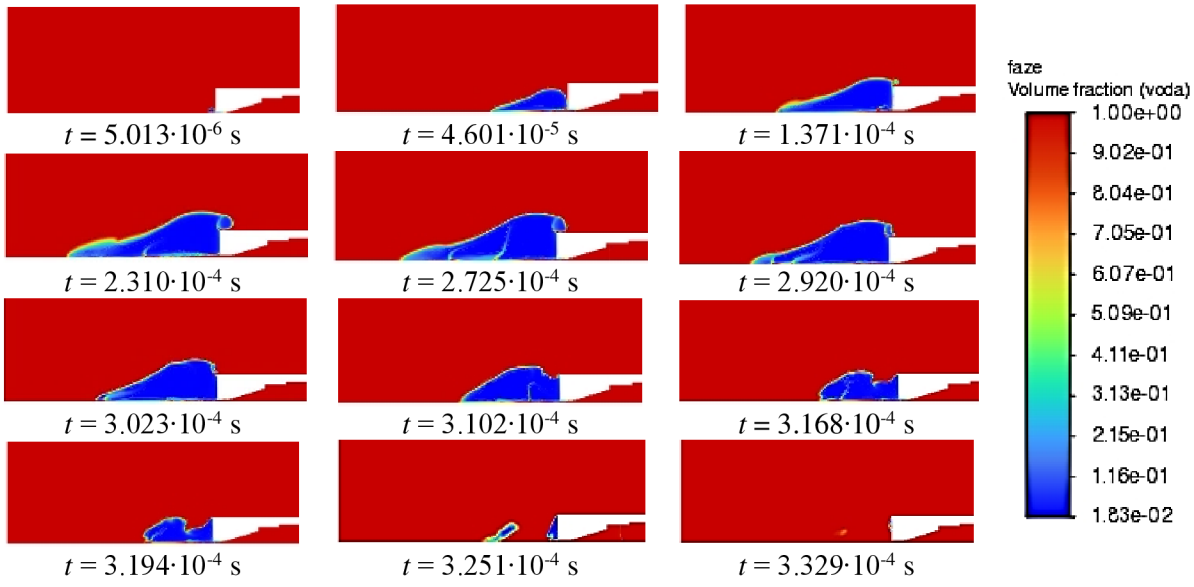

Figure 56: Set of images of volume fraction (water) – computation no. 5

The phenomenon duration from inception to collapse was approximately $3.423 \cdot 10^{-4}$ s, hence very similar to the results from computation no. 3. Furthermore, it can be seen from the previous set of pictures that the cavitation cloud grew significantly, but, unfortunately, has never reached the bottom wall. It might be due to the fact of too high turbulent viscosity. Therefore, the computation no. 6 included UDF for a reduction of this quantity.

Nonetheless, as mentioned above, the simulation performed with SST k-ω model brought about very nice details of the cavitation cloud, see Figure 57.

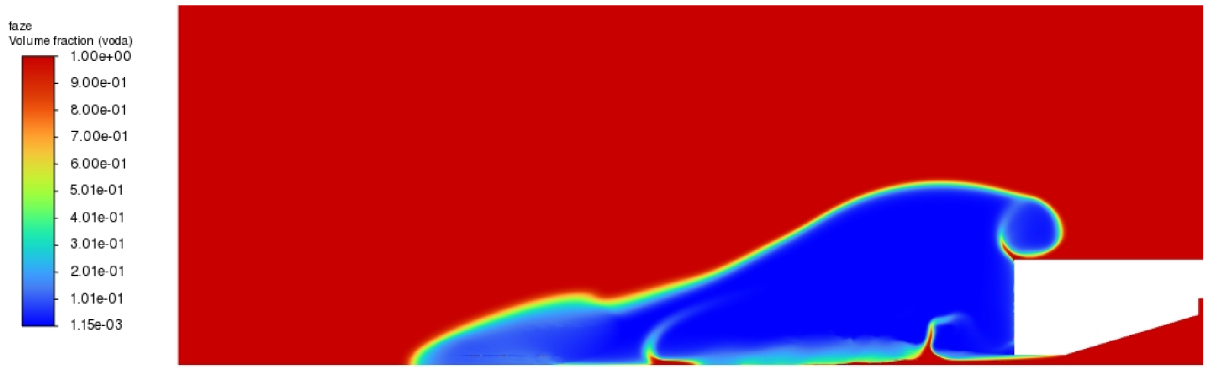

Figure 57: Detail of the cavitation cloud at time $t = 2.582 \cdot 10^{-4}$ s

An interesting phenomenon occurred at the cavitation cloud axis – a liquid jet is flowing through the vapor cloud and it can be seen that the jet is not completely coherent but rather disheveled. It might correspond to borders between 1st, 2nd and 3rd jet core flowing through the partial cavitation clouds, forming an extremely unstable and complicated structure, as described in Chapter 1.3.

3.4.6 Computation no. 6

As mentioned above, a doubt arose that the turbulent viscosity might be too high leading to an excessive damping of the growing cavitation cloud. Consequently, the cavitating flow in the simulation does not reach the bottom wall, in spite of impacting it clearly in the experiment. Therefore, the UDF for the modification of the turbulent viscosity was created according to Chapter 3.3.2 and was implemented to the RNG k-ε turbulence model. The simulation was performed on the coarse mesh, however a few modifications were implemented – a prolongation of the stand-off distance to 50 mm and no extension of pressure outlet boundary condition, therefore a number of nodes remained the same (495 696). Adaptive time stepping with minimum time-step size of $1 \cdot 10^{-8}$ s and maximum of $1 \cdot 10^{-5}$ s was selected to obtain quick but still reliable results. The average time-step size was determined by Fluent to be between $1.59 \cdot 10^{-7}$ s and $1.6 \cdot 10^{-7}$ s. This automatic determination is performed by estimating the truncation error, which is strongly linked to the time integration scheme [35]. The whole phenomenon from inception to collapse and disappearance of the cavitation cloud lasted for

$2.532 \cdot 10^{-3}$ s, thus still longer than in comparison with the experiment. Following set of pictures presents obtained contours of volume fraction.

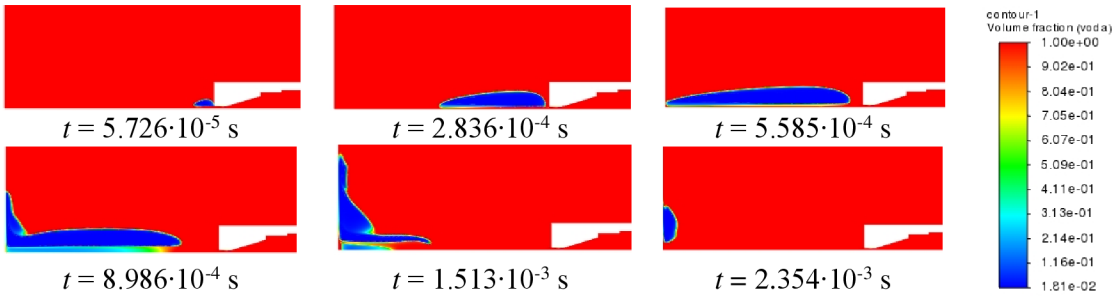

Figure 58: Set of images of volume fraction (water) – computation no. 6

It is obvious from the presented pictures that cavitation in this simulation reached the bottom wall. However, it was redeemed by the less accurate shape of the cavitating cloud - no such details as in case of the simulation with the SST k-ω model could be observed, moreover the shape seems to be rather simplified even in the comparison with the results from k-ε realizable model, presented in Chapter 3.4.3. Therefore, the next step is quite natural – computation no. 6 is going to be performed on the middle-sized mesh.

3.4.7 Computation no. 7

The setting of the computation no. 7 remained the same as in case of computation no. 6, however, as the simulation was performed on more detailed mesh, the acquired results were more precise. It is important to mention that unlike the previous computations; this was the first time when the cavitation cloud was periodically reappearing during the simulation. In all the previous computations, the cavitation cloud appeared only once. Obviously, the turbulent viscosity was too high, leading to a significant damping of the pulsating behavior of the cavitation, meaning the inception, growth and collapse occurred only once and lasted for a rather long time (the duration of the phenomenon was in order of 10^{-3} s) as the cavitation bubble dynamics was damped. In case of computation no. 6 with the already reduced turbulent viscosity, a second smaller cavitation cloud emerged, however, subsequently, no other cavitation cloud was incepted. Apparently, this was not caused by too high turbulent viscosity, but because of too large cells in the computational grid, unable to capture the cavitation bubbles of a smaller size, which are characteristic for the developed and stable cavitation cloud. In contrast, the first cavitation cloud in the simulation seemed to be quite smooth having a strange and unrealistic shape, which was probably caused by the insufficient accuracy and too high residuals at the beginning of the simulation. In computation no. 7, the first cloud had the unrealistic smooth shape too, however, then it reappeared in a much more realistic and structured way, moreover, the duration of the phenomenon was much shorter, see the following set of pictures depicting one shedding cycle of the cavitating jet after numerical stabilization of the simulation.

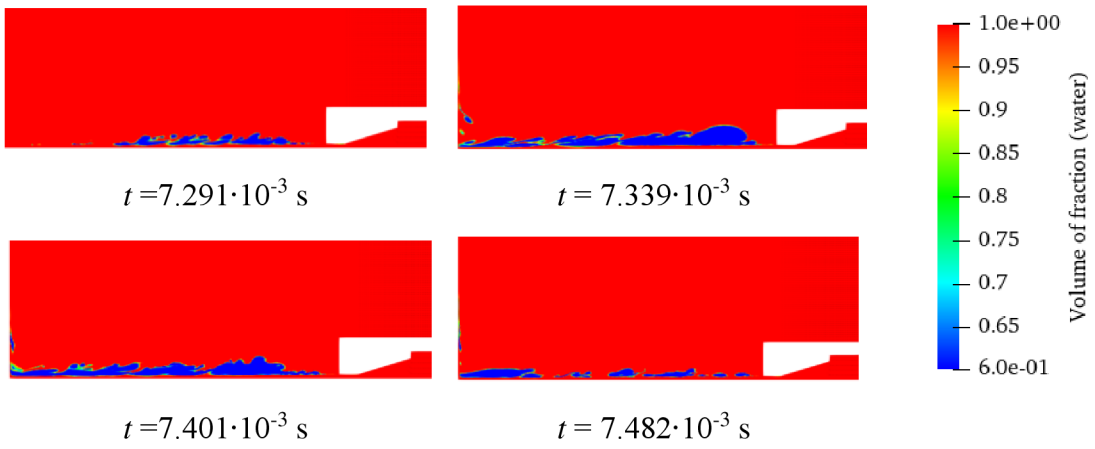

Figure 59: Computation no. 7 - set of images of volume fraction (water) during one shedding period after a considerable number of shedding cycles (after numerical stabilization of the simulation)

To conclude, the results seemed to be quite realistic and the computation proceeded relatively steadily, therefore, it was decided to use this simulation as a basis for the cavitation erosion prediction models described in Chapter 1.5., which is one of the main goals of this thesis.

3.5 Cavitation erosion prediction

As mentioned above, computation no. 7 has provided rather realistic representation of the cavitating liquid jet experiment, and therefore, it will serve as a basis for the cavitation erosion prediction. Clearly, even better results could have been obtained by implementing UDF for reduction of the turbulent viscosity into the SST *k-ω* turbulence model, which brought very nice details of the cavitating jet in computation no. 5. Nonetheless, the computation no. 5 lasted for over 3 months because of the combination of a quite large mesh and very low time step, even though it ran on the university's cluster using altogether 26 processors. As mentioned above, such long simulations are not feasible within the scope of diploma thesis. However, applying the UDF into SST *k-ω* turbulence model should definitely be a goal of a long-term scientific research, as it might bring even more accurate and realistic results.

3.5.1 Modified energy cascade model

To predict cavitation erosion, the energy cascade model was chosen, as this model has a strong physical background and multiple scientific teams apply this model in their research of cavitation erosion [17], [20], [21]. The energy cascade model is based on the evaluation of the potential energy of the vapor structure and includes two main equations, which were derived in Chapter 1.5, and are repeated here - the first one is the equation for potential power density (Eq. 25) and the second one presents an instantaneous power at the time t and location j (Eq. 26) [17]:

$$P_{den} = (p_d - p_v) \cdot \max\left(\dot{m} \frac{\rho}{\rho_v \cdot \rho_l}, 0 \right) \tag{25}$$

$$P_{imp}(j,t)\big|_i = P_{den}(i,t)\cdot\frac{1}{2\pi\cdot|\vec{R}|}\cdot\frac{\vec{R}\cdot\vec{n}}{|\vec{R}|} \tag{26}$$

The energy cascade model, described in this way, assumes a radial propagation of potential power density through the domain from point source at location *i* to a solid surface at position *j*. As this hypothesis is indisputably correct in terms of the physical concept, it has been shown by other authors [41], that some modifications, based on empirical results, can be performed to make the model more easily applicable.

The main idea behind the modification lies in a simplification of the effective distance, at which the cavitation is supposed to be still aggressive enough to cause severe damage to the sample. This distance was assigned as h_{agr} and its value was determined to be 10% of the thickness of emerging cavitating structure according to Kato et al. [42]. Consequently, the intensity of the collapsing cavitation structure can be expressed as follows:

$$P_{agr} = \frac{P_{pot}^{mat}}{\Delta S} = \int_{h_{agr}} P_{den}\, dh \tag{27}$$

and subsequently, this instantaneous cavitation aggressiveness should be integrated over time. Obviously, this approach, which only takes into consideration 10% of the thickness of the cavitating structure, is rather simplified in comparison to the approach described in Eq. 26. However, the authors [41] concluded, that even with this simplification, a good mutual correspondence between numerical and experimental results was obtained. In that paper, it was also stated that enlarging the effective distance over 10% of the cavitation sheet thickness led to an exaggeration of the potential of cavitation erosion as the cavitating clouds collapsing far away from the bottom wall are not so erosive. It is also important to mention, that the authors used the same turbulence model (RNG) and the same UDF for the modification of the turbulent viscosity as in case of computation no. 7. The proposed model with the modification of the effective distance to a distance h_{agr} is displayed in Figure 60.

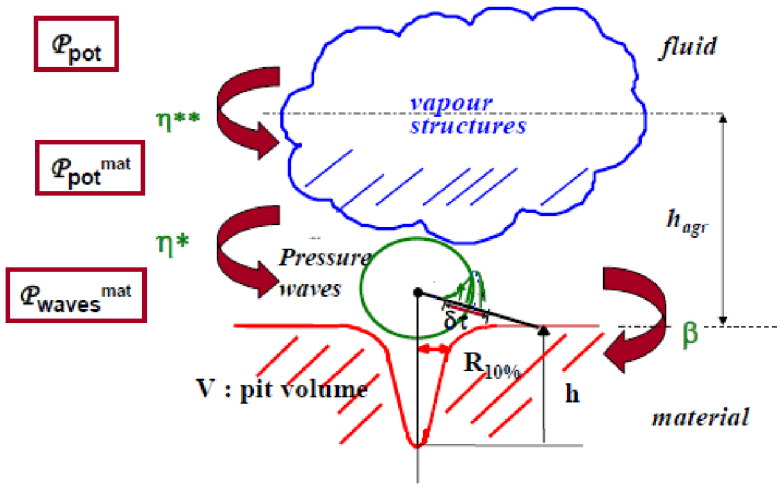

Figure 60: Simplified physical model of potential power density of imploding vapor structures [41]

Imploding cavitation structures emit potential energy P_{pot}, which is reduced by efficiency η^{**} to a value of P_{pot}^{mat} assigned as the intensity of cavitation aggressiveness. The efficiency η^{**} is strongly linked to the distance h_{agr} and depends mainly on flow conditions, type of the cavitating

structure and its dynamic behavior, and last but not least, on the distance from the imploding cavity to the nearby solid surface [41]. Afterwards, the potential energy of pressure waves, which finally reach the material (labeled as P_{waves}^{mat}), can be determined by multiplying the P_{pot}^{mat} by efficiency η^*, which essentially describes the ratio of energy of the emitted pressure waves and the initial energy of the cavity [43], [44]. The value of efficiency of the collapse η^* depends on the ratio of initial gas pressure p_{g0} in the bubble and local liquid pressure p_∞ with the value of p_{g0} being influenced by air content in the liquid. A theoretical model by Brennen [45] describes a relation between initial gas pressure p_{g0} in the bubble and air content α^* [ppm] as:

$$P_{g0} \sim 69 \cdot \alpha^*. \tag{28}$$

After evaluating the ratio of p_{g0}/p_∞, the value of efficiency η^* can be determined according to the graph presented in Figure 61. It is obvious, that with increasing air content α^* (thus, increasing p_{g0}), the efficiency of the collapse grows, hence meaning greater intensity of cavitation collapse.

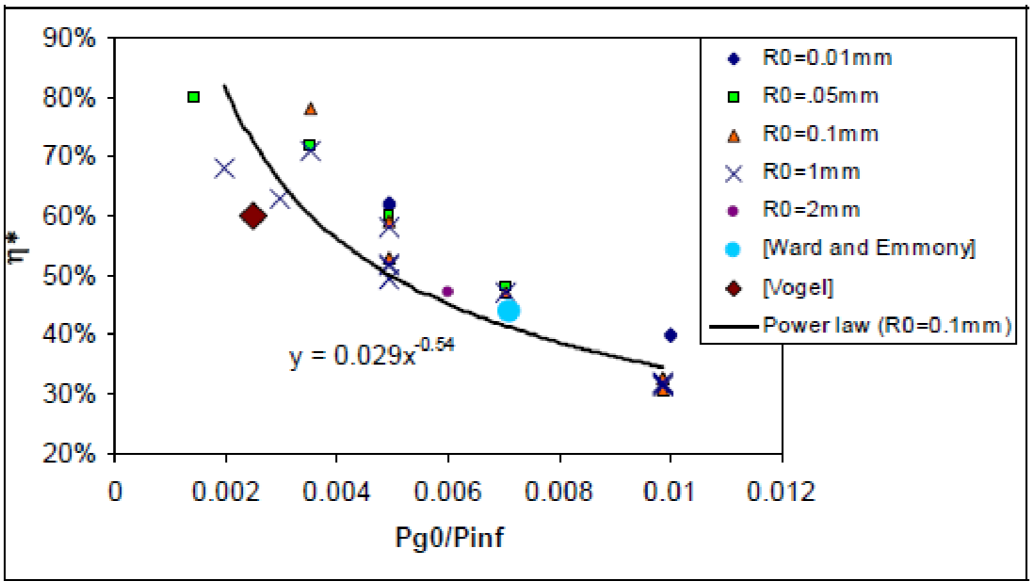

Figure 61: Collapse efficiency [41]

The authors [41] examined the influence of p_{g0} – the applied values were 500 Pa, 1000 Pa and 5000 Pa. In this thesis, p_{g0} = 1000 Pa as the middle value, is going to be taken into consideration. Consequently, together with p_∞ = 101 325 Pa (supposing a vast reservoir), the efficiency η^* can be determined as 0.35.

Afterwards, the quantity P_{waves}^{mat} can be expressed as:

$$\frac{P_{waves}^{mat}}{\Delta S} = \eta^* \cdot \frac{P_{pot}^{mat}}{\Delta S} \tag{29}$$

To correlate the potential energy of the pressure waves emitted during the cavitation collapse to material damage of the sample, the authors [41] assumed this relation:

$$\frac{P_{waves}^{mat}}{\Delta S} = \beta^* \cdot V_d, \tag{30}$$

where β^* is a material characteristics determined from various numerical simulations. For copper, the value was found out to be $\beta^*_{copper} \approx 20 \pm 2$ J/mm^3 [41]. Quantity V_d represents the volume damage rate, thus a ratio of deformed volume of the sample (relative to the surface of the sample and the duration of the experiment [41]. In Chapter 2.3.2, the volume damage rate was found out to be $2.014 \cdot 10^{-11}$ m^3/(m^2·s) for the copper sample.

3.5.2 Preprocessing of the numerical simulation for cavitation erosion prediction

As mentioned above, the setting of computation no. 7 led to quite realistic display of the cavitating jet, therefore, the simulation was rerun for the second time. Nonetheless, this time various quantities including static pressure, vapor fraction, mass transfer rate and density were monitored, hence the potential power of cavitation could be evaluated using a script in Python. The monitoring of the mentioned quantities was performed at 11 lines from $h_0 = 0$ mm to h_{agr}, which was determined as 0.0002 m. The distance between 2 adjacent lines was in all cases the same (0.00002 m), corresponding to the grid distribution. The length of the lines was set to 0.03 m as it was the maximal distance from the axis, at which the cavitation cloud still appeared in computation no. 6. Each line incorporated 396 nodes, resulting in the total number of 4356 monitored nodes. Data was exported as an ASCII file each 300th time-step, which was set to a fixed value of $1.59 \cdot 10^{-7}$ s (the time-step size was determined from computation no. 6). Moreover, the volume vapor fraction was monitored also in other 4 points of the domain in order to determine the shedding frequency of the cavitating liquid jet. The monitoring area is presented in Figure 62.

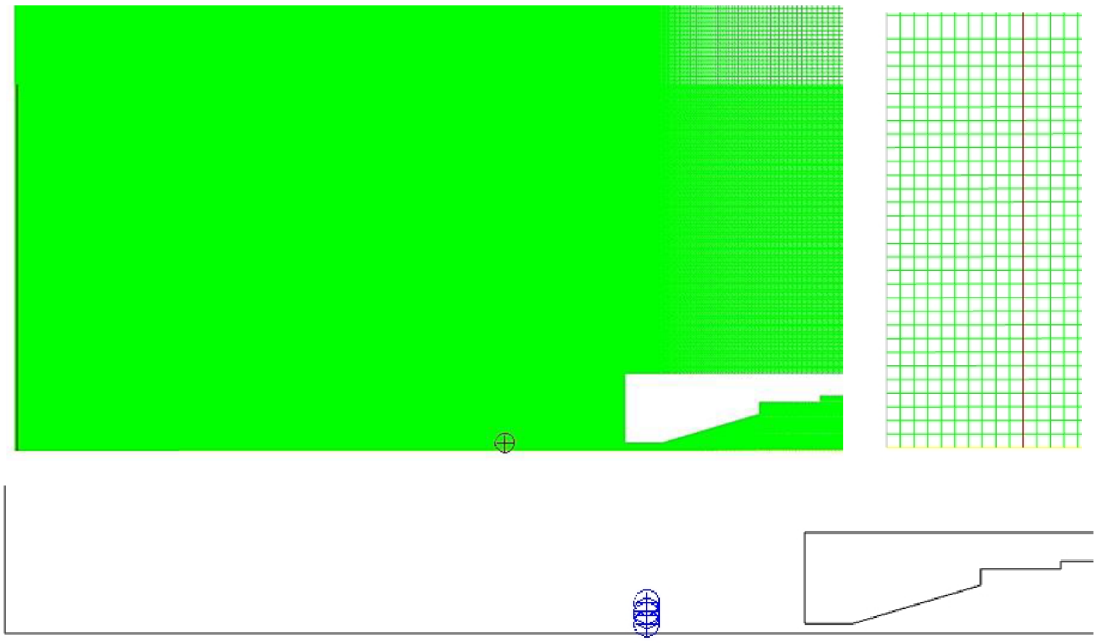

Figure 62: Monitoring area (dark red line – h_{agr}) and one of the 4 monitoring points (left), detail of the grid with h_{agr} (right), locations of all the monitoring points (bottom)

3.5.3 Post-processing of the numerical simulation for cavitation erosion prediction

This chapter is devoted to the post-processing of the numerical simulation – shedding frequency of the cavitation cloud and time-dependence of the bubble radius were analyzed.

3.5.3.1 Shedding frequency

Shedding frequency of the cavitating liquid jet was determined by performing Fast Fourier Transformation on the vapor fraction data obtained from the 4 monitoring points. In all cases, the resulting shedding frequency was evaluated as 5256 Hz, see Figure 63.

Consequently, the shedding period can be easily obtained as 0.00019 s. Nonetheless, the shedding frequency acquired from the simulation is approximately 5 times larger than the shedding frequency determined from the visualization with high-speed camera (1028 Hz). Therefore, it is obvious, that the simulation does not provide completely realistic results, but, at least, the order accuracy was achieved. One possible reason for lower shedding frequency in experiment might be higher damping effect in comparison with CFD due to dissolved air present in water.

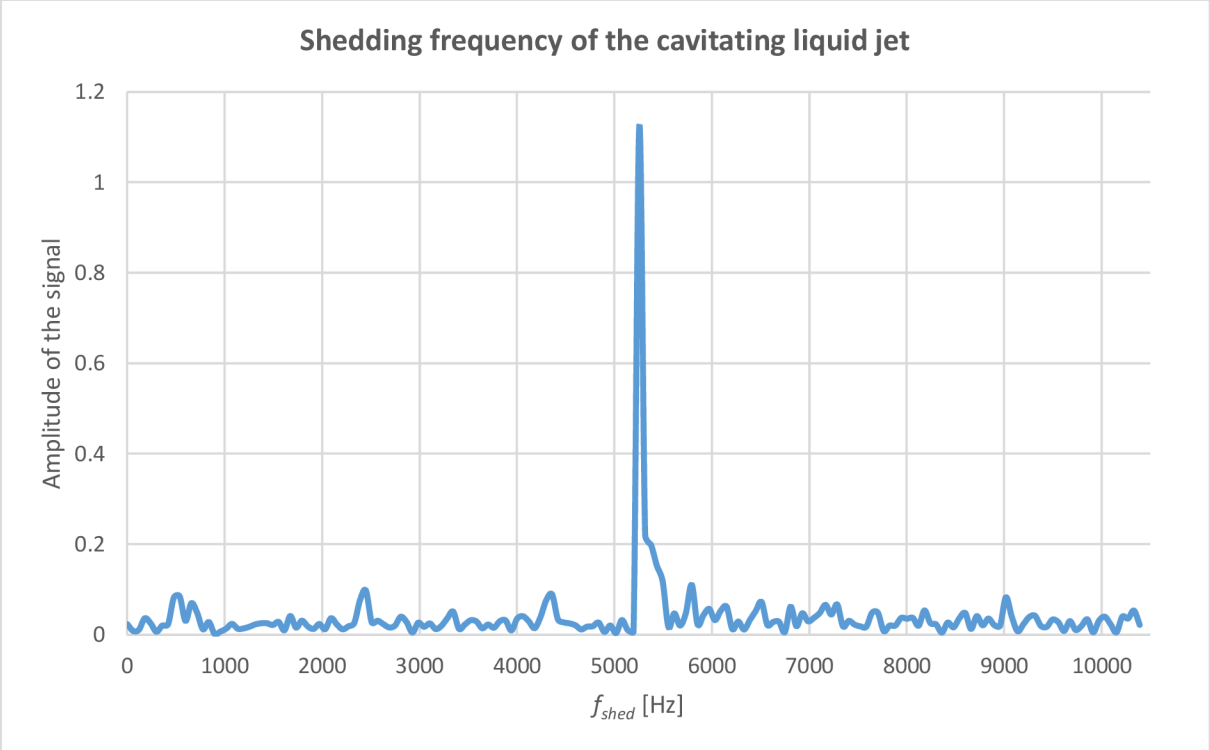

Figure 63: Shedding frequency of the cavitating liquid jet

3.5.3.2 Time-dependence of the bubble radius

Subsequently, as a part of the post-processing, the time-dependence of a bubble radius was studied. The Schnerr-Sauer model assumes the vapor volume fraction defined as [47]:

$$\alpha_V = \frac{V_V}{V_{cell}} = \frac{n_B \cdot \frac{4}{3} \cdot \pi \cdot R_B^3}{V_V + V_L} = \frac{n_0 \cdot V_L \cdot \frac{4}{3} \cdot \pi \cdot R_B^3}{n_0 \cdot V_L \cdot \frac{4}{3} \cdot \pi \cdot R_B^3 + V_L} = \frac{n_0 \cdot \frac{4}{3} \cdot \pi \cdot R_B^3}{1 + n_0 \cdot \frac{4}{3} \cdot \pi \cdot R_B^3}, \tag{31}$$

where V_{cell} is the computational cell volume, V_L is the volume occupied by liquid, V_V is the volume occupied by vapor, n_B is the number of bubbles in the computational cell, R_B is the bubble radius and n_0 is the concentration of cavitation bubbles per unit volume of pure liquid V_L. Consequently, the bubble radius R_B can be expressed from Eq. 31 as [47]:

$$R_B = \left(\frac{\alpha_V}{1 - \alpha_V} \cdot \frac{1}{n_0} \cdot \frac{3}{4\pi} \right)^{\frac{1}{3}}. \tag{32}$$

The quantity n_0 is a constant of the Schnerr-Sauer cavitation model equaled to 1e+11 m^{-3}.

Figure 64 presents a time-dependence of the bubble radius throughout two following shedding cycles at the location of the point presented in Figure 62. Similar curves were obtained also in case of points located at h_{agr}.

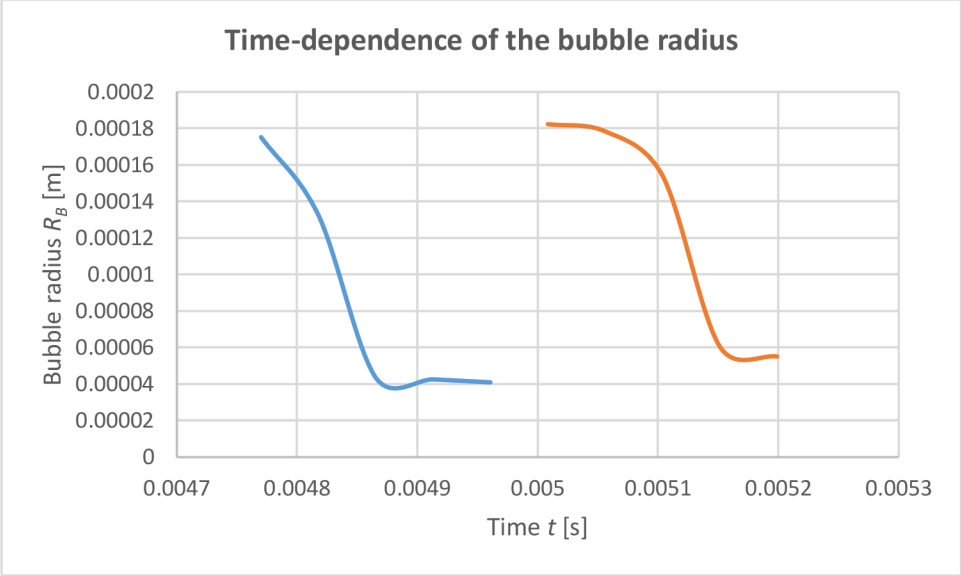

Figure 64: Bubble radius throughout two shedding cycles

It can be seen from Figure 64 that the initial bubble radius was around 0.00018 m (180 μm) and consequently it was reduced to a value of 0.00004 m (40 μm). It is highly probable that the bubble radius rebounded a few times as in the theoretical example presented in Figure 4, however, as the data was not stored with such a frequency, it is not possible to illustrate it here.

3.5.4 Prediction of cavitation erosion based on the numerical results

This chapter is devoted to the cavitation erosion prediction using the modified energy cascade model with numerical results acquired from computation no. 7 and experimental results, therefore, the main aim is to assess Eq. 30, where its left-hand side is going to be evaluated using the CFD results, and the right-hand side is obtained from the experiment.

As mentioned above, the volume damage rate was determined as $V_d = 2.014 \cdot 10^{-11}$ m^3/(m^2·s) based on the experimental results. Together with the material characteristics $\beta^*_{copper} \approx 20 \pm 2$ J/mm^3, the right-hand side of Eq. 30 can be evaluated to 0.403 W/m^2.

The evaluation of the left-hand side is based on the CFD results and the assumption of h_{agr} equaled to 10% of the thickness of the emerging cavitating structure according to Kato et al. [42], which in this case was determined as 0.0002 m.

The potential power density was evaluated according to Eq. 25, where the driving pressure p_d was set to be the atmospheric pressure as the water tank is quite large and the pressure distribution can be therefore regarded as homogenous. This presumption was confirmed by the contours of static pressure, see Figure 65.

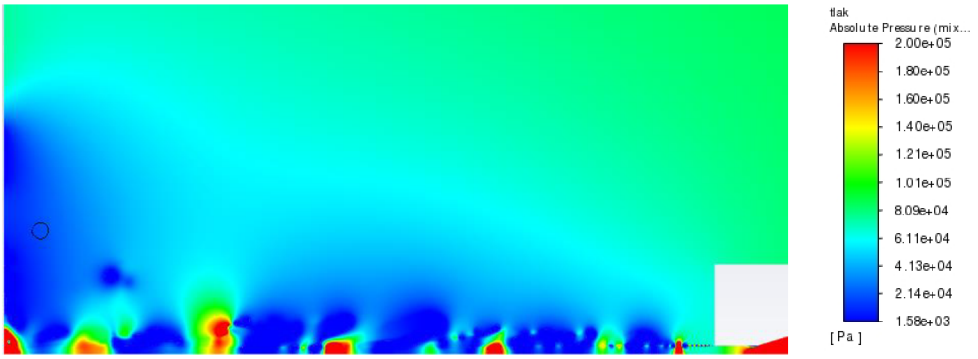

Figure 65: Contours of static pressure

To perform the integration described in Eq. 27, a trapezoidal rule[4] for approximating of the definite integral was utilized with *dh* equaled to the distance between two data lines (0.00002 m). Furthermore, another integration using trapezoidal rule was performed when integrating over time to get the total energy (per m^2) supplied to the bottom wall.

Finally, the intensity of the collapsing cavitation structure was determined – Figure 66 displays the cumulative cavitation aggressiveness after approximately 116 shedding cycles dependent on the y-coordinate, thus the distance from the axis.

[4] Trapezoidal rule is a method for approximating of a definite integral by substituting the area under the curve *f(x)* by multiple trapezoids, which can be mathematically expressed as [46]: $\int_a^b f(x)\,dx \approx (b-a)\cdot\frac{1}{2}\cdot\left(f(a)+f(b)\right)$.

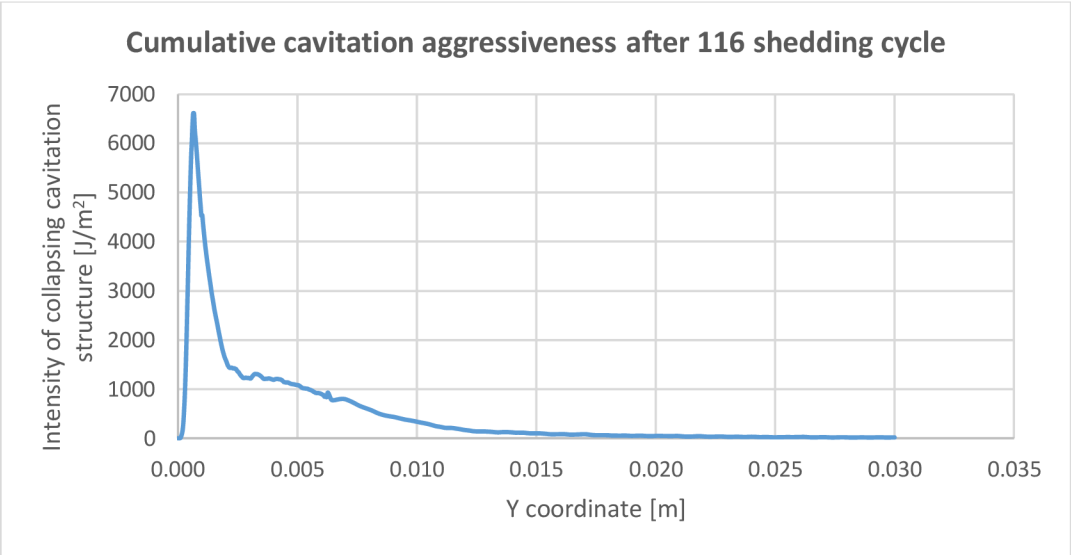

Figure 66: Cumulative cavitation aggressiveness after approximately 116 shedding cycles

From Figure 66, it can be seen, that after approximately 116 shedding cycles, the maximum intensity of imploding cavitation reached a value of 6611 J/m^2 at a distance of 0.0006 m, which corresponds to the radius of the inner deep pit located directly underneath the nozzle. The ring pitted region, which is typical of cavitation peening, has an inner radius of approximately 7.5 mm. In Figure 66, the corresponding value of cavitation intensity at this location was approximately 690 J/m^2 after 116 shedding cycles.

Afterwards, another integration was carried out to determine the total power supplied to the whole sample. As the geometry is of axisymmetric nature, the integration was performed in polar coordinates, therefore it was necessary to compute the Jacobian.

Consequently, the total energy was divided by the number of shedding cycles, for which the computation ran (116 shedding cycles), multiplied by the shedding period obtained from Chapter 3.5.3.1 as 0.00019 s. This was performed to obtain the average power supplied to the bottom wall from cavitation, that means the value of P_{pot}^{mat}. As mentioned in Chapter 3.5.1, the total power P_{waves}^{mat} finally reaching the material can be calculated as a multiplication of P_{pot}^{mat} and the efficiency of pressure waves transmitting the energy of imploding cavitation to the sample denoted as η^*, which was calculated to be 0.35 (for p_{g0} = 1000 Pa).

Eventually, the total power P_{waves}^{mat} was determined according to the procedure described above to be 6.50 W/m^2.

However, the results from experiment brought the value of 0.403 W/m^2, thus more than 15 times lower than CFD results. This suggests that the energy cascade model with chosen h_{agr} equaled to 10% of the cavitation sheet thickness does not provide an accurate prediction of the cavitation erosion. It is important to note, that the proposed value of h_{agr} was probably meant for applications of lower cavitation intensity than in this case. Therefore, an idea arose to further reduce the value of h_{agr} and simultaneously, expect the p_{g0} to be of higher values as the shedding frequency determined from experiment reached lower values than the computational one, implying that the damping effect in experiment was more significant. To be more coherent with

the experiment, the p_{g0} should be increased to reduce the efficiency of the energy transmission from the collapsing cavitation cloud to the sample.

The next re-calculation of the CFD results was performed with h_{agr} equaled to 5% of cavitation sheet thickness, therefore h_{agr} = 0.0001 m, and with p_{g0} equaled to 5000 Pa. Those adjustments to the energy cascade model led to the total power P_{waves}^{mat} equaled to 0.96 W/m^2. This result corresponds much better to the experimental result of 0.403 W/m^2. Table 10 summarizes the obtained results.

Table 10: Summary of the results

Method	Total power supplied to the sample [W/m^2]
Experiment	0.403
CFD: h_{agr}=10% of cavitation sheet thickness, p_{g0} = 1000 Pa	6.5
CFD: h_{agr}=5% of cavitation sheet thickness, p_{g0} = 5000 Pa	0.96

Further improvements to the energy cascade model are not going to be considered. The reason for this decision is that the whole procedure is unfortunately very approximate and burdened with lots of possible errors. Concerning the experiment, a more accurate method for determining the eroded volume should be considered and an exact air content in water should be specified by laboratory methods. Regarding the numerical simulation, a great improvement of the computation accuracy could be obtained by applying more advanced turbulence model (e.g. k-ω SST together with UDF for reduction of the turbulent viscosity) and by the implementation of the energy equation.

More research needs to be done to make it possible to predict the cavitation erosion only by means of computational fluid dynamics. Nonetheless, the potential of the energy cascade model for cavitation erosion prediction is unquestionable.

Conclusion and discussion

The diploma thesis starts with a thorough description of the basic principles of cavitation, including its inception and collapse mechanisms. Attention was also focused on various models of cavitation erosion, which serve to link experimental and numerical results. An extensive chapter was devoted directly to the cavitating jet and describes in detail its dynamic behavior, including the effect of a stand-off distance, injection pressure, cavitation number, nozzle geometry, speed of sound and water properties.

In the experimental part, a copper sample was tested on a new experimental stand (inspired by ASTM G134 standard) at OFIVK FME BUT Brno. The new stand allows more convenient sample handling, and also provides more accurate measurements. The main outcomes of the experimental part include graphs of cumulative mass loss and rate of mass loss, and in addition, a shedding frequency of the cavitating jet obtained from the visualization performed by a high-speed camera. The total mass loss after 15 hours of testing was determined to be 1.16461 g using a high-precision scale. Moreover, it was possible to distinctively recognize the incubation phase, the acceleration of erosion, its subsequent slowing down and then achieving a constant rate of mass loss. Among other things, the experiment confirmed the value of the optimal stand-off distance to be 50 mm, guaranteeing that the predominant mechanism of erosion is cavitation and not water jet cutting, as a ring pitted region appeared on the sample surface, characteristic for cavitation peening. In addition, the measured flow rate, pressure and temperature also served as an input for defining boundary conditions in numerical simulations. The shedding frequency of the cavitation cloud determined by means of images taken by a high-speed camera was determined to be 1028 Hz, i.e. the shedding period was evaluated as $9.73 \cdot 10^{-4}$ s. Moreover, a set of very interesting and rather unique pictures of eroded surface, obtained in a cooperation with CEITEC, was presented. Surface topography, profilometry and observation of the eroded surface and the individual particles by SEM enabled us to investigate the cavitation erosion mechanisms in detail. In addition, the Brinell hardness of the sample, connected to cavitation resistance, was determined to be 86.74 HBW.

Another set of experiments was carried out to observe the pit distribution over the sample and to approximate the volume damage rate during the incubation period. The resulting total power impacting the sample surface was detemined as 0.403 W/m^2 and was later linked to results from computational modelling via energy cascade model.

In the last chapter, a description of performed numerical simulations of cavitating jet was provided. An extensive part of this chapter was also devoted to a thorough description of the chosen cavitation and turbulent models and the overall settings of the individual calculations including the problems connected to modelling of such dynamic phenomenon like cavitating liquid jet. The final calculation was performed with RNG k-ε turbulence model enhanced by UDF for turbulent viscosity reduction. Post-processing of results included evaluation of the shedding frequency by performing Fast-Fourier Transformation on vapor fraction data with the result of 5256 Hz. Unfortunately, this value is approximately 5 times higher than the value of shedding frequency determined from the experiment. One possible explanation is a higher damping effect during experiment, which might be connected to the increased amount of air content in water.

Another important subchapter of the computational part focuses on the determination of the total power supplied to the sample by evaluating the modified energy cascade model. At first, the effective distance at which cavitation is assumed to still cause severe damage to the sample, h_{agr}, was considered to be 10% of the cavitation sheet thickness as proposed by other researchers who employ the energy cascade model; and the initial gas pressure p_{g0} was supposed to be 1000 Pa. However, the resulting total power was approximately 15 times larger than that one determined from the experiment.

Therefore, some improvements to the modified energy cascade model were implied – firstly, the reduction of the h_{agr} to 5% of the cavitation sheet thickness reasoned by very high cavitation aggressiveness of the cavitating liquid jet, and secondly, p_{g0} was increased to value of 5000 Pa, based on obtaining lower shedding frequency from the experiment, which might have been caused by a higher amount of air content. These adjustmensts led to the total power supplied to the sample being equaled to 0.96 W/m^2, which corresponds quite well to the experimental result of 0.403 W/m^2, mentioned above.

However, it is very important to note, that the whole process of the evaluation of the modified energy cascade model is burdened by errors on both sides, the experimental and the computational one. In case of the experiment, a more precise evaluation of pits' volume and the determination of air content is necessary to obtain more precise results. Concerning the computation, the SST k-ω might bring more accurate data, nonetheless, running the simulation with this turbulence model on the fine mesh and with the reuired low time-step would be very challenging.

To conclude, the energy cascade model is undoubtedly a very powerful tool for cavitation erosion prediction in the phase of CFD modelling. However, some types of problems are more suitable for this approach, especially cases with cavitation number lying in interval of tenths to units, which is, unfortunately, not the case of cavitating liquid jet. Yet, this thesis definitely yielded many valuable results and insights into the computational and experimental study of the cavitating liquid jet, thus advancing scientific research in this field.

References

[1] NOSKIEVIČ, Jaromír. *Kavitace v hydraulických strojích a zařízeních*. Praha: SNTL, 1989. ISBN 80-03-00206-0.

[2] KIM, Ki-Han, Georges CHAHINE, Jean-Pierre FRANC a Ayat KARIMI. *Advanced experimental and numerical techniques for cavitation erosion prediction*. Dordrecht: Springer, [2014]. Fluid mechanics and its applications, v. 106.

[3] JYOTI, K.K a A.B PANDIT. Water disinfection by acoustic and hydrodynamic cavitation. *Biochemical Engineering Journal*. 2001, 7(3), 201-212. DOI: 10.1016/S1369-703X(00)00128-5. ISSN 1369703X. Also available at: http://linkinghub.elsevier.com/retrieve/pii/S1369703X00001285

[4] SUSLICK, Kenneth S., Millan M. MDLELENI a Jeffrey T. RIES. Chemistry Induced by Hydrodynamic Cavitation. *Journal of the American Chemical Society*. 1997, 119(39), 9303-9304. DOI: 10.1021/ja972171i. ISSN 0002-7863. Also available at: http://pubs.acs.org/doi/abs/10.1021/ja972171i

[5] BRENNEN, Christopher E. *Cavitation and bubble dynamics*. New York: Cambridge University Press, 2014. ISBN 978-1-107-64476-2.

[6] KOZÁK, Jiří. Kavitace vyvolaná rotací kapaliny. Brno, 2020. Also available at: https://www.vutbr.cz/studenti/zav-prace/detail/122496. Dizertační práce. Vysoké učení technické v Brně, Fakulta strojního inženýrství, Energetický ústav. Vedoucí práce Pavel Rudolf.

[7] HUANG, Jianhua. A Simple Accurate Formula for Calculating Saturation Vapor Pressure of Water and Ice. *Journal of Applied Meteorology and Climatology*. 2018, 57(6), 1265-1272. ISSN 1558-8424. Available at: doi:10.1175/JAMC-D-17-0334.1

[8] BRDIČKA, Miroslav, Ladislav SAMEK a Oldřich TARABA. *Kavitace: Diagnostika a technické využití*. Praha: SNTL, 1981.

[9] SUN, Jing, Zhuangzhi SHEN a Runyang MO. Theoretical prediction of the yield of strong oxides under acoustic cavitation. *Chinese Physics B*. 2019, **28**(1). ISSN 1674-1056. Available at: doi:10.1088/1674-1056/28/1/014301

[10] Introduction to Cavitation. In: *The Process Piping* [online]. 2017 [cit. 2019-03-31]. Available at: https://www.theprocesspiping.com/introduction-to-cavitation/

[11] NIEVES-SOTO, Mario, Oscar M., Carlos ALBERTO, Marco ANTONIO, Toms VIVEROS-GARCA a Ignacio CONTRERAS-ANDRADE. Biodiesel Current Technology: Ultrasonic Process a Realistic Industrial Application. *Biodiesel - Feedstocks, Production and Applications*. InTech, 2012, 2012-12-03. DOI: 10.5772/52384. ISBN 978-953-51-0910-5. Also available at: http://www.intechopen.com/books/biodiesel-feedstocks-production-and-applications/biodiesel-current-technology-utrasonic-process-a-realistic-industrial-application

[12] FRANC, Jean-Pierre a Jean-Marie MICHEL. *Fundamentals of cavitation*. Boston: Kluwer Academic Publishers, c2004. ISBN 14-020-2232-8.

[13] SOYAMA, Hitoshi. Cavitating Jet: A Review. *Applied Sciences*. 2020, 10(20). ISSN 2076-3417. Available at: doi:10.3390/app10207280

[14] NOSKIEVIČ, Jaromír. *Kavitace*. Praha: Academia, 1969, 278 s. : il.

[15] SOYAMA, Hitoshi. Key Factors and Applications of Cavitation Peening. *Inter. J. Peen. Sci. Technol*. 2017, (1), 59.

[16] VAN TERWISGA, Tom J.C., Patrick A. FITZSIMMONS, Li ZIRU a Evert Jan FOETH. *Cavitation Erosion – A review of physical mechanisms and erosion risk models*. Michigan, USA: International Symposium on cavitation, 2009, 7(41), 21.

[17] GENG, Linlin, Jian CHEN, Oscar DE LA TORRE a Xavier ESCALER. Numerical Simulation of Cavitation Erosion Aggressiveness Induced by Unsteady Cloud Cavitation. *Applied Sciences*. 2020, 10(15). ISSN 2076-3417. Available at: doi:10.3390/app10155184

[18] KATO, Hiroharu, Akihisa KONNO, Masatsugu MAEDA a Hajime YAMAGUCHI. Possibility of Quantitative Prediction of Cavitation Erosion Without Model Test. *Journal of Fluids Engineering*. 1996, 118(3), 582-588. ISSN 0098-2202. Available at: doi:10.1115/1.2817798

[19] BARK, G., N. BERCHICHE a M. GREKULA. Application of principles for observation and analysis of eroding cavitation, EROCAV observation handbook. *The EROCAV observation handbook*. Department of Shipping and Marine Technology, Chalmers University of Technology, Sweden, Edition 3.1.

[20] FORTES-PATELLA, R., J.L. REBOUD a L. BRIANCON-MARJOLLET. A Phenomenological and numerical model for scaling the flow agressiveness in cavitation erosion. *EROCAV workshop*. Val de Reuil, France, 2004.

[21] PATELLA, R. Fortes, A. ARCHER a C. FLAGEUL. Numerical and experimental investigations on cavitation erosion. *IOP Conference Series: Earth and Environmental Science*. 2012, 15(2). ISSN 1755-1307. Available at: doi:10.1088/1755-1315/15/2/022013

[22] DULAR, M., B. SIROK a B. STOFFEL. Experimental and numerical modelling of cavitation erosion. *Sixth International Symposium on Cavitation*. Wageningen, 2006, CAV2006.

[23] SOYAMA, H. a A. LICHTAROWICZ. Cavitating jets—Similarity correlations. *J. Jet Flow Eng*. 1996, (13), 9-19.

[24] NISHIMURA, Satoshi, Osamu TAKAKUWA a Hitoshi SOYAMA. Similarity Law on Shedding Frequency of Cavitation Cloud Induced by a Cavitating Jet. *Journal of Fluid Science and Technology*. 2012, 7(3), 405-420. ISSN 1880-5558. Available at: doi:10.1299/jfst.7.405

[25] SOYAMA, Hitoshi. Surface mechanics design of metallic materials on mechanical surface treatments. *Mechanical Engineering Reviews*. 2015, 2(1), 14-00192-14-00192. ISSN 2187-9753. Available at: doi:10.1299/mer.14-00192

[26] SUTOWSKI, Paweł, Jarosław PLICHTA a Paweł KAŁDUŃSKI. Determining kinetic energy distribution of the working medium in a centrifugal disc finishing process—part 2: experimental analysis with the use of acoustic emission signal. *The International*

Journal of Advanced Manufacturing Technology. 2019, 104(1-4), 687-704. ISSN 0268-3768. Available at: doi:10.1007/s00170-019-03937-2

[27] SOYAMA, H. a H. KAMISAKA. Effect of injection pressure on mechanical surface treatment using a submerged water jet. *J. Jet Flow Eng*. 2018, (33), 4-10.

[28] SOYAMA, Hitoshi. Fundamentals and Applications of Cavitation Peening Comparing with Shot Peening and Laser Peening. *Advanced Surface Enhancement*. Singapore: Springer Singapore, 2020, 2020-08-31, , 76-87. Lecture Notes in Mechanical Engineering. ISBN 978-981-15-0053-4. Available at: doi:10.1007/978-981-15-0054-1_9

[29] SPXFLOW APV Cavitator. *AndersonDahlen* [online]. [cit. 2021-7-14]. Available at: https://andersondahlen.com/stock-products/miscellaneous-products/spxflow-apv-cavitator

[30] KAMISAKA, Hirokazu a Hitoshi SOYAMA. Enhancement of an aggressive intensity of a cavitating jet by water flow holes near nozzle outlet. *Transactions of the JSME (in Japanese)*. 2019, 85(879), 19-00280-19-00280. ISSN 2187-9761. Available at: doi:10.1299/transjsme.19-00280

[31] SPIELMANN, Šimon. Modifikace experimentálního stendu pro testování kavitační eroze [online]. Brno, 2021 [cit. 2021-05-21]. Available at: https://www.vutbr.cz/studenti/zav-prace/detail/132703. Bakalářská práce. Vysoké učení technické v Brně, Fakulta strojního inženýrství, Energetický ústav. Vedoucí práce Pavel Rudolf.

[32] VYSOKOTLAKÁ ČERPADLA EVOLUTION 2. *HABRA* [online]. [cit. 2021-7-16]. Available at: https://interpump.cz/cs/interpump/evolution-2/e2b2014/

[33] DMP 331: stainless steel sensor. *BD SENSORS* [online]. [cit. 2019-05-20]. Available at: http://www.bdsensors.cz/fileadmin/user_upload/Download/Datenblaetter_datasheets/DMP331_CS.pdf

[34] Magneticko indukční průtokoměry. *ELA - měřidla pro vodárenství* [online]. [cit. 2019-05-20]. Available at: http://www.elabrno.cz/cs/magneticko-indukcni-prutokomery-mqi-si/

[35] ANSYS FLUENT 12.0 User's Guide. *EneaGrid* [online]. [cit. 2021-7-18]. Available at: https://www.afs.enea.it/project/neptunius/docs/fluent/html/ug/main_pre.htm

[36] Nozzletabel. *Vermeulen B. V.* [online]. [cit. 2021-8-8]. Available at: https://www.vermeulenzevenaar.nl/images/uploaded/nozzletabel.pdf

[37] KOTOULOVÁ, Helena. Cavitation erosion mechanisms. Brno, 2019 [cit. 2019-05-22]. Available also at: https://www.vutbr.cz/studenti/zav-prace/detail/117998. Bachelor's thesis. Brno University of Technology, Faculty of Mechanical Engineering, Energy Institute. Supervisor Pavel Rudolf.

[38] COUTIER-DELGOSHA, O., R. FORTES-PATELLA a J. L. REBOUD. Evaluation of the Turbulence Model Influence on the Numerical Simulations of Unsteady Cavitation. *Journal of Fluids Engineering*. 2003, **125**(1), 38-45. ISSN 0098-2202. Available at: doi:10.1115/1.1524584

[39] ZHAO, Minsheng, Decheng WAN a Yangyang GAO. Comparative Study of Different Turbulence Models for Cavitational Flows around NACA0012 Hydrofoil. *Journal of*

Marine Science and Engineering. 2021, **9**(7). ISSN 2077-1312. Available at: doi:10.3390/jmse9070742

[40] TURBULENCE PART 2 - WALL FUNCTIONS AND *Y+* REQUIREMENTS. *COMPUTATIONAL FLUID DYNAMICS BLOG - LEAP AUSTRALIA* [online]. Australia [cit. 2021-10-22]. Available at: https://www.computationalfluiddynamics.com.au/tips-tricks-turbulence-wall-functions-and-y-requirements/

[41] FLAGEUL, Cédric, Regiane FORTES PATELLA a Antoine ARCHER. Cavitation Erosion Prediction by Numerical Cavitation. *Proc. of 14th International Symposium on Transport Phenomena and Dynamics of Rotating Machinery: ISROMAC14*. Honolulu, United States, 2012; hal-02510566f.

[42] KATO, Hiroharu, Akihisa KONNO, Masatsugu MAEDA a Hajime YAMAGUCHI. Possibility of Quantitative Prediction of Cavitation Erosion Without Model Test. *Journal of Fluids Engineering*. 1996, **118**(3), 582-588. ISSN 0098-2202. Available at: doi:10.1115/1.2817798

[43] FUJIKAWA, Shigeo a Teruaki AKAMATSU. Effects of the non-equilibrium condensation of vapour on the pressure wave produced by the collapse of a bubble in a liquid. Journal of Fluid Mechanics. 1980, 97(03). ISSN 0022-1120. Available at: doi:10.1017/S0022112080002662

[44] PROSPERETTI, A. a A. LEZZI. Bubble dynamics in a compressible liquid. Part 1. First-order theory. Journal of Fluid Mechanics. 1986, 168(-1). ISSN 0022-1120. Available at: doi:10.1017/S0022112086000460

[45] BRENNEN, C. The dynamic balances of dissolved air and heat in natural cavity flows. *Journal of Fluid Mechanics*. 1969, **37**(1), 115-127. ISSN 0022-1120. Available at: doi:10.1017/S0022112069000449

[46] Trapezoidal Rule. ScienceDirect [online]. [cit. 2021-12-06]. Available at: https://www.sciencedirect.com/topics/mathematics/trapezoidal-rule

[47] VILLAFRANCO, Dorien O., Huy K. DO, Sheryl M. GRACE, Emily M. RYAN a R. Glynn HOLT. Assessment of Cavitation Models in the Prediction of Cavitation in Nozzle Flow. Volume 2: Development and Applications in Computational Fluid Dynamics; Industrial and Environmental Applications of Fluid Mechanics; Fluid Measurement and Instrumentation; Cavitation and Phase Change. American Society of Mechanical Engineers, 2018, 2018-07-15, , -. ISBN 978-0-7918-5156-2. Available at: doi:10.1115/FEDSM2018-83223

Symbols and abbreviations

Roman letters

Symbol	Unit	Explanation
C_μ	-	Model constant for the turbulent viscosity
d	m	Nozzle diameter
dm/dt	g/h	Mass loss rate
E_{pot}	J	Potential energy
f_{shed}	Hz	Shedding frequency
I_{cav}	J	Cavitation intensity
h_{agr}	m	Effective distance
K	$kg \cdot m^{-n} \cdot s^{n-1}$	A proportionality coefficient in Eq. (4)
k	$m^2 \cdot s^{-2}$	Rate of dissipation of turbulent kinetic energy
L_{cav}	m	Cavitation length
m	g	Mass
$\Delta m_{cummulative}$	g	Cumulative mass loss
$\Delta m_{partial}$	g	Partial mass loss between two following measurements
$\dot{m}$	$kg \cdot s^{-1}$	Mass flow rate
$\dot{m}_l$	$kg \cdot s^{-1}$	Mass loss
n	-	Exponent in Eq. (4)
n_B	-	Number of bubbles in the computational cell
n_0	m^{-3}	Bubble concentration per unit volume of pure liquid
p_B	Pa	Homogenous (uniform) pressure in the bubble
p_{g0}	Pa	Initial gas pressure
p_v	Pa	Saturated vapor pressure
p_d	Pa	Driving pressure of cavitation collapse
p_{max}	Pa	Maximum pressure at the jet centre (cavitating jet experiment)
p_∞	Pa	Pressure at an infinite distance from the bubble (reference pressure)
$p(r,t)$	Pa	Pressure field
p_1	Pa	Pressure upstream the nozzle (cavitating jet experiment)
p_2	Pa	Pressure in the tank in cavitating jet experiment
P_{agr}	W/m^2	Aggressive potential power
P_{den}	W/m^3	Potential power density
P_{pot}	W	Instantaneous potential power
P_{pot}^{mat}	W	Power of cavitation aggressiveness
P_{waves}^{mat}	W	Potential energy of pressure waves reaching the material
r	m	Radial coordinate
R, R_B	m	Bubble radius
R_0	m	Initial bubble radius
$\dot{R}$	$m \cdot s^{-1}$	Velocity of a bubble wall motion
$\ddot{R}$	$m \cdot s^{-2}$	Acceleration of a bubble wall motion
$\vec{R}$	m	Position vector
s_{opt}	m	Optimal standoff distance
$u(r,t)$	$m \cdot s^{-1}$	Outward velocity
u	$m \cdot s^{-1}$	Flow velocity
v	$m \cdot s^{-1}$	Flow velocity

v_0	$m \cdot s^{-1}$	Ultimate flow velocity at which cavitation still occurs
$v_i(x_i)$	$m \cdot s^{-1}$	Velocity field
v_{max}	$m \cdot s^{-1}$	Maximal velocity in the cavitating jet experiment
v_s	$m \cdot s^{-1}$	Speed of sound
$v_{s,th}$	$m \cdot s^{-1}$	Threshold value of speed of sound
v_∞	$m \cdot s^{-1}$	Reference velocity
V_B	m^3	Bubble volume
V_{cell}	m^3	Volume of one cell in a numerical model
V_d	$m^3/(m^2 \cdot s)$	Volume damage rate
V_L	m^3	Volume occupied by liquid
V_V, V_{vap}	m^3	Volume of the vapor structure
t	s	Time
T	K	Temperature

Greek letters

Symbol	Unit	Explanation
α_v	-	Volume fraction
α^*	ppm	Air content
β	m^{-1}	Processing capability
β^*	J/mm^3	Material characteristics
Δp	Pa	Pressure difference
ΔS	m^2	Area
Δt	s	Time period
ε	$m^2 \cdot s^{-3}$	Turbulent kinetic energy
η^*	-	Efficiency of potential power energy transfer
η^{**}	-	Efficiency of potential power material energy transfer
μ_t	$Pa \cdot s$	Turbulent viscosity
ν_L	$m^2 \cdot s^{-1}$	Kinematic viscosity of a liquid
ν_t	$m^2 \cdot s^{-1}$	Kinematic turbulent viscosity
ρ	$kg \cdot m^{-3}$	Fluid (respectively, mixture) density
ρ_l	$kg \cdot m^{-3}$	Liquid density
ρ_v	$kg \cdot m^{-3}$	Vapor density
σ	-	Cavitation number
σ_L	-	Local cavitation number
σ^*_L	$N \cdot m^{-1}$	Surface tension at an liquid/bubble interface
ω	s^{-1}	Specific rate of turbulence kinetic energy dissipation

Abbreviations

CFD	Computational Fluid Dynamics
SEM	Scanning Electron Microscope
SST	Shear Stress Transport
RNG	Renormalization Group
UDF	User Defined Function